12-3-2015

Electronic Structure Calculations of Monolayer–Protected Gold NanoClusters to Aid Spectroscopic Analysis

Neranjan V. Perera
University of Connecticut, neranjan007@gmail.com

Electronic Structure Calculations of Monolayer–Protected Gold NanoClusters to Aid Spectroscopic Analysis

Neranjan Vikum Perera, Ph.D

University of Connecticut, 2015

The underlying goal of this thesis dissertation is to simulate small monolayer protected clusters (MPCs) via quantum mechanics and molecular mechanics calculations to derive electronic, structural, and dynamical properties. First we specifically focus on monolayers consisting of thiolated oligopeptides and alkanethiols. We construct MPCs with a layer of oligopeptides consisting of α-aminoisobutyric acid units. We use Monte Carlo simulations to determine peptide arrangements and folding. We then perform NMR chemical shifts calculations and compare to experimental measurements to validate the predicted structure.

The native -1 oxidation state can be oxidized into 0 and to +1 charge states. The neutral charge state is paramagnetic and behaves quite differently than the anion as manifested by the NMR spectra. The objective is to calculate NMR chemical shits, compare to experiment, and obtain insight into the electronic origin of these shifts. We also use DFT to simulate ENDOR spectra. Finally, we investigate the frontier molecular orbital arrangement in different charge states and determine the HOMO – LUMO energy gap and identify its fingerprint in the optical absorption spectra.

Electronic Structure Calculations of Monolayer–Protected Gold NanoClusters to Aid Spectroscopic Analysis

Neranjan Vikum Perera

B.Sc (Chem) Sp., University of Peradeniya, Sri Lanka

A dissertation

Submitted in Partial Fulfilment of the

Requirement for the Degree of

Doctor of Philosophy

at the

University of Connecticut

2015

APPROVAL PAGE

Doctor of Philosophy Dissertation

Electronic Structure Calculations of Monolayer–Protected Gold NanoClusters to Aid Spectroscopic Analysis

Presented by

Neranjan Vikum Perera, B.Sc. (Chem) Sp.

Major Advisor …….

Dr. Jose A. Gascon

Associate Advisor ……

Dr. Robert R. Birge

Associate Advisor ……

Dr. Steven L. Suib

Associate Advisor …….

Dr. Edward J. Neth

Associate Advisor …….

Dr. Alfredo Angeles-Boza

University of Connecticut

2015

I dedicated this to my dearest mother

Sirima Jayawardene

for her unconditional love and guidance

Acknowledgments

I am deeply grateful to my major advisor, Dr. Jose A. Gascón for giving me an opportunity to study in the field of computational chemistry, and for the guidance throughout the course of my Ph.D. program. He introduced me to the field of theoretical chemistry. It has been a long journey and I thank him for the patience and dedication shown towards me in my years at University of Connecticut to full fill my goal.

A special thanks to Dr. Robert R. Birge for his guidance towards quantum mechanics and the insights towards the theoretical chemistry. I would always cherish the courses which I took under him, and for the valuable discussions. I thank my thesis committee, Dr. Robert R. Birge, Dr. Steven Suib, Dr. Edward Neth and Dr. Alfredo Angeles-Boza for their valuable inputs.

Thanks to former and current members of Gascón lab for their support and help given towards me during my stay, and specially Dr. Lochana Mennikarachchi. Also I want to thank group members in Dr. Birge lab for the helping hand and the friendship given to me during these years.

A special thanks for my wife Vindya for her loving patience and the courage given to me during my difficult periods and been there for me in my life journey. I also want to remember my family members who helped me to be what I am today.

My mother has been the driving force for all my success in life, she introduced me to the world of chemistry. I own the world to her. She was a proud and courageous person which I always look upon. I know if she was here today, she would be the most happiest to hear me finish up my studies, and I miss her dearly. I am also grateful for my grandmother who looked after me and was behind me in my childhood. If they were here today they would be very proud of me today.

Table of Contents

Chapter 1. Introduction

1.1 Identification of Gold Nanoclusters

Gold nanoparticles are of fundamental and of practical interest. Their characteristic properties and electronic structure are strongly related to the nature of the cluster's dimensions. Extensive studies done over the years have revealed that their physicochemical properties differ dramatically from the corresponding bulk material and are strongly dependent on the size of the clusters. Gold nanoparticles, when approaching the de Broglie wavelength of the order of 1 nm range, exhibit novel properties which are quite different from the properties of their bulk counterparts with diameters over 5 nm [1]. In recent years, a renewed interest has emerged in the study and utilization of these materials as building blocks due to the novelty and the controllability of their properties.

To date, the reported gold clusters can be divided into i) bare gold clusters, and ii) ligand stabilized clusters. Bare gold anion clusters, which present transitions from planar to cage to pyramid like structures, have been well studied [2–12]. In the last decade, ligand stabilized gold clusters have gained much more interest than bare cluster due to their ability to form monodisperse particles. This provided excellent handling and functionalization chemistry with ease of preparation and separation into distinct core sizes, forming well-ordered crystal structures [13].

1.2 Role of ligands in nanoparticles

The ligand adsorbates perform a multirole towards the stability of the nanoparticles. They lower the free energy of the surface and therefore the reactivity of the particles. Ligand adsorbates also act as a physical barrier that prevents the cluster cores from direct contact. Another property of the ligand adsorbates is that their surface charge can be changed, using different functional

groups, which leads to the change in stability towards aggregation of the particles [14, 15]. In other words, energetic stability is promoted by charge–charge interactions and steric repulsion between particles to prevent the system from forming large aggregates. In the formation of monolayers, the ligands interact dynamically with the nanoparticles, and the amount of ligands on the nanoparticles depends on the relative rate of adsorption and desorption. Chemisorbed species have a low rate of desorption compared to the physisorbed species. This low rate of desorption causes the nanoparticles to grow slowly making the particle size smaller. In contrast, the ligands in semiconductors, metaloxides are adsorbed through physisorption where they are kept together by the Van der Waals forces and weak electrostatic forces.

The introduction of thiolated as ligands provides unique properties and is the most common way of adding a protecting monolayer to gold nanoclusters. These thiol ligands have a higher specificity to transition metals. Due to the low desorption rates, they are mainly used to control the size of the nanoparticles in the size range of < 5 nm. To form larger nanoparticles in the range of greater than 5 nm, phosphines and cetyltrimethylammonium bromide (CTAB) need to be used.

1.3 Structure determination of gold clusters

The quest for finding the complete structure of these small gold nanoparticles and the nature of the thiol gold bond has been the subject of intense scientific study for more than a decade. The finding of the x-ray crystal structure of the 102 gold atom nanoparticle with a 1.5 nm diameter was a major breakthrough by Kornberg in 2007 [16]. The high resolution structure of 1.1 Å showed a cluster of gold atoms surrounded by 44 thiolate ligands. The finding of this structure was of the utmost importance as it identified the precise composition and the arrangement of atoms around

the gold cluster. In particular, the structure revealed gold capped semi-ring motifs (usually referred as **staple motifs**) of –RS–Au–SR and –SR–Au–SR–Au–SR–. The emergence of the semi ring-like structure supported the theoretical work done by Hakkinen [17], which showed the novel binding mode of thiolates to gold clusters.

The precise identification of the crystal structure also led to the identification of this Au_{102} nanoparticle having molecule-like properties. Analysis of its electronic structure was also interpreted using a superatom analogy, in which the system is stabilized by the filling of electron shells. This super atom idea led the quest towards identifying much smaller stable nanoparticles with different cluster sizes. Preferential clusters with 18, 21, 25, 32 and 39 were identified as relatively stable compounds compared to the other sized clusters [18]. This also lead theoreticians to predict and evaluate a number or spectral and electronic properties with the available structural data. In particular, the cluster $Au_{25}SR_{18}$ (with, R a generic ligand) emerged as an interesting target due to ease of preparation into monodisperse particles.

Initial misidentification of the $Au_{25}L_{18}$ structure as $Au_{28}(SG)_{16}$ [13, 18, 19] and $Au_{38}(SCH_2CH_2Ph)_{24}$ [20] led to a series of experimental [1, 19] and theoretical results [21–23] based on this composition. The separation into fractions using polyacrylamide gel electrophoresis (PAGE) and identification using electrospray ionization mass spectrometry (ESI – MS) led to the relabeling of $Au_{28}(SG)_{16}$ as $Au_{25}(SG)_{18}$ [24]. Then the Au_{38} nanoparticle was rediscovered as an anionic species [25, 26] and the correct composition as $Au_{25}(SCH_2CH_2Ph)_{18}$ by mass spectroscopy [27]. This was accented with the total crystal structure determination [28, 29] of the salt $[Oct_4N^+][Au_{25}(SCH_2CH_2Ph)_{18}^-]$, which coincided with the DFT prediction of the structure [30].

The breakthrough of the X-ray crystal structures also revealed the nature of the ligand shell conformation. It showed that they diverge from the head – down ligand [31] arrangement typical

of planar surfaces. In the structure of Au_{25}, the nanoparticle is arranged around a core of 13 gold atoms, with a central gold atom surrounded by twelve gold atoms in an icosahedron arrangement as shown in Figure 1.1. Then the icosahedron is surrounded by six – SR–Au–SR–Au–SR– dimeric staples ($Au_2(SR)_3$). The gold atoms in the cluster can be categorized into three groups. The central gold atom has a coordination number of twelve. It is surrounded by twelve icosahedral atoms with a coordination number of six. In the third group, gold atoms are stellar atoms connected to the thiols; these gold atoms have a coordination number of two. The ligands in the semi–rings can be categorized into two environments depending on the proximity towards the core structure. The ligands, residing near the core structure are the inner ligands and the ligands residing far from the core are the outer ligands. The neutral form of the crystal structure was later discovered and it also showed the same basic structural arrangement as the original crystal structure [32].

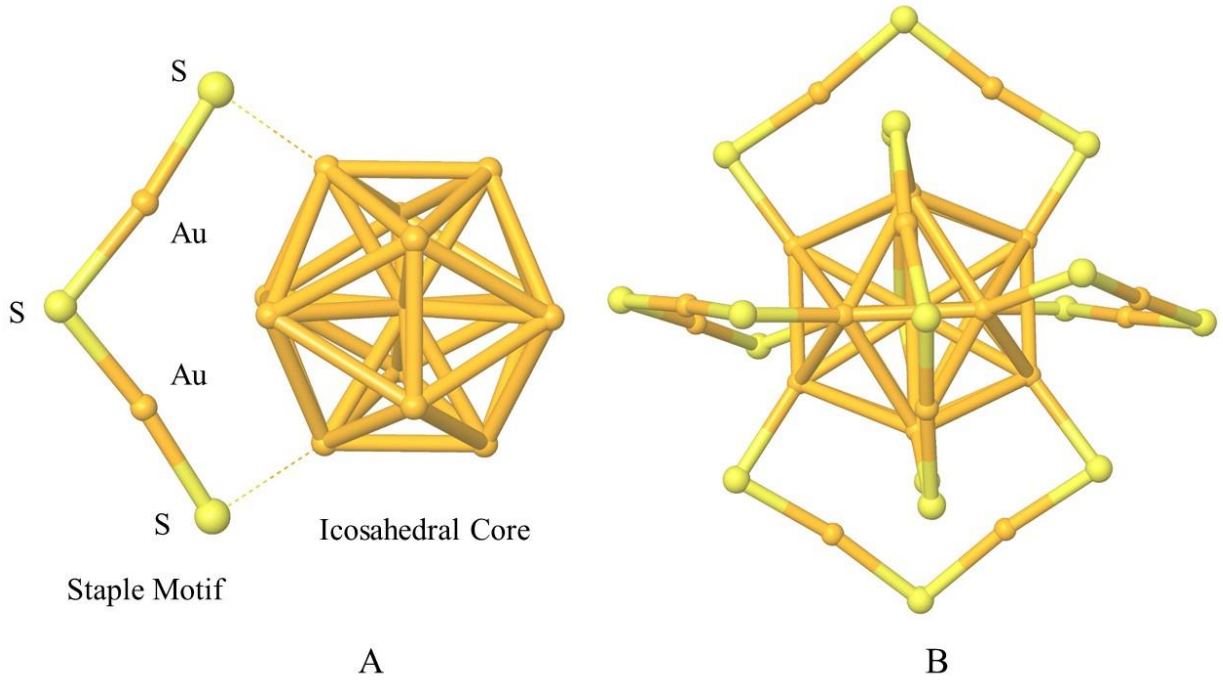

Figure 1.1: Arrangement of gold and Sulfur atoms in the gold 25 cluster. A) Central gold atom surrounded by 12 gold atoms in an icosahedral arrangement. The dimeric staple motif composed of ring like –S–Au–S–Au–S– structure is attached to the gold core through two Au–S bonds. B) $Au_{25}L_{18}$ structure composed of six ring–like staple motifs surrounding the gold core

1.4 Analytical Properties of Nanoclusters

Gold nanoparticles are of fundamental and practical interest. The physicochemical properties of gold change with the size of the clusters, from bulk to nanoparticles. The deep red color in colloidal gold particles originates from a single absorption peak at 2.5 eV (520 nm) due to the coherent oscillation of the conduction electrons [1, 33], known as plasmon resonance [29, 34–36]. This peak is, however, absent in smaller nanoparticles with protected ligands. Optical absorption spectra of ligand protected clusters exhibit multiple absorption peaks characteristic of quantum sized effects [9]. The discreet electronic levels in these clusters differ from the spectra in the bulk continuum. Nanoclusters with different sizes will exhibit distinct optical properties due to the electronic structure variations. Electrochemical experiments show these are molecular-like electronic states with a distinct HOMO–LUMO gap [37–39]. This suggests the gold nanoparticles should be highly stable and chemically inert. The ultra-small nanoparticles are also known to show luminescence [1] and fluorescence. It is still unclear the origin of fluorescence in gold nanoparticles but it is believed that two major sources are responsible. One is the metal core and its quantization effects due to the ultra-small size and the other rising from the surface interaction of the metal core with the surrounding ligands [40].

Smaller nanoparticles, commonly known as nanoclusters, also exhibit distinct properties. They also have promised potential applications ranging from quantum electronics to biomedical applications. With the discovery of high activity towards selective compounds by Haruta [5], the catalytic property of these small nanoparticles was showcased. Catalytic properties ranged from selective oxidation of CO, oxidation decomposition of amines, hydrogenation of: CO_2, carbonyl compounds, and alkynes along with reactions with nitrogen oxides [41–43]. The fluorescence properties of gold nanoparticles are used for biomedical tagging in tumor detection [44]. Other

uses for these gold nanoparticles are gene regulation [45], selective binding to DNA, biology catalysis and in nanotechnology [43].

1.5 Computational methods used

Computational models play an important role in understanding modern chemistry reactions and mechanisms. These models are developed using mathematical equations. The concepts derived from the basic principles lend chemist a helping hand to analyze and interpret results. With the technological advances, computers came into the limelight in running electronic structure calculations in model systems.

In this thesis, the computational methods used can be divided into two. Molecular quantum mechanics, developed from the ab inito (Latin for: from the beginning) molecular orbital theory, and molecular dynamics or Monte Carlo methods that use molecular mechanics force fields.

1.5.1 Molecular Quantum Mechanics

One of the starting points of quantum mechanics was the observation of the phenomena of wave particle duality, which describes the particle as having a dual behavior and it can act as matter as well as wave in nature. Due to this dual nature, it was postulated that matter such as electrons and molecules can be described by a wave function. A wave function, $\psi(r,t)$, describes the position (r) of the wave in a 3-D space at a given time (t), and this describes all its observable properties. For an electron, information on every observable can be extracted from the wave function solving the Schrödinger equation (1.1)

$$H\Psi = E\Psi \qquad 1.1$$

where H is the Hamiltonian operator, representing all the forces in the system. Schrödinger's equation represents a particular situation where the operator acting on a function will give the wave function multiplied by a constant. By solving the Schrödinger equation with force operator on the wave function, it will give back the wave function with energy (E).

The Hamiltonian operator can be written as;

$$\mathrm{H}= -\sum_i \frac{\hbar^2}{2m_e}\nabla_i^2 - \sum_k \frac{\hbar^2}{2m_k}\nabla_k^2 - \sum_i \sum_k \frac{e^2 Z_k}{r_{ik}} + \sum_{i<j} \frac{e^2}{r_{ij}} + \sum_{k<l} \frac{e^2 Z_k Z_l}{r_{kl}} \qquad 1.2$$

where *i, j* run over electrons, *k, l* run over nuclei, m_e is the mass of the electrons m_k is the mass of the nucleus *k*, ∇^2 is the Laplacian operator, *e* is the charge on the electron, *Z* is the atomic number, and r_{ij} is the distance between particle *i* and *j*. In the above equation, the first term is the operator for the kinetic energy of the electrons, the second term is the operator for the kinetic of the nuclei, the third term represents the coulomb attraction between electrons and nuclei, the forth term represent the repulsion between electrons and the fifth term represents the repulsion between nuclei respectively.

The Schrödinger equation cannot be solved exactly for any system but for the simplest systems (containing two interacting particles). To solve the equation in general, we use a well-defined approximation and solve to get an approximate solution. In order to achieve this, we use the Born-Oppenheimer approximation. As the electrons move much faster than the nuclei and are much lighter, we will therefore treat the nuclear and electronic motion entirely independently. As the nuclei are fixed, the kinetic energy of the nuclei can be considered as a constant and the Hamiltonian will now be treated as the electronic Hamiltonian, which has the form:

$$H_e = -\sum_i \frac{\hbar^2}{2m_e}\nabla_i^2 - \sum_i \sum_k \frac{e^2 Z_k}{r_{ik}} + \sum_{i<j} \frac{e^2}{r_{ij}} \quad 1.3$$

In the Born – Oppenheimer approximation, we fix the nuclei (R = $r_{l,k}$) and carry out the calculations to obtain the total energy and the wave function for the R. Then repeat for different values of R to obtain the complete potential energy surface by solving the electronic equation.

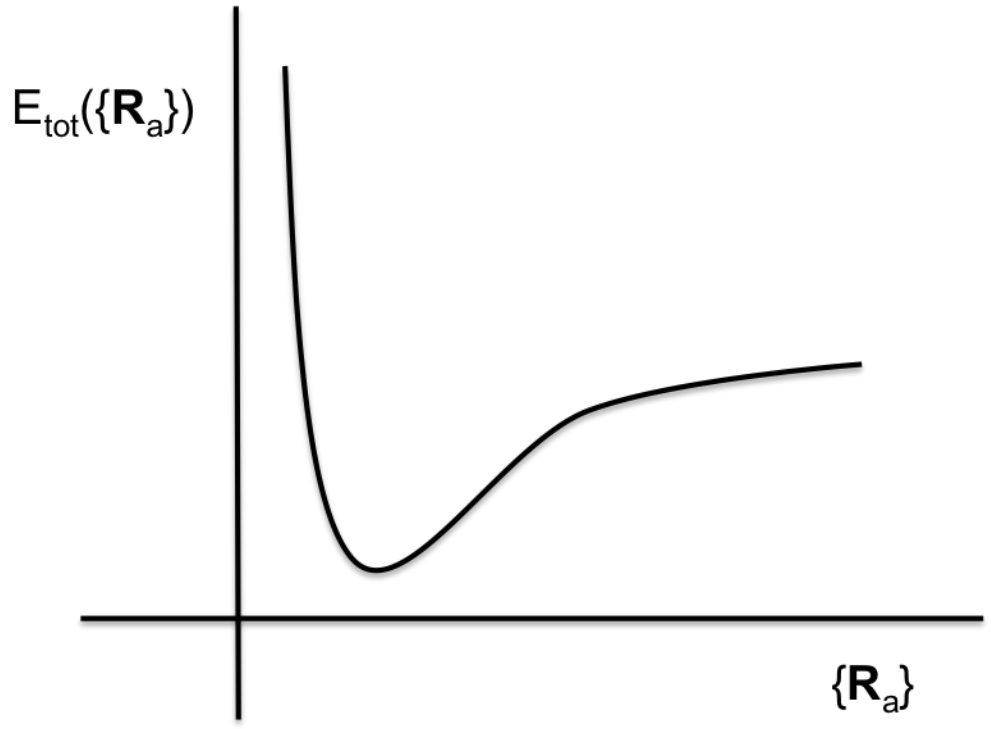

Figure 1.2: schematic diagram of the potential energy surface parametrized by the position of the nuclei.

1.6 Thesis Objectives and Organization

The underlying goal of this thesis dissertation is to simulate small MPCs via quantum mechanics and molecular mechanics calculations to derive electronic, structural, and dynamical properties. We specifically focus on monolayers consisting of thiolated oligopeptides and alkanethiols. The research carried out, which emphasizes the aid of experimental measurements via computations, focused on the following objectives:

1. Characterization of MPC with conformational constrained peptides (Chapter 2).

We construct MPCs with a layer of oligopeptides consisting of α-aminoisobutyric acid units. We use Monte Carlo simulations to determine peptide arrangements and folding. We then perform NMR chemical shifts calculations and compare to experimental measurements to validate the predicted structure.

2. Effect of charge state in $Au_{25}[L]_{18}^{z}$ (z= -1, 0, +1) as revealed by NMR and EPR calculations (Chapter 3).

Native -1 oxidation state can be oxidized into 0 and to +1 charge states. The neutral charge state is paramagnetic and behaves quite differently than the anion as manifested by the NMR spectra. The objective is to calculate NMR chemical shits, compare to experiment, and obtain insight into the electronic origin of these shifts. We also use DFT to simulate ENDOR spectra.

3. Effect of spin state in the electronic structure of $Au_{25}[SCH_3]_{18}^{z}$ (Chapter 4).

We investigate the frontier molecular orbital arrangement in different charge states and determine the HOMO – LUMO energy gap and identify its fingerprint in the optical absorption spectra.

Chapter 2

Characterization of Monolayer Protected Clusters with Conformational Constrained Peptides

Selected portions of the material presented in this chapter were published in:

Neranjan V. Perera, William Isley, Flavio Maran, Jose A. Gascón, Monolayer Modeling Characterization of a Conformationally Constrained Monolayer-Protected Gold Cluster. *Journal of Physical Chemistry C*. 2010, 114, 16043 – 16050.

Chapter 2. Characterization of Monolayer Protected Clusters with Conformational Constrained Peptides

2.1 Introduction

Recent advances in ultra-small gold nanoclusters have directed the focus towards potential applications ranging from quantum electronics to biomedical applications. The discovery of catalytic activity by Huruta [5] gave a new meaning to this emerging field of study. The new found catalytic activities ranged from selective oxidation of CO, hydrogenation of: CO2, α–β unsaturated ketones and aldehydes with carbonyl groups, alkynes along with cross coupling reactions, and amination reactions to direct nitrene insertion reactions. This diverse range of applications created attention directed towards the understanding and development of this new field of gold nanoparticles, which are also known as monolayer protected gold clusters (MPCs).

Exploiting MPCs for applications in the area of catalysis requires a proper structural and dynamical characterization of the physical properties of the protecting layer [46–48]. For some time there has been a misidentification on the composition of the small nanoparticles. This has been a major issue, where the composition would determine the structural arrangement in the interface of gold – ligand as well as in the protecting layer, where it would determine the activity of these MPCs. The total structure determination of a larger cluster size of Au_{102}(p-MBA)$_{44}$ was able to show the first glimpse into the nature of Au–S bonding at the interface. The structure revealed two types of staple motifs (figure 2.1), which are responsible for the attachment of the ligand groups towards the gold core. The recent breakthrough was contradictory to the commonly assumed head – down ligand arrangement once assumed in the layered material. At this point in

time, it was still unclear whether the staple motif was common towards larger, more complex ligands (e.g., ligands composed of polypeptides).

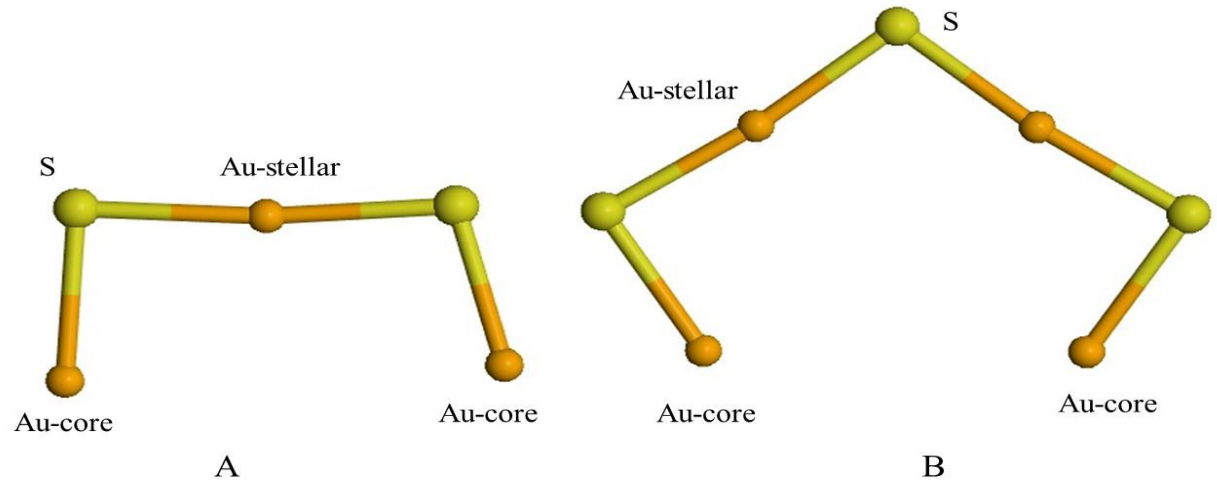

Figure 2.1: Staple motifs. The total structure determination of $Au_{102}(p\text{-}MBA)_{44}$ crystal structure [16] revealed two different types of Sulfur–Gold interactions in the form of two different staple motifs are responsible for the monolayer of ligands to attached to the gold core. A) Monomeric staple motif. B) Dimeric staple motif.

Stability of the formed monolayer depends on the chemical bonding of the ligand thiol groups to gold atoms and the non-bonding interactions between the adjacent ligand groups. The non-bonding interactions, which govern between ligand groups, are of two main types: hydrophobic interactions, which are mainly due to the van der Waals forces, and hydrophilic interactions are mainly due to the H-bonding between ligand groups. Recently, a new series of gold nanoclusters with oligopeptides were synthesized and characterized by Fabris et al [47]. The protecting oligopeptides were based on α-aminoisobutyric acid (Aib) units, where the N-terminus was thiolated to facilitate the bonding towards gold cluster and the C-terminus was capped with

N-*t*-butyl amide group as the protecting group. Aib units form intra molecular H-bonds between C=O --- H-N groups, where they adopt a 3_{10} - helical arrangement [49].

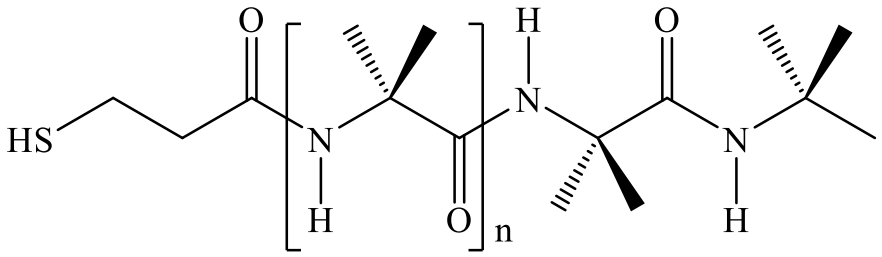

Figure 2.2: α-aminoisobutyric acid (Aib Unit) with the repeating unit, where n = 0, 1, 2,….etc At the same time Aib units form intra H–bonds, with N-H – O=C group which equal to the value n.

Aib oligopeptides form helical structures common to amino acid peptides. In the case of Aib oligopolymers, they form a rigid 3_{10} helical arrangement for very short polymers starting from tri peptides, whereas α-helical structures are formed with only long chains of α-amino acid units. In 3_{10} helices each intra molecular H-bond formed with *i* and *i* + 3 residues (figure 2.2 and figure 2.3) and the single turn is accomplished with 3.24 residues, while α-helices form a single turn using 3.64 residues. Aib polymers are accompanied with a strong dipole moment along the back bone, opposed to the simple alkane thiolates. The flexibility in alkane thiolates increase with the number of units while the Aib polymers are kept rigidly with inter and intra H-bonds. Studies have shown the formed 3_{10} helical structures are kept intact in liquid as well as in solid state [50, 51]. The Aib polymers are also shown to form layered structures in gold surfaces and in gold nano clusters as well [47].

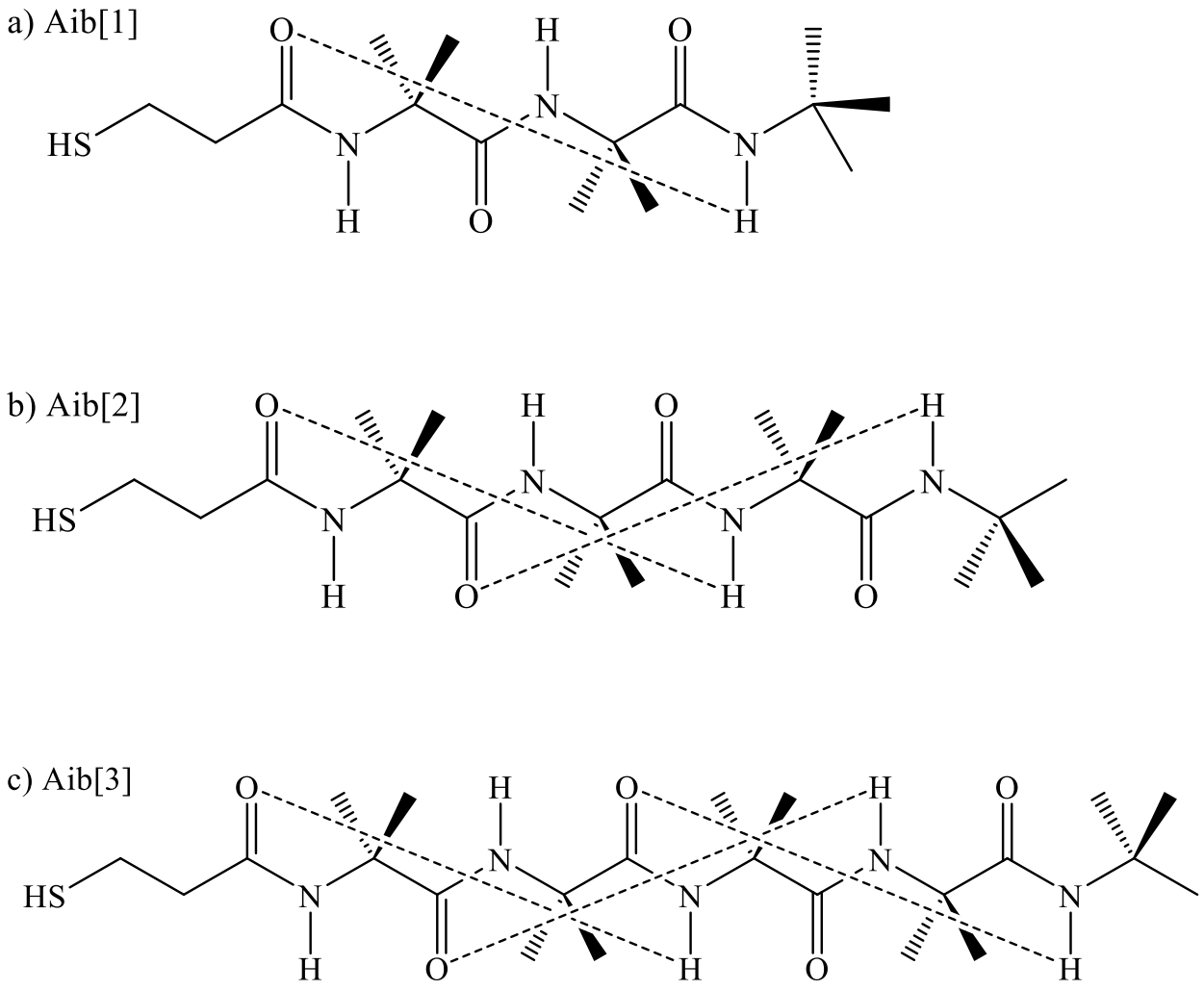

Figure 2.3: Thiolated α-amino isobutyric acid (Aib) peptides labeled according to their number of intra H-bonds. a) Intra molecular H- bonds n=1 Aib[1] b) intra molecular H- bonds n=2 Aib[2] c) intra molecular H- bonds n=3 Aib[3]

Maran and coworkers were able to synthesis and characterize monolayer protected gold nanoparticles containing Aib polymers using ^{1}H NMR spectrometry, IR and UV absorption spectroscopies, transmission electron microscopy (TEM), thermo gravimetric analysis and X-ray photoelectron spectroscopy techniques. The constructed nanoparticles showed an average core diameter of 1.1 – 2.3 nm, while the thermo gravimetric calculated surface coverage showed the smallest clusters formed have the average formula of $Au_{38}L_{18}$. More recent finding showed the formula of $Au_{38}L_{18}$ is a misinterpretation of mass spectroscopy data; the formula should be corrected to $Au_{25}L_{18}$.

Characterization of the above study was done with the assumption of the standard model and not considered the staple motifs. It is important to study the effect with the staple motif to conclude if such arrangement is consistent with the new model. A more fundamental question still arises about the nature of the inter peptide interactions. To answer this question, it is important to construct atomistic models to study and simulate this behavior. The study we are undertaking is the first of this kind, investigating large oligopeptides with functional groups. Many previous studies have investigated the small ligand groups and alkane thiolates where there are no self-interactions and inter H-bonds. Our construction of Aib protected gold nano cluster is mainly guided by the H NMR and IR experimental results, where we try to interpret the structural features using this model.

2.2 Computational models and methods

Our main goal is to build the atomistic model to simulate the structural features in the monolayer of the gold nano cluster. We use the Aib oligopeptides as the ligand group in the monolayer and formula can be denoted as follows:

$$Au_kAib[n]_m \quad 2.1$$

The *k* is the number of gold atoms associated with the gold cluster, *n* is the number of intra molecular H-bonds and *m* corresponds to the *n* + 1 Aib units. As in the actual experiment, the C-terminus are capped with *t*-butyl amide group to produce a realistic simulation.

Theory Level. Density functional theory (DFT) with the hybrid functional Becke, 3-parameter, Lee-Yang-Parr (B3LYP) was carried out to determine the structure of small Au_k-Aib templates as well as for the calculation of ^{1}H NMR chemical shifts. The valance double zeta polarized basis set 6-31g** was used for all atoms other than Au. Effective core potential of LACVP* was used for gold in $Au_{38}Aib[1]_2$ when the Jaguar package [52] was used and LANL2DZ effective core potential was used in all other calculations with the Gaussian 09 package [53]. In the construction of the model $Au_{25}Aib[3]_{18}$, molecular dynamic simulations was used with the Amber99 force field with the use of the Tinker package [54], while the ^{1}H NMR calculations were done using Gaussian 09.

Au_k template. A quantum mechanical description of the full system of atoms composed of around ~1400 atoms including heavy atoms, is computationally not a feasible task considering the computational time required for multi-configuration sampling. However, a correct description on the Au–S bonding interaction is needed to guide the construction of the full system. With that in mind, we constructed a small template of Au_3–SCH_3 to describe the bonding nature between the Au–S atoms. The model system of Au_3–SCH_3 shows that the sulfur atom binds in between two gold atoms in a bridging mode, which appears a general feature in thiolated gold clusters. Next, a more realistic description of the ligand is simulated using the actual Aib[3] ligand in Au_3–Aib[3], where it shows the same bridging mode result as in Au_3–SCH_3 (figure 2.4).

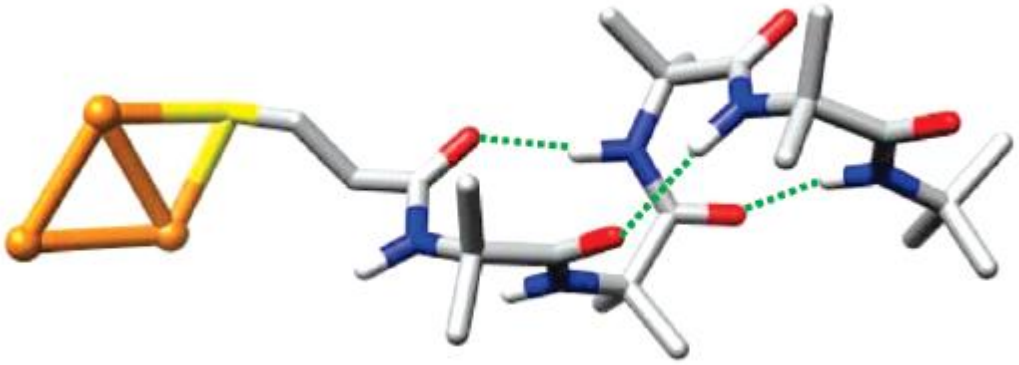

Figure 2.4: Template Au_3-Aib[3] showing the bridging binding mode of S atom to two gold atoms.

Au_{38}(Aib[1]$_2$). The Au_{38}–Aib[1]$_2$ model was constructed using the high symmetry Au38 core. The bare Au38 cluster was prepared with Oh symmetry and optimized at DFT level. Our main objective was to check whether the staple motif would emerge in a highly packed, high symmetry structure. By using the Au_3-Aib[3] model as a guide on how to place the ligand on the surface of Au38, we placed the two Aib[1] ligands at various distances from each other. QM optimizations where the run using Jaguar.

Au_{25}Aib[3]$_{18}$. Au_{25}–Aib[3]$_{18}$ was constructed using the known crystal structure of $[Oct_4N^+][Au_{25}(SCH_2CH_2Ph)_{18}^-]$ as the template. Since a SCH_2CH_2 group is common to the template and the thiolated Aib, the Aib was superimposed into the template to construct the model structure of Au_{25}Aib[3]$_{18}$. The constructed structure contained 1393 atoms including the 25 gold atoms.

Simulated Annealing via Monte Carlo. Construction of the model structure of $Au_{25}Aib[3]_{18}$, using the known crystal structure and the superimposition procedure mentioned above, quickly lead to steric clashes between neighboring groups. Therefore, a Monte Carlo procedure was implemented to relieve these interactions and to search for a low energy conformer in the potential energy surface. Due to the structural features of the Aib oligopolymer, Aib oligopolymers tend to form inter H-bonds with the adjacent ligand. Indeed, the ability of the oligopolymers to fold with each other is a unique feature in this type of monolayers, which is not present in monolayers with regular alkane thiolate ligands, where hydrophobic van der Waals forces dominate.

During this Mote Carlo procedure, we assume the gold atoms in the cluster and the S atoms attached to the cluster to be fixed. The force field employed in the procedure takes the total system to be neutral. We kept the charge of the gold atoms as zero, while the van der Waals parameters (σ = 2.394 Å, ε = 0.0039 kcal/mol) were taken from the universal force field [55] (UFF). Since Sulfur atoms are fixed to Au, we only had to define new angle bending parameters to Au – S – C (k_θ = 51 kcal/mol , θ_0 = 105^o). These parameters were roughly estimated so the Molecular Mechanics optimized geometry of the template and the vibrational frequency of that particular mode reproduced those obtained at the DFT level. For the parameterization of the α-aminoisobutyric acid (bonded and van der Waals), we used similarities with molecules which are already parameterized in Amber99 [56] (for example, parameters for cysteine and alanine residues). The electrostatic potential chargers (ESP) for Aib groups were derived from the DFT calculation done using B3LYP functional and 6-31g* basis set.

Metropolis algorithm was employed during the Monte Carlo procedure. Where the moves were carried out changing three dihedral angles, which are associated with the bonds Au–S–C–C, S–C–C–C and C–C–C–O. During the moves, the integrity of Aib was kept intact by keeping the

other internal coordinates frozen. The dihedrals were randomly moved within an internal of ± 20°, and the moves were accepted with a probability *p* where:

$$p = \min\left[1, \frac{\exp\left(\frac{-E_2}{k_B T}\right)}{\exp\left(\frac{-E_1}{k_B T}\right)}\right]$$

Where k_B is the Boltzmann constant, T is the temperature in Kelvin, and E_1 and E_2 are the energies of the system before and after the move, respectively. During the random move, if the energy E_2 is less than E_1 the move is always accepted. If the E_2 is higher in energy, the p is compared with a random number (*z*) from 0 to 1and the move is accepted if $p \geq z$. Typically around 20,000 Monte Carlo cycles were carried out, which each cycle consisting of 3 x 18 moves. After each Monte Carlo cycle, the temperature was decreased constantly from an initial value of 3000 K to a final value of 0 K. The program TINKER [54] was used minimization the system at the end of the Monte Carlo procedure.

NMR Calculations. ^{1}H NMR shielding constants were computed using Gauge Including Atomic Orbitals (GIAO) [57–61] implemented in Gaussian09 with Tetra Methyl Silane (TMS) as the reference. To compute ^{1}H NMR chemical shifts for the entire Au_{25}-Aib$[3]_{18}$, 18 calculations were carried out separately in the gas phase. If a given Aib was found hydrogen bonded with another one, the entire pair was extracted from the cluster. After capping the two sulfur atoms, DFT energy minimizations were carried out on each pair maintaining the S–S distance fixed. On the resulting structure, NMR calculations were carried out in the gas phase. On the other hand, if an Aib was not forming an intramolecular hydrogen bond, then it was extracted, capped, optimized and the NMR calculation was done in the gas phase for that Aib alone.

2.3 Results and Discussion

We have presented a molecular modeling study to uncover the physical and chemical properties of small gold nanoclusters protected by α-aminoisobutyric acid oligopeptide units. The α-aminoisobutyric acid units form very stable 3_{10}-helices, making them rigid structures. The study was motivated by the recent breakthrough in X-ray crystal structure, where Kornberg et al. showed the "staple motif" as a novel bonding interaction between gold and thiols. At this time, it is still unclear if this novel binding mode is common to all types of thiolate ligands and ligand monolayers with inter bonding interactions. Thus, we constructed a series of atomistic models to simulate the structural changes in the gold cluster after incorporating Aib oligopeptide ligands. In order to study the structural variations, we use the experimental ^{1}H NMR spectroscopic data as a fingerprint to validate certain structural features.

The recent discovery of the staple motif in gold clusters with small ligands drove us to check the feasibility of the staple motifs in high symmetrical structures as well as with large oligopeptides. Au38 was chosen with this intention. The Au38 is a high symmetrical structure with O_h symmetry. Au38 structure was chosen instead of Au25 to test whether the staple motif could emerge from such a compact structure. As described in the methods section, the two Aibs were placed at various distances from each other so that interpeptide H–bond was feasible. After full DFT relaxation two distinct stable conformations were found. In one case the cluster was slightly distorted, and in the other, the staple motif emerged during the course of optimization. Remarkably, the structure with the staple motif was roughly 20 kcal/mol more stable than the other conformation (figure 2.5). The result obtained was remarkable as it suggested that a staple motif is also common to MPC consisting of long chain polymers with inter peptide H–bonds.

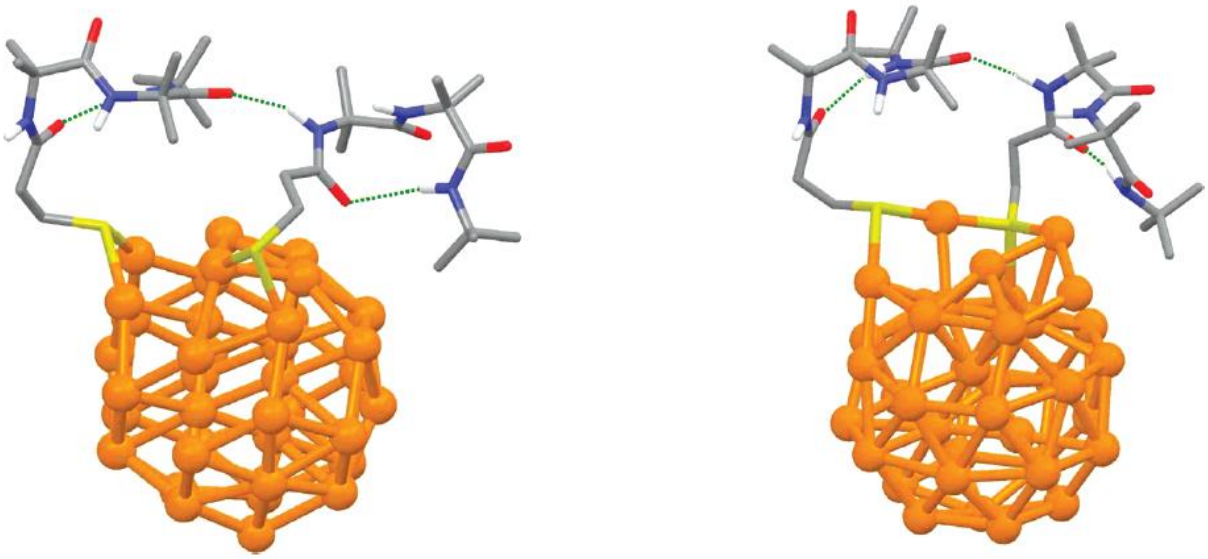

Figure 2.5: DFT minimum energy structure of Au_{38}-Aib[1]$_2$ showing two possible stable conformations. The case on the left side corresponds to the standard motif, with the Au surface unaffected. The other case corresponds to the staple motif, which is much lower in energy.

Simulated Annealing

Having shown that the staple motif is also common in gold cluster bound to larger oligopeptides peptides, we now turn into a more realistic representation of the monolayer with 18 Aib ligands. Monte Carlo simulation followed by the energy minimization of $Au_{25}Aib[3]_{18}$ show a closely packed monolayer (Figure 2.6). The common assumption in which rigid Aib peptides align perpendicular to the surface can no longer. The structure shows that, driven by interligand hydrogen bond interactions, peptides arrange in a folded manner, contrary to the more perpendicular way expected for alkanethiol ligands. It is important to note that the resulted model structure of $Au_{25}Aib[3]_{18}$ was able to maintain the structural integrity of all 3_{10} helical arrangements during the Monte Carlo procedure and after the energy minimization, where it preserved its intra hydrogen bonds (hbonds). However, the resulting structure was only able to accommodate only 6 out of 18 potential H-bonds. This hbonds are expected to form between a C=O oxygen of one ligand and the amide NH(1) group of the donor ligand (figure 2.7). While the acceptor Oxygen atoms varied across the ligand pairs, four were made with the oxygen O(4) (thus, the most common) one with O(3) and one with O(1). This findings give the idea that the general trend of inter H-bond formation is between NH(1) group of one peptide ligand, and carbonyl O(4) of a neighboring peptide ligand. This is an important discovery concerning the structure of the monolayer, which was not clear initially. Figure 2.7 further shows that there are neighboring steric repulsions of methyl groups competing with the H-bond formation in a typical H-bonded pair of Aib ligands.

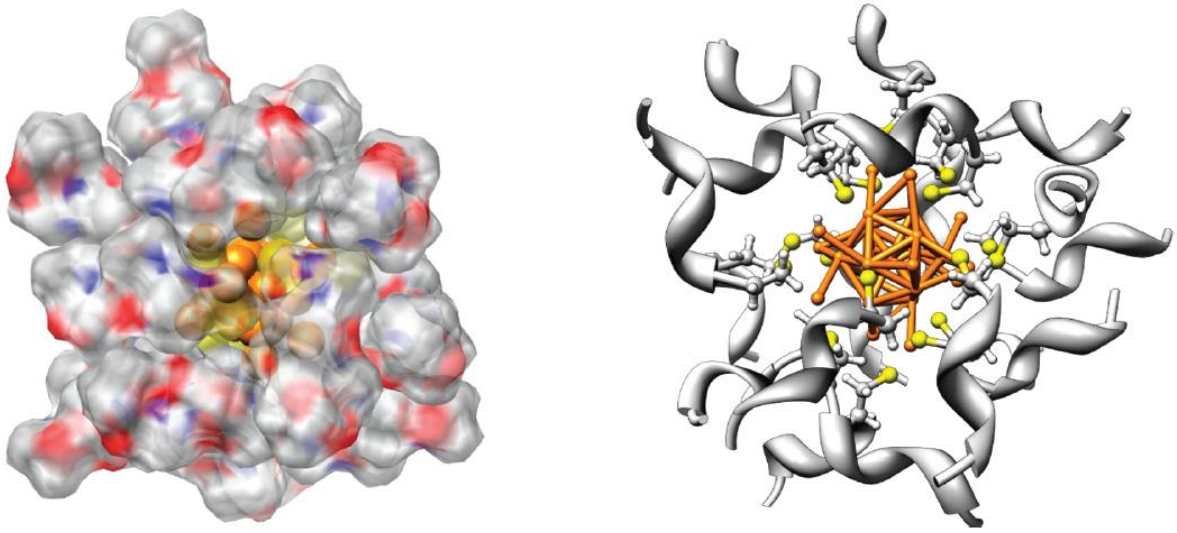

Figure 2.6: The surface representation (left) of the Au_{25}-Aib[3]$_{18}$ showing the Aib ligands protecting the gold core and the ribbon representation (right) of Au_{25}-Aib[3]$_{18}$. Driven by interligand hydrogen bond interactions, peptides arrange in a folded manner, contrary to the more perpendicular way expected for alkanethiol ligands.

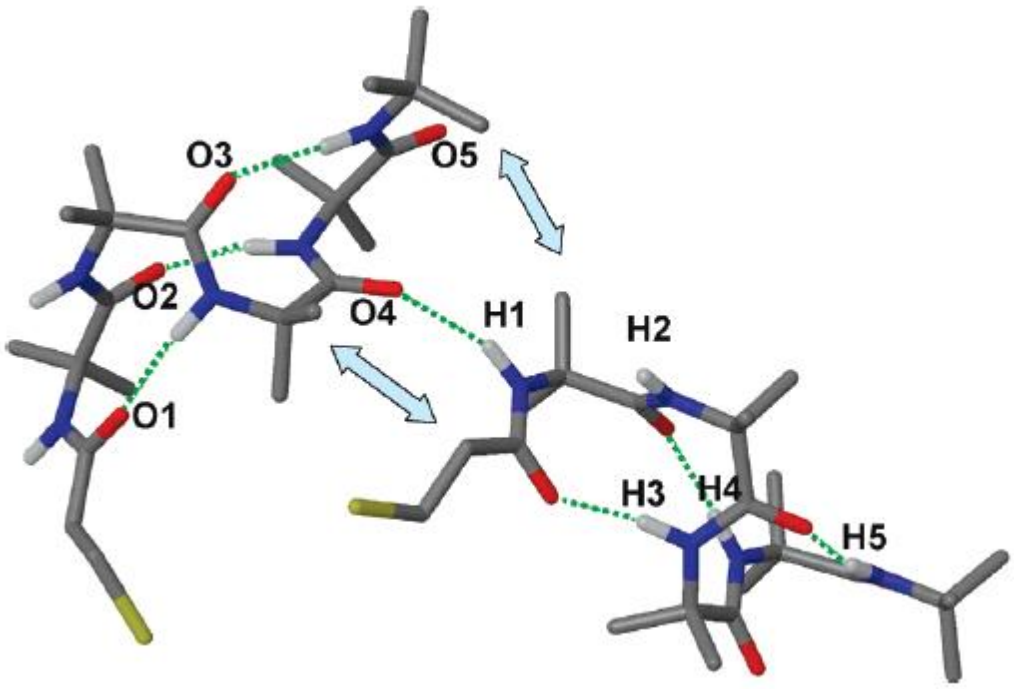

Figure 2.7: A typical hydrogen-bonded Aib[3] pair. Most of the donor – acceptor pairs involve H(1) with O(4). Double arrows distinguish competing steric interactions.

^{1}H NMR

^{1}H NMR spectroscopy was used to evaluate the integrity of the peptides by identifying the relevant molecular interactions involving H-bonds. Experimental studies carried out on free Aib[3] peptides confirmed that the amide protons NH(1) and NH(2) do not form intra H-bonds. NH(1) is sensitive towards solvent interactions as well as NH(2), although this last one on a lesser extent. This hypothesis was tested when a solution of Aib[3] was titrated with Me_2SO-d_6, a H-bond acceptor capable of making H-bonds with polar groups. When the concentration of Me_2SO-d_6 was increased, the ^{1}H NMR chemical shift of NH(1) moved downfield compared to the NH(2) while the other amide protons had little effect on the addition. The initial conclusion was that the solvent molecules formed inter H-bonds with the amide group of NH(1) readily and to a lesser extent with NH(2), while the other amide groups were not affected due to the stable 3_{10}-helical arrangement. When the same experiment was done with the Aib ligands attached to gold clusters, no change in the ^{1}H NMR chemical shift was observed upon the addition of Me_2SO-d_6. The Me_2SO-d_6 was unable to form bonds with the amide groups in the ligand, but the ^{1}H NMR of the MPC **still showed a downfield shifted** NH(1) group compared to the other protons. This observation suggests that all 18 NH(1) groups are involved in hbonds.

The next step was to evaluate the chemical shift using the model structure of $Au_{25}Aib[3]_{18}$ found in by the Monte Carlo procedure. We recall that the resulted structure of $Au_{25}Aib[3]_{18}$ from the simulated annealing contained 6 out of 18 possible hydrogen bonds. Calculated chemical shifts (Table 1) for those 6 ligands show a very good agreement with the experimental chemical shifts. Intra molecular H-bond distances for NH(3) to NH(5) are typical values for Aib oligo polymers of similar length, which can be also accounted for from x-ray diffraction data[49, 62] and DFT calculations [63–65].

Table 1: calculated and experimental ^{1}H NMR chemical shifts (in ppm) for the Aib Amide Protons in the complex of $Au_{25}Aib[3]_{18}$

	H(1)	H(2)	H(3)	H(4)	H(5)
Au3-Aib[3]-Alanine					
calculated shift	7.95	6.07	7.64	7.01	6.85
O--H distance Å	2.05[a]		2.09[b]	2.18[b]	2.21[b]
Au3-Aib[3]18					
calculated total average	5.9 ± 1.5	6.1 ± 0.2	7.5 ± 0.2	7.0 ± 0.1	6.8 ± 0.1
calculated single Aib	4.9 ± 0.1	6.1 ± 0.2	7.4 ± 0.1	6.9 ± 0.05	6.8 ± 0.1
calculated H-bonded Aib	7.9 ± 0.3	6.0 ± 0.2	7.7 ± 0.2	7.1 ± 0.1	6.8 ± 0.1
avg O--H distance Å	2.05 ± 0.08[a]		2.12 ± 0.03[b]	2.19 ± 0.02[b]	2.23 ± 0.01[b]
experiment	8.8	6.8	7.6	7.4	7.3

[a] inter H-bond distance [b] intra H-bond distance

The calculated O---H bond distances correlates with the trend in ^{1}H NMR chemical shift of amide protons. It can be seen from both Table 1 and figure 2.8, (experimental and calculated) the upfield shift when moving from NH(1) to NH(3) and from NH(3) to NH(5), which correlates with the increase in bond distances. It is a known fact that the strength of H-bonds go hand in hand with the H-bond distance. It appears that inter chain H–bond in the peptide MPC is even stronger than the inter molecular H–bonds between peptides, which is also true in β–sheets where it forms shorter O --- H bond distances relative to α–helices [66]. It is worth mentioning that the particular strength of the inter chain H-bond was experimentally evidenced also by IR absorption analysis [47] of the amide A region of the Aib-peptide MPCs, where a low frequency component at 3287 ± 5 cm^{-1} was attributed to the N-H groups H-bonded to neighbor peptides.

So far, we have established that, according to experiments, the amide proton NH(1) group make inter H–bonds. The simulated model structure reveals that the most probable bonding occurs

between NH(1) and O(4) of a neighboring ligand group. When we look at the figure 2.8, it clearly shows our model is lacking the necessary inter H-bonds to move the average shift more down field. In other words the model structure after Monte Carlo simulation did not arrive at a global minima, presumably having 18 inter H-bonds according to the experimental results. However, if we just consider the Aib groups which made inter H-bonds, as shown in red squares in figure 2.8, we would fall into the ideal situation, when the calculated chemical bond trend would go hand in hand with the experimental results. Still, the calculated shifts are down fielded versus the experimental values, since the inter chain H-bonds must compete with the van der Waals interaction, and such a discrepancy is not unexpected when using the current DFT functional.

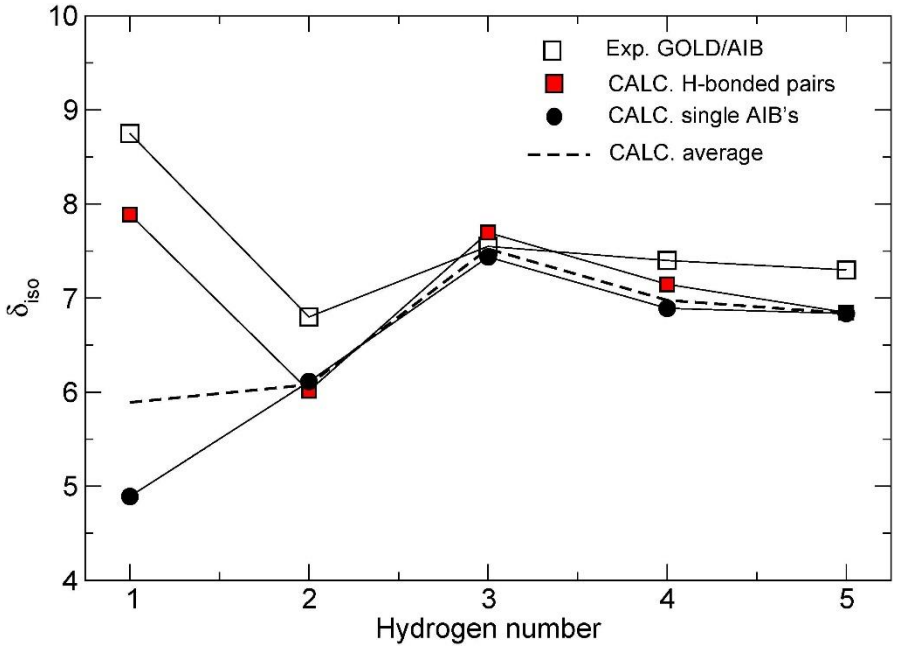

Figure 2.8: DFT calculation of ^{1}H isotropic chemical shielding for the structure of Au_{25}-Aib[**3**]$_{18}$. Contributions from different Aib's, whether they form hydrogen bond pairs or not, are explicitly separated. Chemical shieldings are referred with respect to TMS. Experimental values are also reported[47].

2.4 Conclusions

In this part of the research, we have constructed a series of atomistic models of Aib-monolayer protected gold clusters. The newly discovered staple motif seems to be a common denominator in small alkane ligand gold clusters as well as with large constrained peptide ligands. With the conformation of the new binding mode, we constructed the model structure of $Au_{25}Aib[3]_{18}$ using the X-ray crystal structure. The search of a global minima was driven by the folding of ligands through simulated annealing. Inter peptide nonbonding interactions dominated the ligand folding in the monolayer, where the attraction forces of H-bonding had to compete with the steric repulsion between the methyl groups. All the ligands kept the 3_{10}-helical arrangement during the folding process and folded into the ligand network, opposing the earlier thought of perpendicular alignment of ligands.

The minimized structure was able to correctly correlate with the experimental ^{1}H NMR chemical shift values. The model structure gave an insight into the nature of the interactions between the Aib ligands, which the initial experimental results were unable to do so. However, this structure underestimated the number of inter H-bonds between the ligands, showing it might not have achieved its global minima. Future work is underway to drive the ligand cluster towards the global minimum, where it would form more inter H-bonds.

Chapter 3

Effect of charge state (z = -1, 0, +1) on the nuclear magnetic resonance of monodisperse $Au_{25}[S(CH_2)_2Ph]_{18}^{z}$ clusters

Selected portions of the material presented in this chapter were published in:

Venzo, A.; Antonello, S.; Gascón, J. A.; Guryanov, I.; Leapman, R. D.; **Perera, N. V.**; Sousa, A.; Zamuner, M.; Zanella, A.; Maran, F. Effect of the Charge State (z = -1, 0, +1) on the Nuclear Magnetic Resonance of Monodisperse $Au_{25}[S(CH_2)_2Ph]_{18}^{(z)}$ Clusters. *Analytical Chemistry*. **2011**, *83*, 6355–6362.

Dainese, T.; Antonello, S.; Gascón, J. A.; Pan, F.; **Perera, N. V**.; Ruzzi, M.; Venzo, A.; Zoleo, A.; Rissanen, K.; Maran, F. $Au_{25}(SEt)_{18}$, A Nearly Naked Thiolate-Protected Au_{25} Cluster: Structural Analysis by Single Crystal X-ray Crystallography and Electron Nuclear Double Resonance. *ACS Nano*. **2014**, *8*, 3904–3912.

Chapter 3. Effect of charge state (z = -1, 0, +1) on the nuclear magnetic resonance of monodisperse $Au_{25}[S(CH_2)_2Ph]_{18}^z$ clusters

3.1 Introduction

$Au_{25}L_{18}$ has a distinct optical characteristics due to its molecular like behavior. A new insight into its structural characteristics was given by Murray[28] and Jin[29] with the identification of the crystal structure in its native form. This new $Au_{25}L_{18}$ crystal structure shared similar features with the previous $Au_{102}L_{44}$ crystal structure [16]. Both the structures shared the "staple motif" of Au_2L_3, an iconic feature in ultra-small thiolated gold clusters. At the same time theoretical prediction of the structure of $Au_{25}(SCH_3)_{18}$ also led to the finding of the staple motif parallel to the experimental crystal structure [30]. Where the $Au_{25}(SCH_3)_{18}$ was found to be protected by six staple motifs composed of $Au_2(SCH_3)_3$ complexes. Due to the position of these capping ligands, they either can be termed as outer ligands or inner ligands as shown in the Figure 3.1. The 6 outer ligands are attached to two stellar gold atoms and kept away from the gold core, while the 12 inner ligands are kept closer to the core and each is attached to one stellar and one core gold atom.

Although the finding of the Au25 crystal structure has shed light into understanding the physicochemical properties of the gold clusters, some important physical aspects are still unclear to the scientists at this time. One important aspect which had eluded interpretation was the dependence of the NMR peaks on different charge states. An initial NMR study was done by Murray and coworkers using ethyl phenyls as ligands [67]. They showed that the chemical shift values for α, β methylene protons (α, β refer to the positions relative to the Sulfur atom) and phenyl protons have different magnitudes depending on their position relative to the cluster. The native crystal structure of $Au_{25}L_{18}^-$ showed a broad peak at ~3.17 ppm for both types of ligand groups

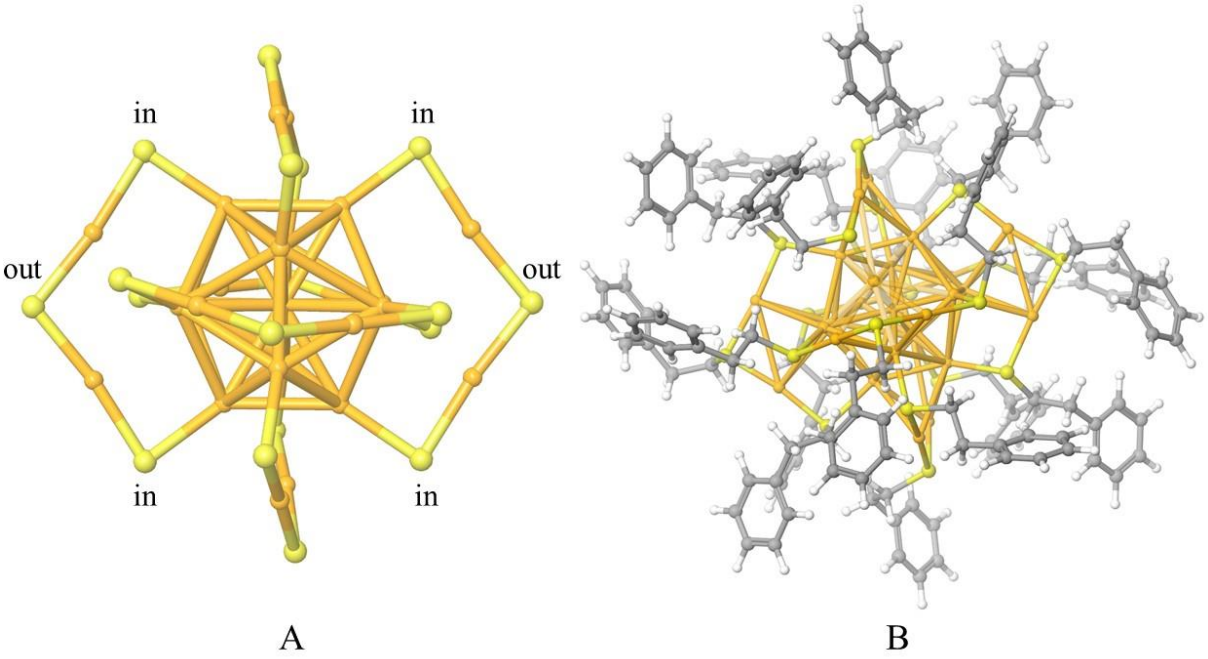

Figure 3.1: The structure of $Au_{25}(SCH_2CH_2Ph)_{18}$ gold atoms in orange, Sulfur atoms in Yellow, Carbon atoms in Gray and Hydrogen atoms in white. A) Showing the staple motifs binding to the Au_{13} core. Where the inner (in) and outer (out) ligands attached to gold core is shown. B) Total structure with Ethyl phenyl ligands attached through the thiol ligand are shown.

and upon oxidation the peak shifted downfield towards ~5.13 ppm. The β–CH_2 groups, on the other hand showed two different peak positions.

One of the ligand types showed a peak at 2.99 ppm and the other a broad peak at ~3.8 to ~3.65 ppm; upon oxidation, the peak broadens and collapses. In their study, they were unable to do a full interpretation of the splitting and broadening of β–CH_2 protons. The ^{13}C NMR spectra of $Au_{25}L_{18}^{0}$ and $Au_{25}L_{18}^{+}$ upon oxidation of native $Au_{25}L_{18}^{-}$ showed the relevant peaks become scattered and then begin to coalesce.

The small core dimension of the Au25 core, with discrete energy levels give rise to a molecule-like one electron redox processes [67–69]. The redox process of electron transfer can be characterized by the cyclic voltammetry (CV) and differential pulse voltammetry (DPV) techniques [31, 38]. It has been found that the peak separation between the oxidation and reduction peaks can be varied with the various substitution in the capping ligands [51, 70]. As several aspects of the redox behavior are still unexplored, using the actual crystal structures with its capping ligands as the starting point is a key step in the identification of the physicochemical properties of these clusters.

In our computational approach, we use the available crystal structures as the starting point and try to understand the dependence of NMR peaks on different charge states using DFT calculations. Clusters with different charge states were obtained by our experimental colleagues (Maran's Group, University of Padova). They used electron transfer (ET) methods, which provided a clean, efficient and controllable method of making redox charge states of $Au_{25}L_{18}^{-}$, $Au_{25}L_{18}^{0}$ and $Au_{25}L_{18}^{+}$ using monodisperse clusters. The prepared redox species where fully characterized using ^{1}H NMR and ^{13}C NMR spectroscopy methods. Experimental data together with DFT calculations of NMR shifts provided a way to clarify the structural finding of two ligand populations in the

monolayer of clusters. In turn, each ligand population showed distinct NMR patterns. $Au_{25}L_{18}^{0}$ cluster has an unpaired electron, making it stand apart from the rest of the redox species. The neutral paramagnetic cluster showed a fascinating picture in the NMR spectra. For the neutral species in particular, we tried to understand and interpret its behavior and try to uncover the dependence of NMR towards different charge states.

The unique features of the paramagnetic cluster was evident in the paramagnetic nuclear magnetic resonance (PNMR) spectrum. The chemical shift values of the two ligand populations were significantly affected by the spin density populations due to the unpaired electron. Careful observations showed the spin density populations are not symmetrically distributed around the gold core. In the ligands, where the spin densities showed a profound concentration, displayed a significant hyperfine shift, compared to the other ligands.

3.2 First Principle Calculations of Paramagnetic NMR shift

Calculating the NMR spectrum of paramagnetic species is a difficult task experimentally as well as theoretically. Paramagnetic NMR (PNMR) provides a tool to identify long range structural data information and the spin density distributions across the molecule. Bertini and coworkers [71, 72] pioneered the approach to obtain NMR shifts in paramagnetic species, which is now recognized as a reliable method.

In paramagnetic species the average induced electron magnetic moment contributes towards the chemical shift, which is known as the hyperfine shift. The interaction between the nuclear and electron magnetic moments give rise to new terms in the chemical shift. Now, the paramagnetic shift of nucleus *I* is composed of three main parts: orbital shift δ_O, the Fermi contact shift δ_{FC} and pseudo contact shift δ_{PC} [73].

$$\delta = \delta_O + \delta_{FC} + \delta_{PC} \quad 3.1$$

δ_O refers to the orbital, which is taken from the isotropic part of the shielding tensor (σ_O) and referenced with respect to the isotropic shielding tensor (σ_{ref}) of a diamagnetic reference compound (in this work, TMS): $\delta_O = \sigma_{ref} - \sigma_O$. The Fermi contact, $\delta_{FC,}$ arises from the scalar interaction between the nuclear magnetic moment of the resonate nucleus and the average spin density arising from the unpaired electron at the location of the nucleus. In its simplest form, the isotropic Fermi contact is given by the equation 3.2

$$\delta_{FC} = \frac{2\pi}{\gamma_I} g_e \mu_B A \frac{S(S+1)}{3kT} \quad 3.2$$

Where γ_I is the magnetogyric ratio of the nucleus *I*, g_e is the electron g factor, μ_B is the Bohr magneton, A is the isotropic hyperfine coupling constant and kT is the thermal energy. This equation holds for one unpaired electron located in a single orbital with no thermally accessible excited levels. The sign of δ_{FC} is dictated by the sign of *A*, and its magnitude may be very large for low γ nuclei but relatively small for ^{1}H nuclei. *A* is proportional to the spin density at the nucleus: $\rho_s(\mathbf{R}_I) = \rho^{\alpha}(\mathbf{R}_I) - \rho_s{}^{\beta}(\mathbf{R}_I)$, where $\rho^x(\mathbf{R}_I)$ involves all occupied molecular orbitals of spin *x*: $\rho^x(\mathbf{R}_I) = \sum_i \left|\Psi_i^x\right|^2$. Thus, an excess of alpha spin at position $\mathbf{R}_I$ produces a resonance of nucleus *I* at higher frequencies, while the opposite occurs for an excess of beta spin. A derivation of *A* is given in the next section.

The last term in Eq. 3.2 is due to the dipolar interaction between the induced magnetic moment arising from the unpaired spin and the magnetic moment of the nuclear spin. The equation

3.3 shows that the pseudo contact shift is proportional to the anisotropy of magnetic susceptibility tensor χ:

$$\delta_{PC} = \frac{1}{4\pi r^3}\left[(\chi_{zz} - \bar{\chi})\frac{2z^2-x^2-y^2}{2r^2} + (\chi_{xx} - \chi_{yy}) \times \frac{x^2-y^2}{2r^2} + \chi_{xy}\frac{2xy}{r^2} + \chi_{xz}\frac{2xz}{r^2} + \chi_{yz}\frac{2yz}{r^2}\right] \quad 3.3$$

where *r* is the separation between the magnetic moment and the observed nucleus, and χ_{ij} are the components of the χ tensor. Generally, the pseudocontact shift is negligible [74] in comparison with δ_{FC}, assumption that we adopt in this study.

Theory Level: for the calculations of NMR chemical shifts, the $Au_{25}(SCH_2CH_2Ph)_{18}^{-1}$ crystal structure was initially optimized by Jaguar and then finally by Gaussian 09 [75]. The hybrid functional B3LYP and LACVP pseudo potential for gold atoms and 6-31g(d) basis set for all other atoms was used in Jaguar. After the initial optimization, the structure was fully optimized using Gaussian 09 using the B3LYP functional and lanl2dz effective core potential for gold atoms and 6-31g basis set for all other atoms. The optimized structure was then used to calculate the paramagnetic NMR parameters using the GIAO method implemented in Gaussian 09. The B3LYP functional with lanl2dz effective core potential for gold and 6-31g(d,p) basis set for all other atoms was used in this calculation. Using the parameters calculated by Gaussian 09 we then calculated the paramagnetic shift for the H and C atoms. To calculate the reference orbital shift, TMS was used as the reference molecule.

3.2.1 Spin Density

In paramagnetic molecules the unpaired electron is not localized on a single nucleus or at a single point in space, but delocalized on the entire molecule. At a particular place, where the unpaired electron resides, it may have a non-zero electron magnetic moment in that particular

molecular orbital (MO). So the average electromagnetic moment felt by the nucleus will be proportional to the spin angular moment in the z-direction times the spin density (ρ). In here the spin density is the fraction of unpaired electrons at that point [71].

When an unpaired electron is residing near the core, it will interact with the paired electron and it will be polarized by the unpaired electron, this is called spin polarization. Due to this effect, the paired electron will modify its presence in such a way that the electron with spin aligned with the unpaired electron will have a slight preference to occupy the space of molecular orbital closer to the unpaired electron, while the electron with a anti parallel spin will have a slight preference to occupy the molecular orbital space away from the unpaired electron as shown in figure 3.2.

As stated, the spin density is not just the amount of unpaired electron residing at the nuclear, but now it has a contribution, arising due to the spin polarization of paired electrons. Spin density on the nucleus can be positive or a negative quantity due to the spin polarization. When spin density is normalized for one electron, it is proportional to the contact coupling constant (A), a quantity which express how much the nucleus and the electron can sense each other.

$$A = \frac{2}{3}\,\mu_o\,\hbar\,\gamma_I\,g_e\,\mu_B\left[\rho^{\alpha}(R_I) - \rho^{\beta}(R_I)\right] \qquad 3.4$$

We employed Gaussian 09 with spin unrestricted DFT to calculate spin density values, (first proposed by Barth and Hedin [76]) where the excess spin density is related to the Fermi contact term [77]. According to the equation 3.2, the coupling constant can be a positive or negative quantity, depending whether the excess spin density is, α or β at the nucleus.

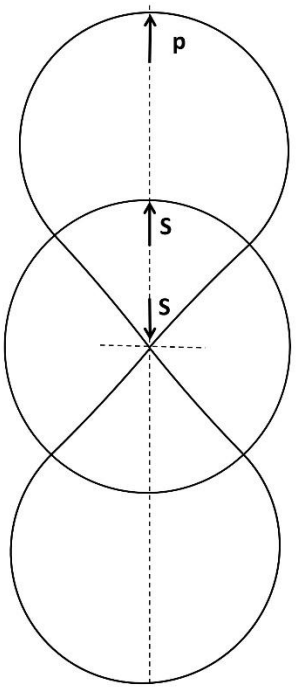

Figure 3.2: The unpaired electron in a *p* orbital affects the distribution of the two paired electrons in the s orbital, where the electron with spin aligned with the unpaired electron will have a slight preference to occupy the space of molecular orbital closer to the unpaired electron, while the electron with a anti parallel spin will have a slight preference to occupy the molecular orbital space away from the unpaired electron

3.3 Results and Discussion

According to the earlier work done by Murray and coworkers on $Au_{25}(SCH_2CH_2Ph)_{18}^{-1}$, they have identified two ligand families according to the chemical shift values of the CH_2 group. Upon oxidation to $Au_{25}(SCH_2CH_2Ph)_{18}^{0}$ both inner and outer α-CH_2 peaks shifted downfield from 3.13 ppm to 5.13ppm while the broad peak at 3.68 – 3.8 ppm of β-$(CH_2)_{in}$ disappeared. In order to revisit these observations, Maran and coworkers measured the ^{1}H and ^{13}C NMR data of $Au_{25}(SCH_2CH_2Ph)_{18}^{-1}$ and assigned the triplet at 2.93 ppm to β-$(CH_2)_{out}$, the complex peak around 3.1 ppm to be the overlap of two methylene protons of α-$(CH_2)_{out}$ and β-$(CH_2)_{in}$, and the remaining broad peak at 3.8 ppm to be due to of α-$(CH_2)_{in}$ [78]. The ^{13}C NMR results also confirmed the evidence to two ligand populations.

As described by Murray, the peak positions shifted upon oxidation towards $Au_{25}(SCH_2CH_2Ph)_{18}^{0}$. As expected, Maran and coworkers found the NMR spectrum to be quite complex due to the unpaired electron in the cluster. Upon oxidation, the peak at 3.1 ppm moved down field and the α-$(CH_2)_{out}$ towards 5.13 ppm and β–$(CH_2)_{in}$ towards 5.4 ppm. This shows that both the α-$(CH_2)_{out}$ and β–$(CH_2)_{in}$ peaks undergo significant downfield shift when $Au_{25}(SCH_2CH_2Ph)_{18}^{-1}$ is oxidized into $Au_{25}(SCH_2CH_2Ph)_{18}^{0}$. The two peaks were better resolved with temperature where the β–$(CH_2)_{in}$ peak becomes sharper and undergoes a slightly upfield shift with increase in temperature, and its integral becomes twice of the value of α-$(CH_2)_{out}$ which correlates with the ratio between the inner and outer ligands.

The behavior of the NMR shift can be further confirmed by the theoretical work. To simulate the NMR behavior, we constructed the two charge states starting from the crystal structures of $Au_{25}(SCH_2CH_2Ph)_{18}^{-1}$ and $Au_{25}(SCH_2CH_2Ph)_{18}^{0}$ [32]. ^{1}H NMR shift values of -1 cluster showed the expected spectral features, (Table 3.1) e.g., the dependence of the two ligand

types based on their position with respect to the gold core. Like the experimental value, the α-$(CH_2)_{out}$ and β-$(CH_2)_{in}$ showed a peak at ~3.1 ppm which, upon oxidation to $Au_{25}(SCH_2CH_2Ph)_{18}^0$, both shifted to 3.26 ppm and 5.55 ppm, respectively. Downfield shift of α-$(CH_2)_{out}$ was modeled exactly as in the experiment, whereas the downfield shift of β-$(CH_2)_{in}$ could not reproduce the experimental value.

Table 3.1: Calculated[a] average values and the experimental ^1H NMR values of $Au_{25}(SCH_2CH_2Ph)_{18}^{1-}$ and $Au_{25}(SCH_2CH_2Ph)_{18}^0$ clusters.

compound	temp (K)		α-CH_2	β-CH_2	o-CH	m-CH	p-CH
$Au_{25}L_{18}^{1-}$	δ cal	inner	3.68	3.31	7.77	7.89	7.85
		outer	3.28	3.64	8.11	7.96	7.84
$Au_{25}L_{18}^0$	δ cal(298)	inner	23.85	3.26	8.28	8.26	7.68
		outer	5.55	3.55	8.12	8.04	7.94

compound	solvent	temp (K)		α-CH_2	β-CH_2	o-CH	m-CH	p-CH
$Au_{25}L_{18}^{1-}$	CD_2Cl_2	δ exp(298)	inner	3.80	3.13	7.19	7.15	7.08
			outer	3.13	2.93	7.14	7.19	7.15
$Au_{25}L_{18}^0$	toluene-d_8	δ exp(298)	inner	24.9[d]	5.4[c]	7.42[c]	7.19	n.d
			outer	5.13	2.81	n.d	n.d	n.d
	toluene-d_8	δ exp(358)	inner	21.22	4.9	7.41	7.18	6.99
			outer	5.05	2.89	7.02	7.09	7.03
	C_6D_6	δ exp(298)	inner	n.d	5.47[d]	7.46[d]	7.20	6.99
			outer	5.14	t 2.86	6.99	7.05	6.97

n.d.= not determined. [a] Level of DFT used : B3LYP functional / LANL2DZ / 6-31g**, Calculated chemical shifts in ppm at 298 K. [c] Broad peak. [d] Very broad.

The most affected and interesting peak is the peak of α-$(CH_2)_{in}$ at 3.8 ppm. Which disappears as soon as it is partially oxidized. In CD_2Cl_2 solvent medium with increasing temperature, the peak becomes very broad at around 24.9 ppm. This significant broadening of the peak makes it undetectable through COSY even at high temperatures. A theoretical description becomes much more important in this circumstance. The calculated paramagnetic shift of 23.85 ppm value is obtained for the α-$(CH_2)_{in}$ proton, confirming the experimental downfield shifted proton. This assignment is one of several major breakthroughs in conforming the experimental assignment of the ^{1}H NMR peaks. The β-$(CH_2)_{out}$ shift is more or less unaffected by the oxidation where it remains at slightly upfield value of 2.81 ppm from its original value of 2.93 ppm. This behavior is exactly observed with our theoretical model as well, where the oxidized cluster showed the value at 3.55 compared to the 3.64 ppm value in the -1 cluster.

In the experimental ^{1}H NMR spectrum in the phenyl region of $Au_{25}(SCH_2CH_2Ph)_{18}^0$ cluster, the o- , m- and p-protons of the outer ligands appear at 7.02, 7.09 and 7.03 and the inner ligands appear at 7.41, 7.18 and 6.99 ppm. In the calculated spectrum of $Au_{25}(SCH_2CH_2Ph)_{18}^0$, the peaks of the outer protons appear at 8.12, 8.16 and 7.94 ppm and the inner ligands appear at 8.28, 8.26 and 7.68 ppm respectively. By comparison, the experimental inner ligand peak positions as well as the calculated ones appear slightly downfield compared to the outer ligand protons.

Table 3.2: Calculated[a] and experimental[b] paramagnetic ^{1}H NMR chemical shifts of inner and outer ligands of $Au_{25}(SCH_2CH_2Ph)_{18}^0$

inner	α-CH_2	β-CH_2	o-CH	m-CH	p-CH
1	8.26	1.69	7.24	8.51	6.64
2	2.92	3.66	8.73	8.23	8.06
3	9.86	3.88	7.88	8.10	7.93
4	38.98	2.72	8.83	8.42	7.43
5	78.16	3.88	8.72	7.86	7.96
6	5.59	3.42	8.33	8.38	8.05
7	2.64	3.69	8.71	8.25	8.04
8	7.97	1.52	7.29	8.61	6.65
9	37.97	2.91	8.78	8.42	7.44
10	11.00	3.89	7.86	8.13	7.96
11	5.69	3.51	8.34	8.37	8.05
12	77.12	4.29	8.68	7.91	7.96
Avg	23.85	3.26	8.28	8.26	7.68
exp(298)	24.9[d]	5.4[c]	7.42[c]	t 7.19	n.d
exp(358)	21.22[d]	4.9[c]	7.41	7.18	6.99

outer	α-CH_2	β-CH_2	o-CH	m-CH	p-CH
13	6.21	3.90	8.26	8.29	7.98
14	6.59	3.86	8.22	8.30	7.99
15	5.98	2.96	8.00	8.07	7.80
16	6.31	2.88	7.98	8.03	7.82
17	4.05	3.82	8.14	8.14	8.04
18	4.15	3.89	8.12	8.12	8.03
Avg	5.55	3.55	8.12	8.16	7.94
exp(298)	5.13	t 2.81	n.d	n.d	n.d
exp(358)	t 5.05	t 2.89	7.02	7.09	7.03

[a] Level of DFT used : B3LYP functional / LANL2DZ / 6-31g**, Calculated chemical shifts in ppm at 298 K. [b] Experimental values were determined in toluene-d_8 at 298K and 300 K (n.d. = not determined). [c] Broad peak. [d] Very broad.

Table 3.3: calculated and experimental ^{1}H NMR chemical shifts of inner and outer ligands of $Au_{25}(SCH_2CH_2Ph)_{18}^{1-}$ (B3LYP / 6-31g**/LANL2DZ)

inner	α-CH_2	β-CH_2	o-CH	m-CH	p-CH
1	3.27	3.15	6.72	7.55	7.69
2	3.71	3.71	8.75	8.38	8.06
3	3.81	3.86	8.78	8.40	8.08
4	3.37	3.11	6.73	7.55	7.69
5	3.54	2.98	7.24	7.43	7.67
6	3.71	3.62	8.37	8.01	7.76
7	3.71	3.58	8.29	7.97	7.73
8	3.40	2.97	7.11	7.37	7.61
9	3.89	2.74	7.33	7.91	7.94
10	4.10	3.74	8.36	8.17	8.04
11	3.96	3.67	8.36	8.14	7.98
12	3.67	2.61	7.26	7.85	7.91
Avg	3.68	3.31	7.77	7.89	7.85
exp(298)	3.80[d]	3.13	7.19	7.15	7.08

outer	α-CH_2	β-CH_2	o-CH	m-CH	p-CH
13	3.63	3.75	8.04	7.82	7.70
14	3.61	3.84	8.04	7.81	7.68
15	2.97	3.54	7.98	7.90	7.80
16	2.93	3.42	7.91	7.90	7.84
17	3.44	3.73	8.35	8.19	8.03
18	3.13	3.55	8.31	8.13	7.96
Avg	3.28	3.64	8.11	7.96	7.84
exp(298)	3.13	2.93	7.14	7.19	7.15

[a] Level of DFT used : B3LYP functional / LANL2DZ / 6-31g**. [b] Experimental values were determined in CD_2Cl_2 at 298K and 300 K (n.d. = not determined). [c] Broad peak. [d] Very broad.

Comparison of $Au_{25}(SCH_2CH_2Ph)_{18}^{1-}$ (Table 3.3) and $Au_{25}(SCH_2CH_2Ph)_{18}^{0}$ (Table 3.2) with the experimental values and calculated values provides a quantitative assessment of the ligand types in the monolayer. The calculated results provide a rational to the dramatic chemical shift values seen in the inner α-CH_2 experimentally, when the $Au_{25}(SCH_2CH_2Ph)_{18}$ cluster is oxidized from -1 to 0.

The ^{13}C NMR spectrum of $Au_{25}(SCH_2CH_2Ph)_{18}^{0}$ gives also evidence for a two ligand populations in the monolayer. The relative 13C NMR shift values of inner ligands are slightly downfield compared to the outer ligands as seen in table 3.4. This feature is observed in experimental values, and our calculated paramagnetic values agree with this. This peak difference is more prominent in quaternary C (*ipso*-C) and in *ortho* C. The experimental values of 140.05 and 129.57 ppm for outer ligands and 144.22 and 131.73 ppm for inner ligands were observed for *i*-C and *o*-C. This feature was reproduces in the DFT calculation where the outer ligands showed the values of 134.11 and 123.45 ppm while inner ligands had the value of 154.74 and 127.31 ppm respectively for *i*-C and *o*-C (Table 3.4). The effect of paramagnetism is evident for α-C_{in} and for β-C_{in} compared to the other ligands. For the inner C, the experimental values of -134 ppm and 350ppm were observed but satisfactory assignment could not be made. DFT calculations carried out on $Au_{25}(SCH_2CH_2Ph)_{18}^{0}$ cluster were able to solve the problem by successfully assigning the -134 ppm peak to the α-C_{in} and the 350 ppm shift to the β-C_{in}.

Table 3.4: Calculated[a] and experimental[b] paramagnetic ^{13}C NMR chemical shifts of inner and outer ligands of $Au_{25}(SCH_2CH_2Ph)_{18}^0$

inner	α-C	β-C	*i*-C	*o*-C	*m*-C	*p*-C
1	126.77	252.38	200.24	129.28	119.35	129.59
2	42.45	41.95	135.54	125.47	122.55	121.07
3	32.34	40.19	134.54	123.34	121.86	120.59
4	-87.54	230.71	187.69	136.97	120.92	126.32
5	59.94	104.96	125.76	125.94	123.41	120.38
6	49.84	66.50	139.97	123.74	122.65	121.67
7	41.80	41.68	135.53	125.17	122.64	121.38
8	127.50	263.51	203.57	130.02	119.62	130.33
9	-88.68	244.15	193.79	135.05	121.41	125.98
10	30.01	41.60	134.66	123.83	122.16	120.83
11	49.12	59.23	139.40	123.86	122.89	121.98
12	62.09	98.22	126.14	125.03	123.20	120.11
δavg	37.14	123.76	154.74	127.31	121.89	123.35
δexp[b]	-134.00[c]	350.00[c]	144.22	131.73	128.63	126.53

Outer	*α*-C	*β*-C	*i*-C	*o*-C	*m*-C	*p*-C
13	41.68	44.67	133.37	124.45	122.78	122.49
14	41.93	44.56	133.26	124.17	122.66	122.68
15	36.87	43.94	133.79	123.52	122.81	120.87
16	36.36	44.09	133.73	123.52	122.82	120.72
17	34.28	46.11	135.41	122.49	123.26	121.07
18	33.37	45.46	135.11	122.56	123.18	121.04
δavg	37.41	44.81	134.11	123.45	122.92	121.48
δexp[b]	39.00	47.71	140.05	129.57	128.16	126.41

[a] Level of DFT used : B3LYP functional / LANL2DZ / 6-31g**. Calculated chemical shifts in ppm at 300 K. [b] Experimental values were determined in toluene-d_8 at 358 K (n.d. = not determined). [c] Very broad peak.

Table 3.4: calculated and experimental ^{13}C NMR chemical shifts of inner and outer ligands of $Au_{25}(SCH_2CH_2Ph)_{18}^{1-}$

inner	α-C	β-C	*i*-C	*o*-C	*m*-C	*p*-C
1	43.76	43.71	136.77	123.43	122.43	118.78
2	44.04	45.38	139.33	124.41	122.50	120.19
3	44.15	45.46	139.39	124.44	122.50	120.21
4	43.68	43.23	136.76	123.32	122.43	118.90
5	43.40	40.79	135.28	124.49	121.69	118.97
6	41.92	44.69	138.80	124.29	122.12	120.11
7	41.85	44.64	138.60	123.72	122.32	120.22
8	43.66	40.49	135.37	124.51	121.69	118.96
9	41.94	39.83	136.13	124.89	121.66	119.94
10	43.53	44.18	138.78	123.41	122.65	120.20
11	43.16	44.06	138.84	123.75	122.35	119.60
12	42.18	40.16	136.04	124.72	121.66	119.79
avg	43.11	43.05	137.51	124.11	122.17	119.66
exp(298)	n.d	n.d	141.88	129.85	128.52	126.27

outer	α-C	β-C	*i*-C	*o*-C	*m*-C	*p*-C
13	42.92	43.64	137.35	123.21	122.51	119.87
14	43.43	44.27	137.48	123.20	122.49	119.82
15	42.91	43.62	137.99	123.45	122.12	119.58
16	42.83	43.63	137.77	123.41	122.31	119.94
17	41.25	43.41	138.03	123.89	122.36	120.19
18	40.61	43.76	137.98	123.91	122.21	119.76
avg	42.32	43.72	137.77	123.51	122.33	119.86
exp(298)	35.98	42.18	140.88	129.3	128.63	126.49

[a] Level of DFT used : B3LYP functional / LANL2DZ / 6-31g**. [b] Experimental values were determined in CD_2Cl_2 at 298K (n.d. = not determined).

From the observation of experimental and theoretical chemical shift it is evident that values of α-CH_2 in inner ligands show dramatic changes when the $Au_{25}(SCH_2CH_2Ph)_{18}^{1-}$ is oxidized to $Au_{25}(SCH_2CH_2Ph)_{18}^{0}$. The unpaired electron is the major influence towards these exceptional values in paramagnetic species. This effect is felt by the ^1H nuclei in close proximity to the gold core. The effect is quite significant for the ^1H nuclei the α-$(CH_2)_{in}$ while the effect is also evident in the β-$(CH_2)_{in}$ and α-$(CH_2)_{out}$ nucleus, but β-$(CH_2)_{out}$ nucleus is not affected. The same effect is also responsible for the significant shift in 13C NMR shift, where the α-C_{in} and β-C_{in} are the most affected nucleus in this case.

Calculations done on ^1H and ^{13}C NMR on the $Au_{25}(SCH_2CH_2Ph)_{18}^{0}$ cluster provide an insight into the significance of the shift, in particular about the origin of the two different ligand types in the monolayer. This behavior is attributed to the contact interaction of the nuclear magnetic moment, arising from the unpaired electron. A close inspection of the spin density give us a rationale to explain how the spin density delocalization around the affected nuclei is responsible for this interesting behavior.

A measure of this delocalization is to consider the spin density on the (α-C). The average spin density on $(\alpha\text{-C})_{in}$ is $0.0008\times\hbar/2$ whereas for $(\alpha\text{-C})_{out}$ is, on average, $0.00007\times \hbar /2$. Figure 3.3 provides a visual representation of such order of magnitude difference of inner versus outer ligands. For a spin isosurface of $0.0001\times \hbar /2$, no spin density is evident for outer ligands (Figure 3.3). This translates into a uniform set of chemical shifts in the region (33 – 46) ppm. For inner ligands the spin density clearly extends up to the (β-C) and, for some ligands, even to the phenyl groups (Figure 3.3). A closer inspection of the spin density of inner ligands shows that it presents a non-uniform distribution. For instance, an excess of alpha spin (Figure 3.4) can give rise to values ranging from 30 ppm to 130 ppm for $(\alpha\text{-C})_{in}$ and from 40 ppm to 260 ppm for $(\beta\text{-C})_{in}$. On the other

hand, an excess of beta spin, which only extends up to the $(\alpha\text{-C})_{in}$ is uniquely responsible for the negative chemical shifts (Figure 3.5). All these observation are consistent with the experimental data presented in Table 3.4. In addition, calculations reveal that the normal band in the 33 – 46 region, who originates mainly from the outer ligand alkenes, also has some minor contribution from both $(\alpha\text{-C})_{in}$ and $(\beta\text{-C})_{in}$.

Calculations of ^{1}H chemical shifts also show a strong correlation with the extent of spin delocalization as in the case of ^{13}C. That is, outer ligands behave remarkably different than inner ligands (see Figure 3.3 for representative values and Figure 3.6, Figure 3.7 for the histogram representation of inner and outer shift values). Different than the case of ^{13}C, however, $(\alpha\text{-CH}_2)_{out}$ and $(\beta\text{-CH}_2)_{out}$ present distinct distributions: one centered at ~ 5.55 ppm and the other at ~ 3.55 ppm. This agrees very well with the corresponding experimental values of 5.13 ppm and 2.81 ppm, respectively. $(\alpha\text{-CH}_2)_{out}$ are also more sensitive to temperature than $(\beta\text{-CH}_2)_{out}$ (Table 3.4), experiencing an upfield of –0.28 ppm after increasing the temperature to 358 K, in modest agreement with the experimentally observed shift (–0.08 ppm). Computed chemical shifts for $(\beta\text{-CH}_2)_{in}$ give rise to a small shift (+0.07 ppm), whereas the experimentally observed shift is (–0.5 ppm), suggesting that the extent of spin delocalization in underestimated at the current level of theory. $(\alpha\text{-CH}_2)_{in}$ exhibit the most noticeable effect. The computed average is 23.85 ppm at 298 K and 20.6 ppm at 358 K, in excellent agreement with the experimental values at these two temperatures (24.90 ppm and 21.22 ppm, respectively). This correspondence clearly demonstrates the paramagnetic behavior of $Au_{25}(SCH_2CH_2Ph)_{18}^{0}$ arising from the Fermi-contact term.

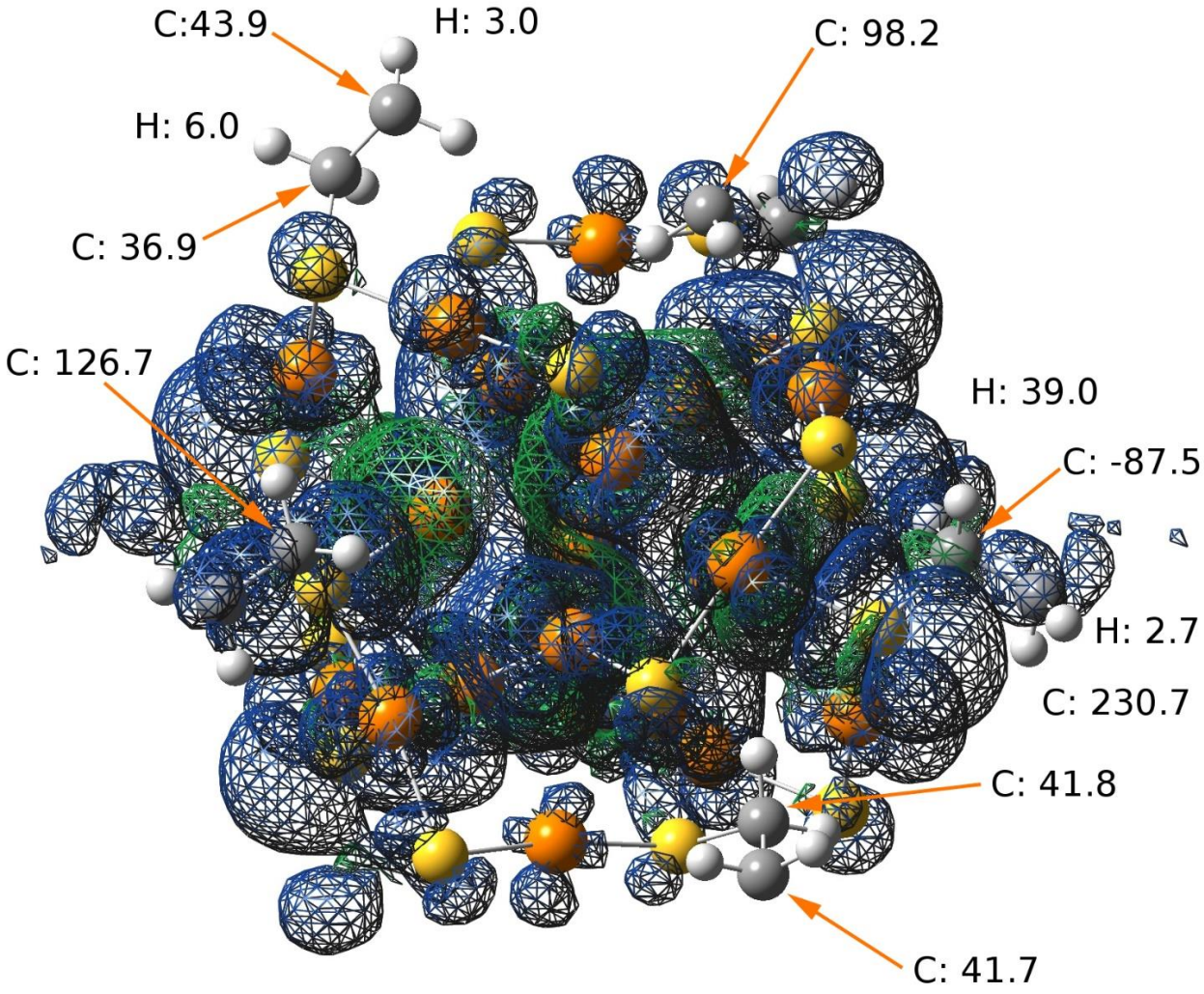

Figure 3.3: Isosurface of the electronic spin density of $Au_{25}(SCH_2CH_2Ph)_{18}^0$ (iso value = 0.0001). Blue and Green corresponds to α and β spin respectively. For clarity, only some of the ethyl groups are shown, and phenyl groups are not displayed. Gold, sulfur, carbon and hydrogen atoms are shown in orange, yellow, gray and while respectively. Typical values of calculated chemical shifts at 298K are shown.

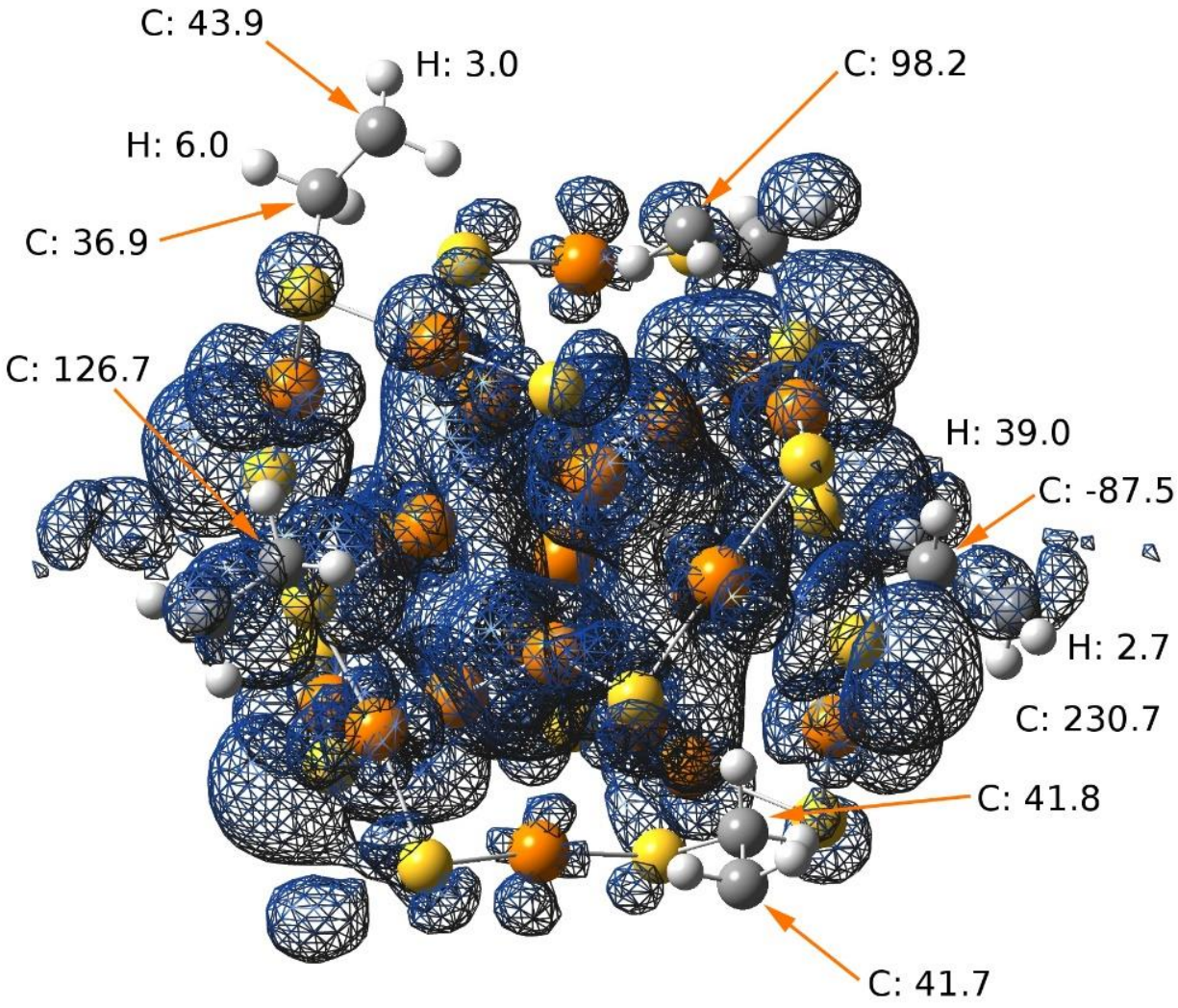

Figure 3.4: Alpha spin density of $Au_{25}(SCH_2CH_2Ph)_{18}^0$ and representative NMR chemical shifts at 298 K. For clarity only few of the ligands are shown. Phenyl groups are not displayed. Gold, sulfur, carbon and hydrogen atoms are shown in orange, yellow, gray and while respectively. Isosurface value = 0.0001

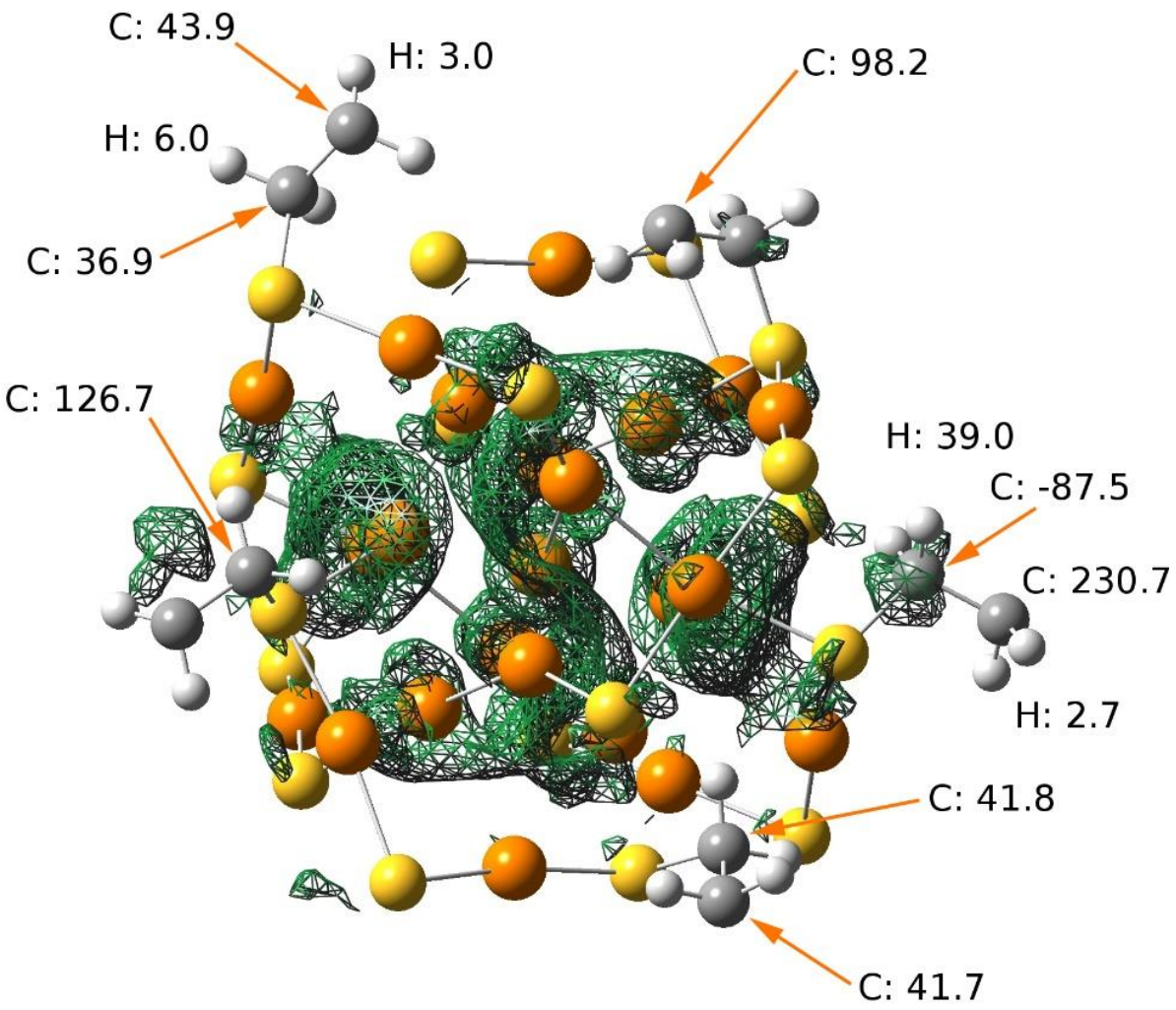

Figure 3.5: Beta spin density of $Au_{25}(SCH_2CH_2Ph)_{18}^0$ and representative NMR chemical shifts at 298 K. For clarity only few of the ligands are shown. Phenyl groups are not displayed. Gold, sulfur, carbon and hydrogen atoms are shown in orange, yellow, gray and while respectively. Isosurface value = 0.0001

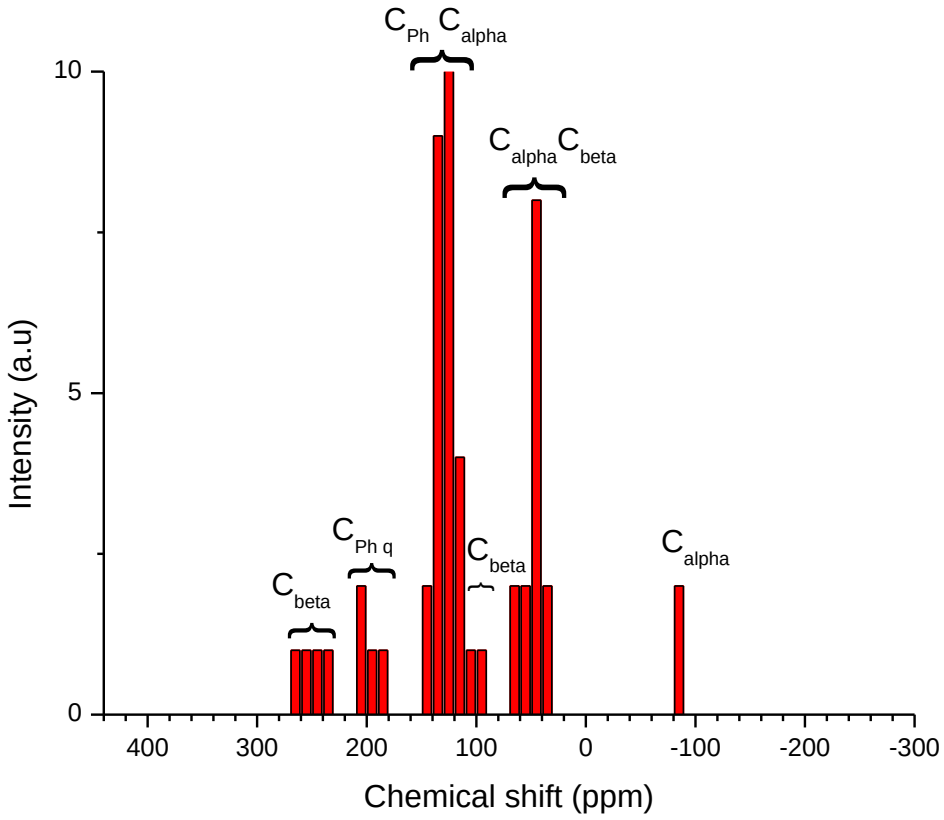

Figure 3.6: ^{13}C probability histogram of inner ligands in $Au_{25}(SCH_2CH_2Ph)_{18}^{0}$

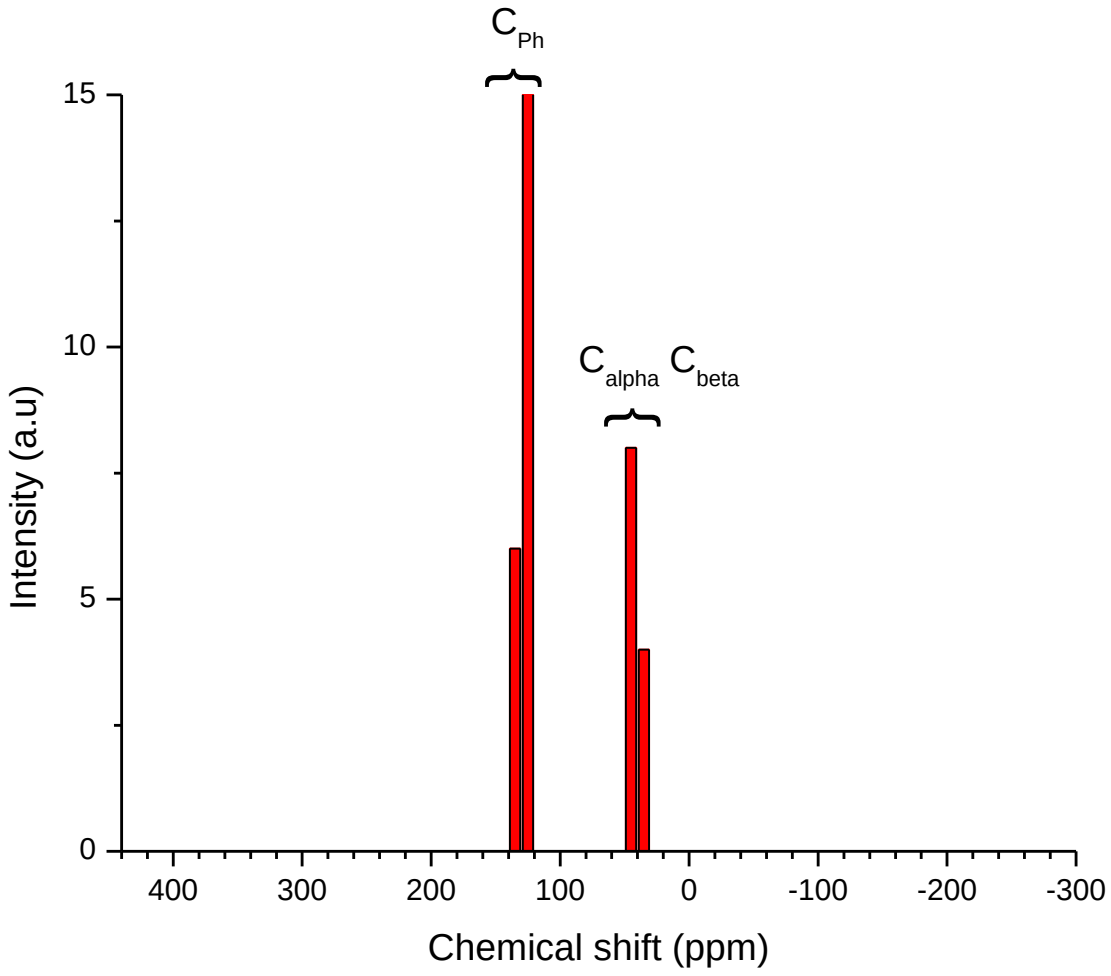

Figure 3.7: ^{13}C probability histogram of outer ligands in $Au_{25}(SCH_2CH_2Ph)_{18}^0$

As stated before, the ^{1}H and ^{13}C paramagnetic shift values show a strong correlation with the spin delocalization and the origin of two ligand populations. The ^{1}H NMR of $\alpha–(CH_2)_{in}$ and $\beta–(CH_2)_{in}$ show a resonance at 23.85 ppm and 3.26 ppm, whereas the outer ligands of $\alpha–(CH_2)_{out}$ and $\beta–(CH_2)_{out}$ show the corresponding resonance at 5.55 ppm and 3.55 ppm, confirming the existence of two ligand families. The average ^{1}H NMR of $\beta–(CH_2)_{in}$ protons experience an upfield shift corresponding to its experimental value suggests the level of theory we used underestimates the paramagnetic shift by 2.14 ppm. Calculated ^{13}C NMR values of inner ligands also suggest it also underestimates the average resonance value.

A different level of theory was also used to check if the underestimation could be rectified. So we used the DFT level of theory with bvp86, a pure functional, and checked the paramagnetic shift values as well as the NMR shift of -1 and +1 charge states as well. The starting geometry of $Au_{25}(SCH_2CH_2Ph)_{18}^{0}$ crystal structure was used as our starting geometry, where the optimized structure of 0 was used as the starting point of -1 and +1 structure optimizations.

The use of bvp86 functional did not improve the resonance value of $\beta–(CH_2)_{in}$, but it also did prove to be adequate for the rest of the ^{1}H and ^{13}C NMR values as shown in Table 3.5 and 3.6. A complete ^{1}H NMR and ^{13}C NMR values for charge states -1,0 and +1 with individual shifts are tabulated in Appendix A. Despite the underestimation of the $\beta–(CH_2)_{in}$ shift, the NMR behavior in $Au_{25}(SCH_2CH_2Ph)_{18}^{+1}$ structure also demonstrated the two ligand populations in the monolayer. The NMR shifts calculated in the +1 showed a closer resemblance towards the $Au_{25}(SCH_2CH_2Ph)_{18}^{1-}$ cluster, suggesting that the +1 charge cluster is a diamagnetic species.

Although we changed the level of functional in calculating the NMR shifts and paramagnetic shift values, we were unable to replicate the experimental value for the $\beta–(CH_2)_{in}$ in the $Au_{25}(SCH_2CH_2Ph)_{18}^{0}$ charge state. However, looking at the values calculated for the

$Au_{25}(SCH_2CH_2Ph)_{18}^0$ clearly demonstrates that the paramagnetic behavior arises due to the Fermi contact term, where the average spin density arising from the unpaired electron is responsible for the change in the nuclear magnetic moment of the nucleus. (Calculated ^1H and ^{13}C NMR values for the -1, 0 and +1 charge states using bvp86 functional are tabulated in Appendix Table A.1-6)

Table 3.5: Calculated ^1H NMR chemical shifts of inner and outer ligands of $Au_{25}[S(CH_2)_2Ph]_{18}^z$ (z= -1,0, +1) [a] (bvp86 / 6-31g**/LANL2DZ)

			α-CH_2	β-CH_2	o-CH	m-CH	p-CH
-1		inner	3.33	3.09	7.43	7.28	7.15
		outer	3.36	3.03	7.44	7.28	7.13
0	δ(300)	inner	20.52	2.48	7.54	7.53	7.14
	δ(300)	outer	4.63	3.00	7.48	7.32	7.21
1		inner	3.12	2.94	7.26	7.45	7.43
		outer	3.24	3.01	7.33	7.34	7.23

[a] The $Au_{25}(SCH_2CH_2Ph)_{18}^0$ was used as the starting structure, where the density fitting was used to optimize all the charge states, using the bvp86/lanl2dz/6-31g level of theory and bvp86/lanl2dz/6-31g** for calculating NMR shifts.

Table 3.6 : Calculated ^{13}C NMR chemical shifts of inner and outer ligands of $Au_{25}[S(CH_2)_2Ph]_{18}^{z}$ (z= -1, 0, +1) [a] (bvp86 / 6-31g**/LANL2DZ)

			α-C	β-C	*i*-C	*o*-C	*m*-C	*p*-C
(-1)	cal	inner	52.63	45.75	136.12	122.54	120.46	118.08
		outer	51.13	43.28	134.99	122.55	120.46	118.55
0	δcal(358)	inner	45.40	101.71	144.49	125.93	121.03	121.03
		outer	48.83	44.48	133.52	123.26	121.07	119.88
(+1)		inner	54.12	45.83	132.93	121.82	121.69	120.45
		outer	53.70	43.43	132.02	121.69	121.69	120.71

[a] The $Au_{25}(SCH_2CH_2Ph)_{18}^{0}$ was used as the starting structure, where the density fitting was used to optimize all the charge states, using bvp86/lanl2dz/6-31g level of theory and bvp86/lanl2dz/6-31g** level of theory for calculating NMR and paramagnetic shifts.

3.4 DFT Calculations to aid ENDOR analysis

Recently, for the first time, Maran and coworkers were able to synthesis the smallest possible ligand in an MPC, ethanethiol. This was the first time an alkane group was used to prepare a monolayer protected gold cluster. This was due to the difficulty and the complexity in the preparation of ligands with higher degree of freedom. The synthesis and crystal structure determination of a simple alkane thiolate protected cluster of $Au_{25}(SEt)_{18}$ for the first time provided us the best way to carryout accurate DFT calculations with the usual approximations of replacing SCH_3CH_2Ph with SCH_3. The new gold cluster was protected by a very short alkanethiolate, and the ligand arrangement in the 0 state was similar to the previous $Au_{25}(SCH_2CH_2Ph)_{18}^0$ cluster.

The paramagnetic $Au_{25}(SEt)_{18}^0$ cluster was used to obtain the first electron nuclear double resonance (ENDOR) results for a monolayer protected cluster. The ENDOR is a powerful method to determine the environment surrounding paramagnetic centers. Experimental and calculation analysis of paramagnetic $Au_{25}(SEt)_{18}^0$ cluster gave an opportunity to study factors governing the asymmetric spin density population of the much larger ligand cluster of $Au_{25}(SCH_2CH_2Ph)_{18}^0$. Due to the nuclear spin of I=3/2, ^{197}Au exhibits hyperfine and quadrupole interactions, which accounts for the fine structural features in the ENDOR spectroscopy. A DFT study of hyperfine and quadrupole tensors gave us the opportunity to study the paramagnetic nature of the neutral $Au_{25}(SEt)_{18}^0$ cluster and its relationship with the structural features.

3.4.1 Hyperfine and Quadrupole Couplings/ Electron Double Resonance Spectroscopy

Electron Double Resonance Spectroscopy, or ENDOR for short is a powerful technique to determine the hyperfine coupling constants that are unresolved in an EPR spectra. ENDOR is especially suited to identify the hyperfine interactions between unpaired electron and the surrounding nuclei. Permanent magnetic dipole of nuclei such as nuclear spins with I=1/2 can interact with an unpaired electron if they are located closely in the space, and give rise to doublet lines in the ENDOR spectrum. For a nuclear spin larger than 1/2, quadrupole interaction affects the ENDOR spectrum and further splits the ENDOR lines. In the case of ^{197}Au, which has a nuclear spin of 3/2 exhibits both quadrupole and hyperfine interactions.

The hyperfine coupling has three different contributions: 1) The isotropic fermi contact term from the finite spin density on the nucleus; 2) The spin-dipole part arising from the magnetic dipole interaction of the magnetic nucleus with the magnetic moment of the electron; and 3) second order contributions that arise from the spin-orbit coupling. The ORCA software [79] utility we used calculates all these contributions.

The alkane thiolate ligand cluster of $Au_{25}(SEt)_{18}^{0}$ showed a very nice ENDOR spectrum, that enabled to determine the hyperfine interactions between the unpaired electron and the gold clusters. In order to study the fine ENDOR spectrum, the structure of $Au_{25}(SEt)_{18}^{0}$ was used as is, without any approximation. Starting from the X-ray structure, the $Au_{25}(SEt)_{18}^{0}$ cluster was optimized using DFT as implemented in Turbomole V.6.3.1 [80]. For the energy minimization step the s-vwn functional and the def2-TZVP basis set for all atoms with a def2-ecp effective core potential for all Au atoms was employed. At the optimized geometry (coordinates can be found in the Appendix A Table A.7), hyperfine constants and quadrupole tensors were calculated using Orca 2.9.1 [79]. These calculations were carried out using unrestricted DFT with the GGA

functional (BP86), the TZVP basis set for Au, and DZP basis set for all other atoms. Scalar relativistic effects were introduced using Zeroth-Order Regular Approximation (ZORA) [81]. All core electrons were included explicitly in the calculation of hyperfine and quadrupole tensors, using segmented all-electron relativistically constructed (SARC) basis set [82]. The Orca-euler utility program was used to calculate the Eular rotation of the hyperfine tensor and the electric field gradient tensor with respect to the g-tensor.

3.4.2 ENDOR analysis using DFT calculations

Experimental analysis of the ENDOR spectrum of $Au_{25}(SEt)_{18}^{0}$ showed five broad lines located at 9.8, 24.7, 42.1, 60.9 and 77.9 MHz [83]. The number of ENDOR lines in the spectrum are related to the equivalent Au nuclei in the cluster. It is intriguing to explain the spectral features, considering the fact that the Au25 cluster has three groups of Au atoms: a central Au, 12 icosahedral Au atoms and 6 staple gold atoms.

DFT has used to compute hyperfine constants, quadrupole tensors and the Orca-euler utility program to calculate Euler rotation of the hyperfine tensor and the electric field gradient tensor with respect to g-tensor. All these quantities in the nuclear–electron interaction Hamiltonian solution was used as a input for the EasySpin software [84], to simulate the ENDOR line shape.

To understand the spectral features of ENDOR spectrum, the DFT calculations were carried out on the optimized $Au_{25}(SEt)_{18}^{0}$ cluster. Table 3.7 shows the calculated hyperfine tensors in the gold cluster, which can be divided into four categories. The icosahedral gold atoms can be divided into two groups according to the calculated hyperfine coupling constants. One group is composed of 8 atoms (labeled as 2, 3, 4 and 5) corresponds to an average of 41 – 55 MHz and the

other group composed of 4 atoms (labeled as 6 and 7) corresponds to an average of 15 – 17 MHz. The staple nuclei have low hyperfine couplings and the fourth group is the central gold atom.

The calculated hyperfine coupling constants are responsible for a single configuration, whereas in the ENDOR spectrum the hyperfine and quadrupole tensors of these atoms dynamically averaged by the vibrational motion. To simulate the ENDOR response, for each group of similar core nuclei the average of Cartesian component of the hyperfine and the quadrupole tensors with their Euler angles are used (quadrupole and Euler angles are tabulated in the Appendix Table A.8). According to the simulated ENDOR spectrum by Alfonzo Venzo [83], the five peaks are mainly due to the different Au groups in the gold cluster. Peaks 24.7 and 42.1 MHz are mainly due to the group of 8 core Au atoms, where the other group corresponds to the peak at 9.8 MHz. The central Au atom is responsible for the peak at 77.9 MHz. The peak at 60.9 MHz is due to group of 8 core gold atoms and central Au atom. The peak at 9.8 MHz is due to the staple gold atoms. The DFT calculation to obtain hyperfine coupling constants and quadrupole tensors were carried out using two model structures. The actual crystal structure of $Au_{25}(SEt)_{18}^{0}$ MPC was used as the starting point in one of the models and in the other model the SEt groups were replaced by SMe. This last calculations allowed us to test whether using a small ligand to predict the experimental spectrum is adequate. Often it has been assumed that calculations using smaller ligand groups such as SH and SMe as opposed the actual (larger) ligands will not change the outcome of the solution. But in our simulation of the ENDOR spectrum using $Au_{25}(SMe)_{18}^{0}$ model structure did not match sufficiently well with the experimental spectrum (figure 3.8). This suggests that calculations with the actual ligands must be considered.

Table 3.7. DFT-Computed Values of the Anisotropic Hyperfine Tensors for $Au_{25}(SEt)_{18}^{0}$.

Atom label[a]	Ax (MHz)	Ay (MHz)	Az (MHz)	Ave[b] (MHz)
Au1(central)	20.7	14.2	11.6	15.5
Au4(ico)	40.3	44.5	36.7	40.5
Au3(ico)	52.8	45.1	48.5	48.8
Au7(ico)	9.1	22.7	12.6	14.8
Au2(ico)	39.5	40.8	47.6	42.6
Au5(ico)	50.8	61.6	52.7	55.0
Au6(ico)	11.4	14.3	23.9	16.5
Au8(staple)	1.9	1.9	3.1	2.3
Au11(staple)	20.0	18.6	18.9	19.2
Au9(staple)	4.0	2.9	2.8	3.2
Au10(staple)	3.7	5.0	4.3	4.3
Au12(staple)	21.0	18.3	19.4	19.6
Au13(staple)	10.3	11.1	9.8	10.4

[a] Except for the central atom, Au1, for symmetry reasons all other labels pertain to couples of equivalent Au atoms [b] Average of Ax, Ay, and Az.

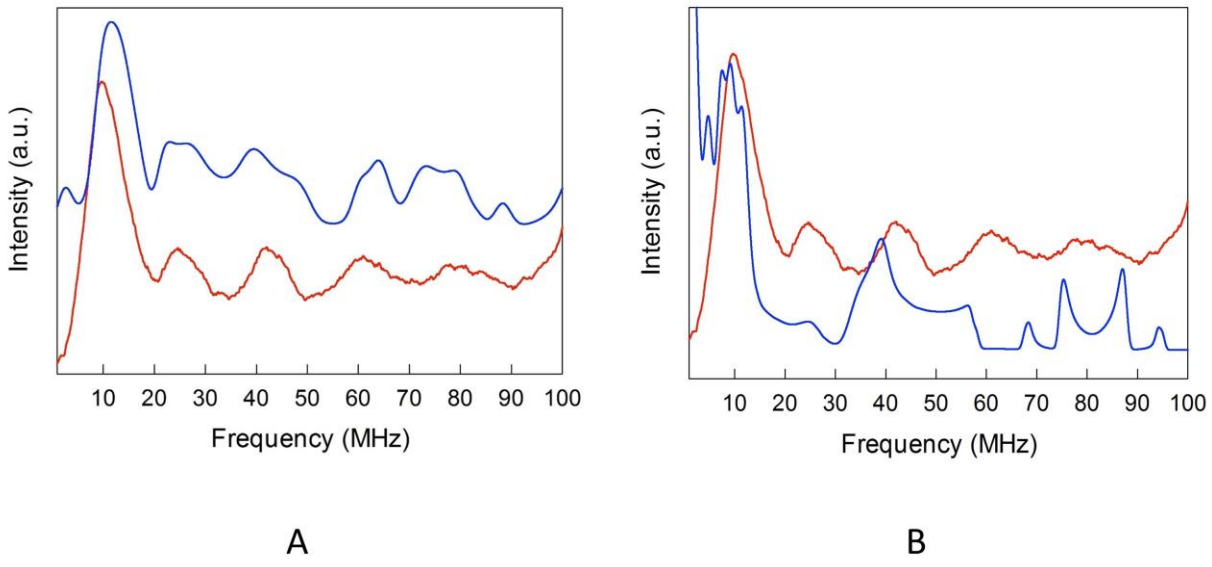

Figure 3.8: A) ENDOR spectrum of $Au_{25}(SEt)_{18}^{0}$ in toluene at 5.5 K (red line). The blue line shows the corresponding simulation based on the hyperfine and quadrupole components obtained by DFT calculation. B) ENDOR spectrum of $Au_{25}(SEt)_{18}^{0}$ in toluene at 5.5 K (red line). The blue line shows the corresponding simulation for $Au_{25}(SMe)_{18}^{0}$

3.5 Conclusions

The carefully controlled redox coupled charge states (-1, 0, +1) produced by oxidation coupling reactions were characterized using ^{1}H and ^{13}C NMR spectroscopy. DFT calculations were used to analyze and also classify the peak assignments in $Au_{25}(SCH_2CH_2Ph)_{18}^{0}$ which could not be done using the experimental evidence. In $Au_{25}(SCH_2CH_2Ph)_{18}^{0}$, a unique NMR behavior was observed due to the unpaired electron present, and it also was able to confirm the presence of two ligand populations in the monolayer of the cluster. The inner ligand populations were composed of 12 inner ligands and the outer ligand population composed of 6 outer ligands. From the two populations, we found out the inner ligand population is more prone towards the effect of the unpaired electron, and this effect is more pronounced in the $\alpha–(CH_2)_{in}$ methylene protons where a sizeable shift of ~23 ppm is observed. The effect of unpaired electron is felt by $\beta–(CH_2)_{in}$ as well as in the outer $\alpha–(CH_2)_{out}$ methylene protons, but the $\beta–(CH_2)_{out}$ methylene protons of the outer ligands are not affected by the paramagnetic field. This dramatic paramagnetic effect is also evident in the ^{13}C NMR spectrum, where the average shift in $\alpha–C_{in}$ and $\beta–C_{in}$ show distinct peak positions.

The DFT calculations carried out allowed us to visualize the spin density delocalization across the $Au_{25}(SCH_2CH_2Ph)_{18}^{0}$ cluster, and the Fermi contact term arising due to the interaction between nuclear magnetic moment and average spin density is responsible for this unique behavior in the α protons of the inner ligands. The total average spin density arises from the difference between two spin density populations (alpha and beta). In particular, the beta spin density is responsible for the negative shift values uncounted in the $\alpha–C_{in}$, whereas the excess alpha spin density is responsible for the large downfield shift in the carbon nucleus. This alpha spin density resides closer to the gold core and does not extend beyond the $\alpha–C_{in}$. The current level theory used

was not adequate to simulate the excess of alpha spin density throughout the α–C_{in} and was the main reason why only a few ^{13}C nucleus showed the desired negative paramagnetic shift. From the two functionals we used to calculate the PNMR shift values, B3LYP performed better than the bvp86, which confirmed earlier claims [85]. Despite the use of two different Density functionals to calculate the paramagnetic NMR behavior, in the $Au_{25}(SCH_2CH_2Ph)_{18}^0$ cluster the calculated value of β–$(CH_2)_{in}$, underestimated the experimental value. It would be interesting to calculate the pseudo contact shift for the $Au_{25}(SCH_2CH_2Ph)_{18}^0$ cluster and see how it would affect the overall NMR shift in the paramagnetic species. With alpha spin density residing near the β–$(CH_2)_{in}$ methylene proton which is responsible for the high shielding in the α–$(CH_2)_{in}$ the pseudo contact shift might be the missing component which would move the methylene protons in β–$(CH_2)_{in}$ towards the much anticipated downfield movement.

The NMR results of the $Au_{25}(SCH_2CH_2Ph)_{18}^{-1}$ and $Au_{25}(SCH_2CH_2Ph)_{18}^{+1}$ clusters also point out the existence of two ligand populations, where the $Au_{25}(SCH_2CH_2Ph)_{18}^{+1}$ charge state, showing similar NMR shifts than in the case of the $Au_{25}(SCH_2CH_2Ph)_{18}^{-1}$ cluster, pointed out that the cluster is diamagnetic in nature. For the first time, with the NMR calculations, we were able to characterize the $Au_{25}(SCH_2CH_2Ph)_{18}$ as a function of different charge states.

The paramagnetic nature of the zero charged cluster can be further studied using the small alkane thiolate ligand stabilized $Au_{25}(SEt)_{18}$ cluster. Careful inspection of the experimental ENDOR spectrum with the DFT based calculation of the hyperfine and quadrupole tensors allowed us to distinguish the different nuclei responsible for the spectrum. According to the ENDOR spectrum the Au atoms can be divided in to four groups namely: central Au atom, 12 staple Au atoms, and two groups of icosahedral gold atoms. Spin density contribution arising from the

unpaired electron in the paramagnetic cluster made it sensitive to the ENDOR spectroscopy which was able to identify the environment around the nuclei.

Chapter 4

Effect of spin state in the electronic structure of $Au_{25}[SCH_3]_{18}^{z}$

Selected portions of the material presented in this chapter were published in:

Antonello, S.; **Perera, N. V.**; Ruzzi, M.; Gascón, J. A.; Maran, F. Interplay of Charge State, Lability, and Magnetism in the Molecule-like $Au_{25}(SR)_{18}$ Cluster. *Journal of American Chemical Society.* **2013**, *135*, 15585–15594.

Chapter 4: Effect of spin state in the electronic structure of $Au_{25}[SCH_3]_{18}^{z}$ (z = -1, 0, +1)

4.1 Introduction

The ligand protected $Au_{25}(SCH_2CH_2Ph)_{18}$ cluster is the most studied gold cluster among small nanoclusters with molecular like behavior. One of the interesting features that arise in such small cluster size is the molecular like HOMO – LUMO energy gap. During the electron transfer process the charge of these clusters can be changed, which changes the HOMO – LUMO gap energy as well. A fundamental level study on the optical absorption spectra will give information on the electronic structure, and how well we can address the superatom terminology towards the smaller nanoparticles.

4.1.1 Superatomic orbitals in monolayer protected clusters

The thermodynamic stability of discrete sizes of metal clusters including gold clusters was well documented. But the factors underlining the stability were not known. A unified view into the factors governing the principles of stability in these type of clusters were tried to address using the noble gas superatomic terminology.

In Mendeleev's periodic table, the elements are arranged according to the similarities in properties. When arranged according to their properties, they fall into horizontal rows with similar chemical properties, which later could be explained by the filling with electrons using the aufbau principle. The right-most column is composed of noble gases, which are chemically inert. The noble gases are composed of closed electronic shells and the electronic composition of all other atoms can be expressed in terms of the maximum valence. In metal atoms, the valance electrons, can be transformed to other atoms and ligands in achieving the noble electronic configuration.

Similarly, the super atom theory helps to predict the stability of noble metal nanoparticles. The theory was developed using the Jellium model to address the factors affecting cluster stability. This model, developed for gaseous cluster species, was able to explain the stability of specific cluster sizes usually known as the magic numbers, with the filing of electronic shells.

The Jellium model was developed by Knight et al, in 1984, using Sodium clusters [86]. It approximates the *s* electrons moving uniformly in a positively charged spherical potential. Spherical symmetry in these clusters cause fermions to arrange in sub shells with specific quantum numbers and to exhibit angular momentum character [10]. The model predicted a series of magic numbers, with specific valance electron counts, and corresponds to a successive electronic shell closing. Apart from the small Sodium clusters, Aluminum [87], Gallium[88] were used to experimentally determine stable atomic cluster compositions. Using the homogenous spherical Jellium model, the experimentally observed magic numbered clusters of 8, 18, 20, 34, 40, 58 and 92 were predicted. Still, not all magic numbers could be reproduced by this model, and the inhomogeneous spherical Jellium model was able to correct it [89].

The superatom model developed using the Jellium model, gives rise to stable electron counts. However, not every closed subshell corresponds to a magic number.

$$n = 2, 8, 18, 34, 58, 92, 138, ..$$

where *n* is the stable electron count. The stable electron counts with the aufbau rule of delocalization will give superatomic orbitals, with successive shell closings, where S – P – D – F – G – H denotes the angular momentum character

$$1S^2 \mid 1P^6 \mid 1D^{10} \mid 1S^2\, 1F^{14} \mid 2P^6\, 1G^{18} \mid 2D^{10}\, 3S^2\, 1H^{22} \mid ..$$

In medium to small gold clusters, the loosely bound 6s atomic electrons contribute towards the spherical electron cloud, giving rise to superatom orbitals. The clusters are then stabilized by the ligands as it surrounds the naked clusters. The stabilizing ligands either can be electron withdrawing (X_M) or weak Lewis based ligand (L_S). Now the shell closing electron count for the superatomic cluster of $[L_S \, . \, A_N \, X_M]^z$ can be written as:

$$n = N_A - M - z$$

Using the above equation the shell closing electron count (n) can be calculated. Where N is the number of valance *s* orbitals contributing by the metal atom A, while M and S related to the cluster stoichiometry and z is the overall charge of the complex. According to the above equation, the shell closing number of gold clusters can be calculated.

Eg : $[Au_{25}(SCH_2CH_2Ph)_{18}]^-$ $n = 25 - 18 - (-1) = 8$

$[Au_{102}(p - MBA)_{44}]$ $n = 102 - 44 - (0) = 58$

Shell closing numbers have given a way to identify the stable compounds of metal clusters and to relate the stability to its properties.

4.1.2 Molecule like HOMO – LUMO gap in $Au_{25}L_{18}$ clusters

Nanoparticles show size-dependent properties, importantly in the nanometer size scale. In particular, as the core size decreases the HOMO-LUMO energy gap increases, manifesting the quantum confinement effect [69].

In the family of thiolate ligand protected gold nanoparticles, the metal to molecule-like transition is signaled by the emergence of an energy gap. This energy gap can be detected optically or electrochemically or by both methods. The optical energy gap can be detected for nanoparticles in the range of 1 nm or smaller. This gap is experimentally determined by the electronic band edge or the absorbance spectrum onset. This can be observed in the near-infrared region with energies

near or above 1 eV. The electrochemical energy gap is the electrochemical potential difference between the first oxidation and the first reduction wave. Unlike optical energy gaps, electrochemical methods can be measured for lower energies and are useful for determining smaller HOMO–LUMO gaps. However, both methods exhibit uncertainties in determining the energy gap; in optical absorption, it is associated with measuring the excitation energy and in electrochemical measurements, it is associated with estimating the charging energy correction [90–92].

According to the electrochemical behavior, monolayer protected gold clusters can be divided in three main categories as shown in the Figure 4.1. The three regions are: the metal like bulk nanoparticles showing no energy gap, the nanoparticles showing quantized double layer charging for Au_{225} to Au_{140} [93], and the nanoparticles showing molecular like energy gaps for smaller nanocluster of Au_{75} and smaller particle sizes. This HOMO–LUMO gap in smaller nanoparticles increases rapidly with the decreasing core sizes. For example, when the particle size decreases from Au_{75} to Au_{25} the energy gap increases from 0.47 eV to 1.3 eV.

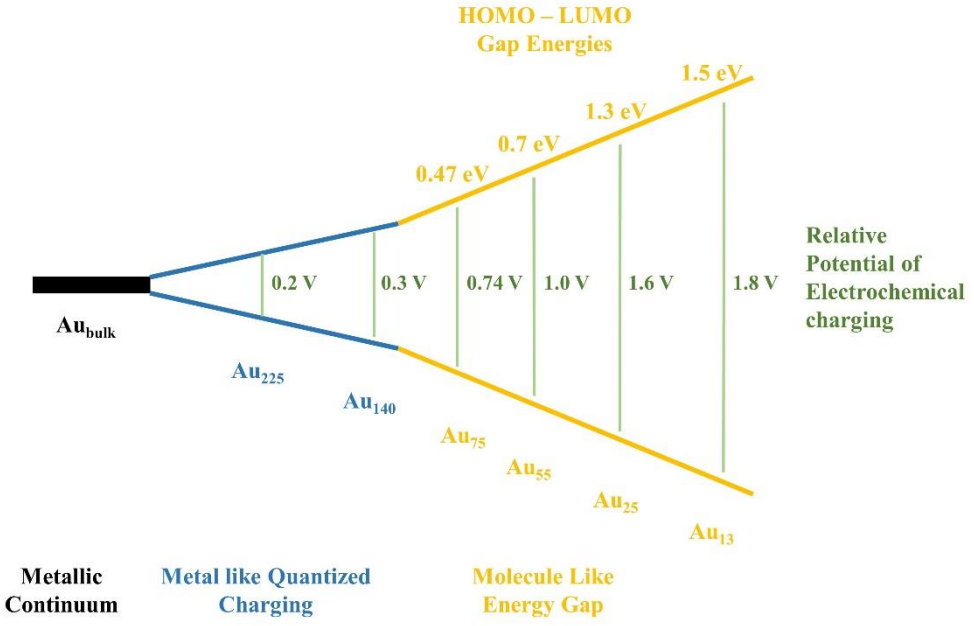

Figure 4.1: Change in HOMO – LUMO gap with decreasing core size. According to the electrochemical behavior, monolayer protected gold clusters can be divided in the three main categories Metallic continuum, Metal like quantized charging and molecular like energy gap region.

This rapid increment in the HOMO–LUMO gap correlated with discrete spectral features in the absorption line shape. The first ever determined crystal structure of Au_{140} with a core size of 1.6 nm did not show any HOMO – LUMO gap and it only showed a single peak which is due to the plasmon resonance. The later discovered Au_{25} with a core size of 1.1 nm had larger HOMO–LUMO gap around 1.3 eV and it showed discrete spectral features in the ultra-violet (UV) spectrum. The discrete spectral features were thought to originate from the molecular like HOMO – LUMO gap energies.

DFT calculations on small model gold cluster of $Au_{25}SH_{18}$ showed the HOMO is triply degenerate and the LUMO is doubly degenerate, [30] [94] which gave the insight into the superatom like orbitals. A later study on symmetrically optimized $Au_{25}SPh_{18}$ pointed to the triply degenerate HOMO level being slightly uneven [95] as one of the HOMO orbital energies has a higher energy than the rest.

In our previous study in chapter 3, we encountered the $Au_{25}(SCH_2CH_2Ph)_{18}^0$ cluster as a paramagnetic in nature. The oxidation of the HOMO (nearly degenerate) to the $Au_{25}(SCH_2CH_2Ph)_{18}^{1+}$ should generate another paramagnetic species, assuming the ejection of the electron should originate from an already doubly occupied molecular orbital. In fact, in our studies we found out the $Au_{25}(SCH_3)_{18}^{1+}$ generated by the oxidation of the neutral $Au_{25}(SCH_3)_{18}^0$ is diamagnetic. The experimental and the DFT study of the NMR spectra also showed the $Au_{25}(SCH_3)_{18}^{1+}$ cluster closely resembles the negatively charged diamagnetic $Au_{25}(SCH_3)_{18}^{1-}$ species.

4.2 Construction of the model structure and the computational methods

In order to evaluate the optical spectrum of different charge states and its electronic structure we needed a model structure. A structure which is computationally feasible. As a template, the crystal structure of $Au_{25}(SCH_2CH_2Ph)_{18}^{1-}$ was selected. The ligands were changed from $–SCH_2CH_2Ph$ to –SH. The –H as ligand is (a too simplified structure) used for its computational simplicity. Then the ligand groups were rotated and arranged to achieve S6 symmetry as shown in the Figure 4.2. Once the cluster was arranged in the S6 symmetry, the ligands were changed from SH to SCH_3 to represent a more realistic situation. With methyl

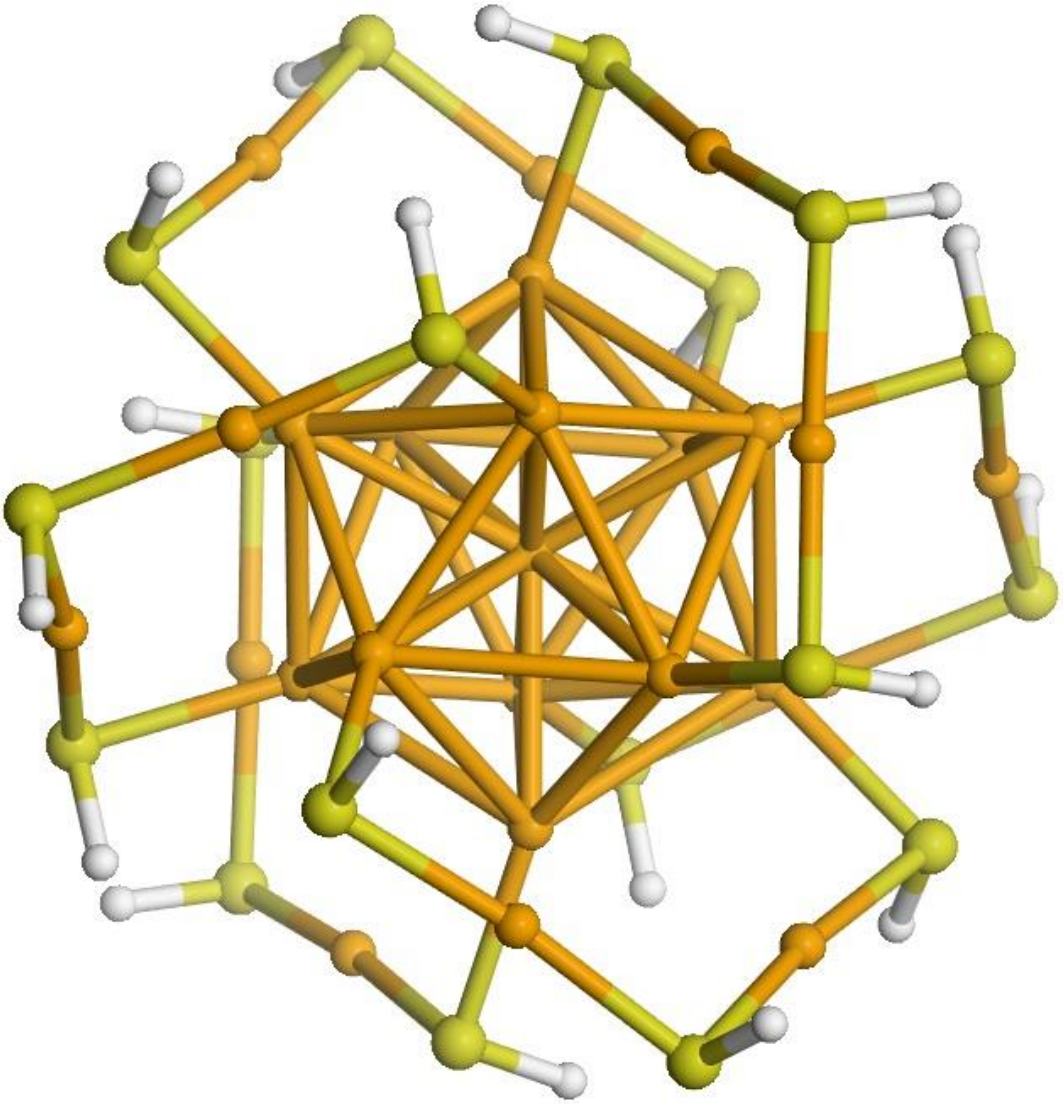

Figure 4.2: S6 symmetric structure of $Au_{25}(SH)_{18}$. Constructed using the crystal structure of $Au_{25}(SCH_2CH_2Ph)_{18}^0$ and the ligand groups were rotated to achieve the S6 symmetry.

rotations, sustaining the S6 symmetry was not possible, and the structure was relaxed to having Ci symmetry.

All structure optimizations and single point calculations were carried out using resolution of identity density functional theory (RI-DFT) employed in Turbomole V.6.3.1 [80] package along with local density approximation (LDA) correlation functional of S-VWN by Vosko, Wilk and Nusair. A triple-ξ valance quality plus polarization of def2-TZVP basis set and a default auxiliary basis set of def2-TZVP was used for S, C and H atoms, whereas for Au, 60 electron relativistic effective core potential (ECP) of def2–ECP basis set was used. Time dependent DFT with RI approximation [96] was carried out to calculate the optical absorption spectra for all charged states after optimization.

4.3 Computational Results and Discussion

4.3.1 HOMO – LUMO gap

The electronic structure of $Au_{25}(SCH_3)_{18}^{1-}$ is characterized by a closed shell electron configuration, where according to the superatom terminology, $Au_{25}(SCH_3)_{18}^{1-}$ has a stable electron configuration ($1S^2\ 1P^6$), with a shell closing electron count of 8. In this case the HOMO level has a P angular momentum character, with a fully occupied 1au states, while the first unoccupied orbital corresponds to a a_g state (according to the figure 4.3 and the density of states diagram in figure 4.4). According to the orbital energy diagram in figure 4.3, the triply degeneracy [29] of HOMO in the -1 state is no longer applicable, and this finding is an agreement with analysis by Aikens's, frontier molecular orbitals [95].

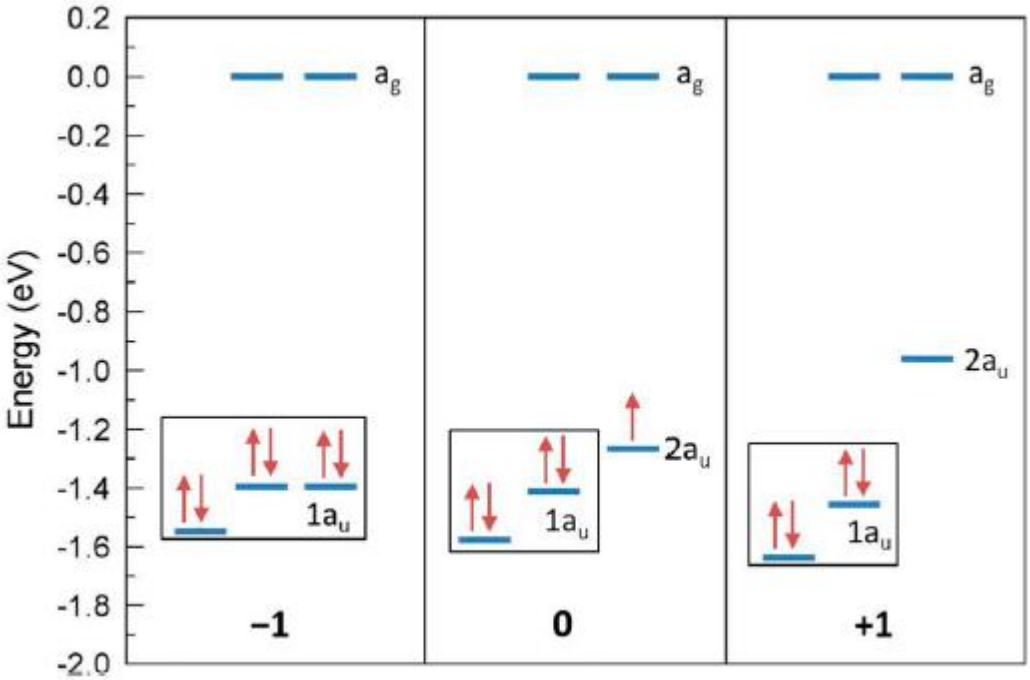

Figure 4.3: Orbital energy diagrams of $Au_{25}(SCH_3)_{18}^{z}$ (z= -1, 0, +1). The Energy manifold is represented in a box.

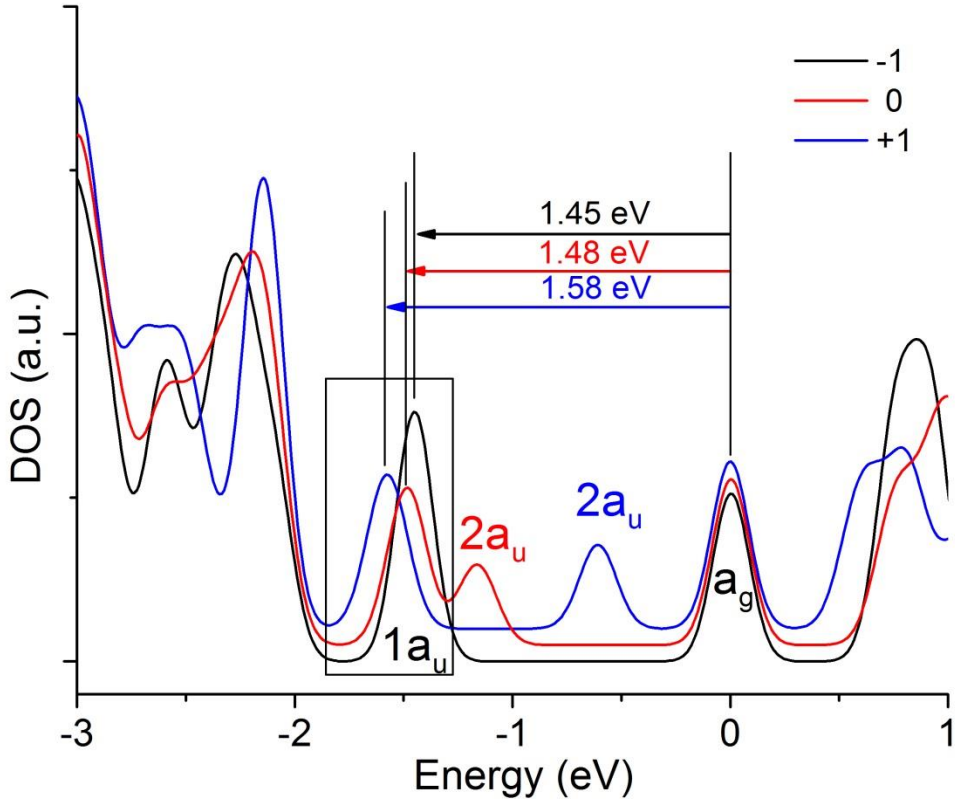

Figure 4.4: Density of states (DOS) diagram of $Au_{25}(SCH_3)_{18}^{z}$ (z= -1, 0, +1). While the $Au_{25}(SCH_2CH_2Ph)_{18}^{1-}$ is represented in black, $Au_{25}(SCH_2CH_2Ph)_{18}^{0}$ is represented in red and $Au_{25}(SCH_2CH_2Ph)_{18}^{1+}$ is represented in blue color. The calculated values are in a good agreement with the corresponding experimental values of 1.33, 1.46 and 1.53 eV.

Although the energy levels in the HOMO are not equal, they can be considered into a single manifold. Adding a 0.1 eV Lorentzian energy width to the density of states (DOS), the three HOMO energy levels can be considered as part of the same manifold. Therefore the three energy levels hereafter will be called as $1a_u$, while the lowest two unoccupied energy levels will be called as a_g. In the -1 state, the energy separation between the $1a_u$ and 1ag is 1.45 eV, in very good agreement with the experimentally measured value of 1.33 eV [97].

Once the cluster is oxidized from -1 to 0, the $1a_u$ manifold splits and gives rise to a second distinct Lorentzian peak in the DOS as seen in figure (4.4). As the new peak in the DOS diagram has risen from the 1au, we now call the second peak as $2a_u$. Now, the energy gap between the occupied $1a_u$ and a_g increased by 0.03 eV. While the calculated increment is quantitatively smaller than the experimental value of 0.13 eV, the direction of increment is in qualitative agreement with the experimentally measured HOMO – LUMO gap increase.

A more complex situation arises for the 0 to +1 oxidation, in which a triplet state is possible. In the next step of redox oxidation, where the cluster oxidizes from 0 to +1, the electron is being ejected from the singly occupied $2a_u$ level, making the $2a_u$ level vacant, and making the +1 state a singlet. The $2a_u$ level being vacant, in the DOS diagram, the peak further move to a higher energy. If the resulting state is a triplet state, then to promote an electron from the $1a_u$ to $2a_u$ energy level would require a large energy, which would rule out the paramagnetic +1 state. In fact, the resulting triplet state of $[Au_{25}(SCH_3)_{18}]^+$ consist of 0.36 eV energy higher than the optimized single state. Although the 0 state is a paramagnetic state the oxidation of the paramagnetic state has produced a stable singlet species. These results further confirms our findings with the NMR results [98] in the Chapter 3. While the 2au energy level being vacant and occupying a higher energy level, the transition of $1a_u \rightarrow 2a_u$ is symmetry forbidden. Thus, despite $2a_u$ energy level is vacant, the a_g level

appears to behave as the LUMO, and the 1au as the HOMO. The calculated energy gap of 1.58 eV corresponds to the transition between 1au and a_g level. This increment of 0.13 eV is again a good agreement with the experimentally observed increment of 0.20 eV. The severe splitting in the HOMO manifold in the +1 species does agree with the NMR results, and it questions the superatom model representation for such di-radical species.

4.3.2 Optical absorption spectra

Spectral features in the optical absorption spectra can be correlated with distinct electronic structures in the different charge states of $Au_{25}(SCH_3)_{18}$ cluster. The optical absorption spectra of the -1, 0 and +1 charge states could be reproduced using time dependent density functional theory calculations (TDDFT). As the optical absorption spectra is known to show a strong dependence on the temperature [92], we note that all our calculations are done at 0 Kelvin.

Reproducing the optical absorption spectra and deducing the energy levels responsible for the excitations of -1 state have been attempted in the past [99] [29], and tentative assignments have been made with respect to the experimental results. Until now, however, no study had addressed the double peak observed in the experimentally UV spectra. In the calculated optical absorption spectra, using the half width maximum of 0.1 eV for the Lorentzian, the double peak structure was reproduced successfully for the -1 state as shown in figure 4.5. The peaks in the experimentally observed spectra is less resolved at 298K [100] [78], but Devadas et al [92] have shown these peaks are completely resolved at 78 K, where the two peaks are located at 1.67 eV and 1.9 eV, with the second peak 1.5 times higher than the first. In the calculated spectra of -1, the two peaks are located at 1.47 eV and 1.67 eV, with the second peak 1.2 times higher than the first. The

transitions involved in the double peak originate from the HOMO → LUMO, and HOMO – 1→ LUMO orbitals.

As in the -1 state, the TDDFT spectra of 0 and +1 charge states also happens to show a double peak structure, where in the 0 charge state the two peaks are located at 1.49 eV and 1.65 eV. The +1 charge state it is located at 1.53 eV and 1.72 eV. These findings are consistent with the experimentally observed double peak for the Au25 gold clusters.

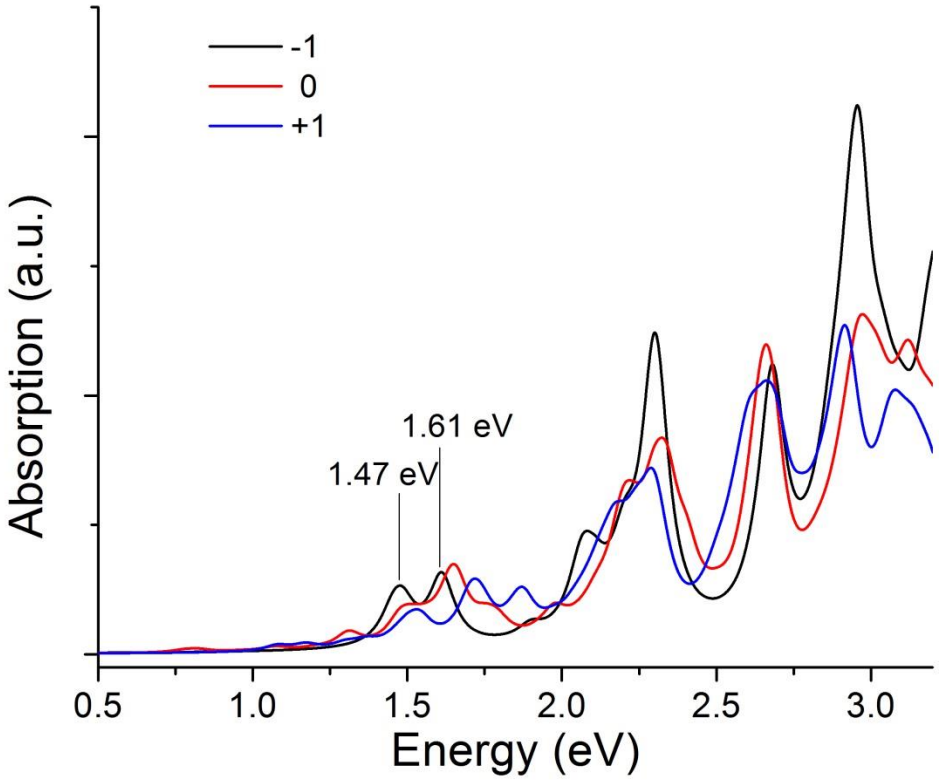

Figure 4.5: Calculated TDDFT absorption spectra for $Au_{25}(SCH_3)_{18}^{z}$ (z= -1, 0, +1). Spectra were constructed with 0.1 eV width Lorentzians. Black line corresponds to the $Au_{25}(SCH_3)_{18}^{1-}$, Red line corresponds to the $Au_{25}(SCH_3)_{18}^{0}$, Blue line corresponds to the $Au_{25}(SCH_3)_{18}^{1+}$.

4.4 Conclusions

All previous studies have assumed gold nanoclusters to have their electronic structure described in terms of superatomic orbitals. This has resulted from assuming the HOMO level as triply generate. With this picture, researches tend to assume that removal of two electron should lead to a paramagnetic state. However, our DFT calculations show that the HOMO energy manifold splits in the 0 state, and that that energy separation becomes quite large in the +1 state. That means that the singlet state becomes much more stable than the presumed triple state. Therefore, the superatom analogy is not that useful for oxidized species. All these results are consistent with ^{13}C and ^{1}H NMR eperiments, which have indicated that the +1 species is diamagnetic [101]. On the other hand, a recent EPR study [102] has pointed the +1 cluster to be radical in nature. We claim this last experimental result is incorrect.

Appendix A

Table A.1: Calculated [a] and experimental ^{1}H NMR chemical shifts of inner and outer ligands of $Au_{25}[S(CH_2)_2Ph]_{18}^{1-}$ (bvp86 / 6-31g**/LANL2DZ)

inner	α-CH_2	β-CH_2	o-CH	m-CH	p-CH
1	2.77	2.40	6.79	7.18	7.09
2	3.65	3.84	7.87	7.49	7.27
3	3.26	2.60	7.45	7.30	7.23
4	3.11	2.59	7.36	7.16	6.98
5	2.92	2.77	7.29	6.98	6.86
6	3.60	3.46	7.79	7.58	7.39
7	3.60	3.26	7.61	7.33	7.23
8	3.40	2.66	6.74	6.96	6.87
9	3.12	3.22	7.38	7.25	7.09
10	4.11	2.69	7.18	7.13	7.10
11	3.46	3.22	7.64	7.60	7.43
12	2.99	4.38	8.02	7.42	7.23
avg	3.33	3.09	7.43	7.28	7.15
exp(298)	3.80[d]	3.13	7.19	7.15	7.08
outer	α-CH_2	β-CH_2	o-CH	m-CH	p-CH
13	3.67	2.89	7.58	7.40	7.14
14	3.92	3.20	7.68	7.42	7.16
15	4.20	3.21	7.50	7.26	7.19
16	2.28	2.32	6.98	6.93	6.89
17	3.24	3.24	7.53	7.41	7.31
18	2.86	3.28	7.41	7.23	7.11
avg	3.36	3.03	7.44	7.28	7.13
exp(298)	3.13	2.93	7.14	7.19	7.15

[a] The $Au_{25}[S(CH_2)_2Ph]_{18}^{0}$ was used as the starting structure, where the density fitting was used to optimize all the charge states, using bvp86/lanl2dz/6-31g level of theory and bvp86/lanl2dz/6-31g** level of theory for calculating NMR and paramagnetic shifts.

Table A.2: Calculated and experimental ^{13}C NMR chemical shifts of inner and outer ligands of $Au_{25}[S(CH_2)_2Ph]_{18}^{1-}$ (z= -1,0, +1) [a] (bvp86 / 6-31g**/LANL2DZ)

inner	α-C	β-C	*i*-C	*o*-C	*m*-C	*p*-C
1	50.64	45.41	134.84	121.86	120.91	118.18
2	56.60	45.35	136.52	123.13	120.39	118.41
3	52.55	43.26	135.38	122.54	120.62	118.60
4	52.14	45.12	136.02	122.70	120.10	118.32
5	53.32	50.06	136.97	122.43	120.41	118.05
6	51.12	45.60	136.19	122.46	120.77	118.23
7	53.09	44.24	135.64	123.21	120.07	117.77
8	51.75	44.53	136.38	121.34	120.49	117.68
9	51.42	45.54	136.29	122.10	120.53	117.62
10	52.89	43.06	134.91	122.64	119.93	117.96
11	49.29	44.48	136.31	122.22	120.83	118.84
12	56.79	52.32	137.95	123.79	120.47	117.30
avg	52.63	45.75	136.12	122.54	120.46	118.08
exp(298)	n.d	n.d	141.88	129.85	128.52	126.27

outer	α-C	β-C	*i*-C	*o*-C	*m*-C	*p*-C
13	50.14	41.39	133.03	123.19	120.50	119.26
14	51.47	42.23	134.25	122.69	120.44	120.00
15	53.56	42.92	136.13	122.62	120.59	117.87
16	50.77	42.92	135.03	122.13	119.98	117.76
17	51.96	44.84	135.87	122.33	120.83	118.12
18	48.89	45.41	135.64	122.34	120.41	118.26
avg	51.13	43.28	134.99	122.55	120.46	118.55
exp(298)	35.98	42.18	140.88	129.3	128.63	126.49

[a] The $Au_{25}[S(CH_2)_2Ph]_{18}^{0}$ was used as the starting structure, where the density fitting was used to optimize all the charge states, using bvp86/lanl2dz/6-31g level of theory and bvp86/lanl2dz/6-31g** level of theory for calculating NMR and paramagnetic shifts.

Table A.3: Calculated [a] and experimental ^{1}H NMR chemical shifts of inner and outer ligands of $Au_{25}[S(CH_2)_2Ph]_{18}^{0}$ (bvp86 / 6-31g**/LANL2DZ)

inner	α-CH_2	β-CH_2	o-CH	m-CH	p-CH
1	16.36	-0.26	6.50	7.93	6.32
2	3.18	3.59	7.90	7.63	7.39
3	5.87	2.48	7.39	7.38	7.32
4	25.01	2.44	7.98	7.33	6.89
5	64.15	3.07	7.58	7.04	7.25
6	7.45	2.88	7.73	7.72	7.40
7	3.15	3.05	7.54	7.46	7.36
8	17.35	0.05	6.64	7.85	6.21
9	25.19	3.05	8.02	7.49	7.18
10	6.91	2.62	7.29	7.32	7.30
11	7.58	2.81	7.75	7.84	7.52
12	64.05	4.04	8.21	7.40	7.53
avg(300)	20.52	2.48	7.54	7.53	7.14
exp(298)	24.9[d]	5.4[c]	7.42[c]	t 7.19	n.d
exp(358)	21.22[d]	4.9[c]	7.41	7.18	6.99

outer	α-CH_2	β-CH_2	o-CH	m-CH	p-CH
13	4.66	3.23	7.52	7.32	6.96
14	5.93	3.47	7.60	7.44	7.30
15	5.30	2.81	7.45	7.32	7.33
16	4.00	2.04	7.07	7.10	7.07
17	4.08	3.28	7.71	7.48	7.43
18	3.77	3.16	7.53	7.24	7.19
avg(300)	4.63	3.00	7.48	7.32	7.21
exp(298)	5.13	t 2.81	n.d	n.d	n.d
exp(358)	t 5.05	t 2.89	7.02	7.09	7.03

[a] The $Au_{25}[S(CH_2)_2Ph]_{18}^{0}$ was used as the starting structure, where the density fitting was used to optimize all the charge states, using bvp86/lanl2dz/6-31g level of theory and bvp86/lanl2dz/6-31g** level of theory for calculating NMR and paramagnetic shifts.

Table A.4: Calculated and experimental ^{13}C NMR chemical shifts of inner and outer ligands of $Au_{25}[S(CH_2)_2Ph]_{18}^0$ (z= -1,0, +1) [a] (bvp86 / 6-31g**/LANL2DZ)

inner	α-C	β-C	*i*-C	*o*-C	*m*-C	*p*-C
1	91.75	190.67	175.29	127.54	119.81	126.20
2	54.21	40.49	134.88	123.03	121.04	119.82
3	48.13	38.96	133.79	122.07	121.29	119.81
4	-41.74	163.74	158.24	136.77	121.55	122.12
5	69.75	111.85	125.79	123.18	121.42	118.70
6	52.24	64.45	137.69	123.17	121.20	120.10
7	50.88	39.64	133.78	123.14	120.47	119.20
8	92.27	189.84	177.02	126.93	119.65	125.86
9	-41.93	162.61	158.76	135.92	122.01	122.59
10	47.64	39.22	133.04	122.53	120.67	119.06
11	51.17	63.97	138.02	122.82	121.42	120.59
12	70.46	115.08	127.54	124.12	121.78	118.25
avg(358)	45.40	101.71	144.49	125.93	121.03	121.03
δexp(358)	-134.00[c]	350.00[c]	144.22	131.73	128.63	126.53

outer	α-C	β-C	*i*-C	*o*-C	*m*-C	*p*-C
13	48.95	41.43	132.81	123.90	120.61	120.49
14	52.35	42.70	133.37	123.27	120.96	121.30
15	51.30	44.48	134.33	121.82	121.32	119.36
16	49.16	44.53	133.38	122.07	120.83	118.59
17	46.48	46.37	133.88	124.14	121.55	119.90
18	44.76	47.37	133.36	124.37	121.13	119.64
avg	48.83	44.48	133.52	123.26	121.07	119.88
δexp(358)	39	47.71	140.05	129.57	128.16	126.41

[a] The $Au_{25}[S(CH_2)_2Ph]_{18}^0$ was used as the starting structure, where the density fitting was used to optimize all the charge states, using bvp86/lanl2dz/6-31g level of theory and bvp86/lanl2dz/6-31g** level of theory for calculating NMR and paramagnetic shifts.

Table A.5: Calculated [a] and experimental ^{1}H NMR chemical shifts of inner and outer ligands of $Au_{25}[S(CH_2)_2Ph]_{18}^{+1}$ (bvp86 / 6-31g**/LANL2DZ)

inner	α-CH_2	β-CH_2	o-CH	m-CH	p-CH
1	2.09	2.16	6.52	7.18	7.28
2	3.18	3.60	7.78	7.77	7.63
3	3.22	2.82	7.29	7.30	7.34
4	2.52	2.28	6.76	7.20	7.25
5	3.07	3.05	7.39	7.43	7.39
6	3.32	3.55	7.67	7.70	7.61
7	4.09	3.28	7.56	7.65	7.57
8	2.91	2.13	6.67	7.24	7.27
9	3.25	3.01	7.08	7.31	7.26
10	4.09	2.98	7.35	7.33	7.42
11	3.50	3.23	7.62	7.72	7.66
12	2.19	3.23	7.46	7.58	7.49
avg	3.12	2.94	7.26	7.45	7.43
exp(298)	3.45	3.07	7.09	7.24	7.22
outer	α-CH_2	β-CH_2	o-CH	m-CH	p-CH
13	3.14	2.99	7.36	7.25	6.96
14	3.97	3.07	7.44	7.23	6.96
15	3.14	2.91	7.27	7.30	7.29
16	2.87	2.57	7.11	7.26	7.29
17	3.23	3.24	7.47	7.61	7.54
18	3.13	3.27	7.34	7.38	7.32
avg	3.24	3.01	7.33	7.34	7.23
exp(298)	3.06	2.91	7.11	7.19	7.22

[a] The $Au_{25}[S(CH_2)_2Ph]_{18}^{0}$ was used as the starting structure, where the density fitting was used to optimize all the charge states, using bvp86/lanl2dz/6-31g level of theory and bvp86/lanl2dz/6-31g** level of theory for calculating NMR and paramagnetic shifts.

Table A.6 : Calculated and experimental ^{13}C NMR chemical shifts of inner and outer ligands of $Au_{25}[S(CH_2)_2Ph]_{18}^{+1}$ [a] (bvp86 / 6-31g**/LANL2DZ)

inner	α-C	β-C	*i*-C	*o*-C	*m*-C	*p*-C
1	51.84	46.61	130.97	120.88	122.01	120.52
2	57.18	43.51	134.66	122.04	121.47	119.90
3	56.99	43.13	132.56	121.70	121.83	120.69
4	54.42	45.13	131.65	121.32	121.44	120.05
5	53.86	51.87	133.33	122.17	121.76	120.66
6	51.95	46.02	133.50	122.34	121.46	120.65
7	55.50	44.14	132.96	122.81	121.56	120.61
8	52.42	44.37	133.03	121.45	121.90	120.15
9	54.90	43.09	133.34	120.79	121.54	120.47
10	54.79	44.36	131.42	122.38	121.28	120.26
11	52.99	45.24	133.35	122.07	121.95	120.92
12	52.57	52.49	134.38	121.86	122.02	120.53
avg	54.12	45.83	132.93	121.82	121.69	120.45
exp(298)	38.19	42.64	139.52	129.27	129	127.28

outer	α-C	β-C	*i*-C	*o*-C	*m*-C	*p*-C
13	52.43	39.87	131.41	122.45	121.60	120.27
14	54.71	42.92	131.38	122.41	121.17	121.88
15	56.66	43.44	132.59	120.85	121.93	120.01
16	53.25	43.39	131.64	121.49	121.31	120.39
17	53.12	44.76	132.59	122.09	121.78	121.20
18	52.04	46.20	132.53	120.87	122.33	120.51
avg	53.70	43.43	132.02	121.69	121.69	120.71
exp(298)	34.79	40.13	139.78	129.16	129	127.28

[a] The $Au_{25}[S(CH_2)_2Ph]_{18}^{0}$ was used as the starting structure, where the density fitting was used to optimize all the charge states, using bvp86/lanl2dz/6-31g level of theory and bvp86/lanl2dz/6-31g** level of theory for calculating NMR and paramagnetic shifts.

Table A.7: Optimized geometry of $[Au_{25}(SEt)_{18}]^0$ using Turbomole V.6.3.1[80]. For the energy minimization step the s-vwn functional and the def2-TZVP basis set for all atoms with a def2-ecp effective core potential for all Au atoms was employed.

169

Au	1.1384	0.1221	2.5336
Au	1.4437	-2.2641	0.7798
Au	-1.1772	-1.5555	1.9897
Au	-1.6105	1.1438	1.9796
Au	0.7087	2.5317	0.8826
Au	2.7574	0.2611	0.3206
Au	0.0000	0.0000	0.0000
Au	-1.1106	-0.1241	4.6685
Au	3.3642	2.0836	2.6358
Au	3.8375	-1.4361	2.5633
Au	1.7813	-4.2259	-1.5384
Au	-0.3597	-4.5903	1.2650
Au	-3.9791	-0.6203	2.6096
S	2.0504	3.9153	2.2202
S	4.9208	0.4906	3.1813
S	2.9157	-3.5077	2.1600
S	1.1704	0.1630	4.8997
S	2.9131	-2.8428	-2.9921
S	0.9487	-5.8480	-0.1391
S	-1.7190	-3.6564	2.8653
S	-3.3913	-0.3641	4.8088
S	-4.8465	-0.9535	0.5099
C	1.0013	4.0668	3.6967
H	0.0253	4.4462	3.3203
H	0.8274	3.0511	4.0924
C	1.6093	4.9821	4.7166
H	1.7818	5.9880	4.2981
H	2.5763	4.5917	5.0735
H	0.9376	5.0869	5.5860
C	4.8688	0.4563	4.9965
H	5.3346	1.4021	5.3196
H	3.8080	0.4854	5.3060
C	5.5906	-0.7411	5.5423
H	5.1193	-1.6743	5.1859
H	5.5697	-0.7384	6.6444
H	6.6439	-0.7577	5.2188

C	4.0856	-4.4218	1.1125
H	3.6387	-5.4274	1.0139
H	4.0902	-3.9730	0.1047
C	5.4559	-4.4655	1.7199
H	6.1371	-5.0739	1.1012
H	5.4328	-4.8977	2.7335
H	5.8701	-3.4450	1.8033
C	1.8029	-1.4684	5.3947
H	2.8284	-1.5219	4.9710
H	1.8838	-1.4332	6.4950
C	0.9885	-2.6375	4.9333
H	0.8942	-2.6385	3.8316
H	-0.0357	-2.6012	5.3472
H	1.4619	-3.5878	5.2327
C	2.2220	-3.1603	-4.6424
H	1.1611	-2.8629	-4.6444
H	2.7545	-2.4554	-5.3058
C	2.4132	-4.5870	-5.0653
H	2.0536	-4.7384	-6.0971
H	1.8578	-5.2697	-4.3975
H	3.4747	-4.8801	-5.0247
C	-0.2574	-6.7396	-1.1605
H	-0.7085	-7.4926	-0.4930
H	-1.0535	-6.0278	-1.4514
C	0.3942	-7.3703	-2.3570
H	-0.3470	-7.9318	-2.9501
H	1.1984	-8.0649	-2.0655
H	0.8438	-6.5972	-3.0060
C	-3.4175	-4.0246	2.3436
H	-3.6806	-4.9614	2.8653
H	-4.0322	-3.2041	2.7713
C	-3.6295	-4.1333	0.8661
H	-3.0282	-4.9548	0.4367
H	-3.3200	-3.2018	0.3563
H	-4.6938	-4.3073	0.6346
C	-3.5557	-2.0218	5.5307
H	-4.6324	-2.2577	5.5003
H	-3.0238	-2.7336	4.8721
C	-3.0063	-2.0548	6.9276
H	-3.1284	-3.0576	7.3685
H	-3.5144	-1.3268	7.5803
H	-1.9304	-1.8053	6.9218
C	-5.9895	0.4313	0.2522

H	-6.2251	0.4019	-0.8280
H	-6.9034	0.1645	0.8093
C	-5.4522	1.7670	0.6609
H	-4.5132	1.9722	0.1098
H	-5.2108	1.7928	1.7389
H	-6.1748	2.5714	0.4370
Au	-1.1384	-0.1222	-2.5336
Au	-1.4437	2.2641	-0.7797
Au	1.1771	1.5555	-1.9897
Au	1.6105	-1.1438	-1.9795
Au	-0.7087	-2.5318	-0.8826
Au	-2.7573	-0.2611	-0.3206
Au	1.1105	0.1240	-4.6685
Au	-3.3642	-2.0836	-2.6358
Au	-3.8375	1.4361	-2.5633
Au	-1.7813	4.2258	1.5384
Au	0.3596	4.5903	-1.2650
Au	3.9791	0.6203	-2.6096
S	-2.0503	-3.9153	-2.2202
S	-4.9208	-0.4906	-3.1813
S	-2.9157	3.5077	-2.1600
S	-1.1705	-0.1631	-4.8997
S	-2.9131	2.8428	2.9922
S	-0.9488	5.8479	0.1392
S	1.7189	3.6564	-2.8653
S	3.3913	0.3641	-4.8088
S	4.8465	0.9535	-0.5099
C	-1.0012	-4.0667	-3.6967
H	-0.0252	-4.4461	-3.3203
H	-0.8273	-3.0510	-4.0924
C	-1.6092	-4.9820	-4.7167
H	-1.7816	-5.9879	-4.2983
H	-2.5761	-4.5915	-5.0736
H	-0.9374	-5.0867	-5.5861
C	-4.8688	-0.4563	-4.9965
H	-5.3346	-1.4021	-5.3197
H	-3.8080	-0.4853	-5.3060
C	-5.5906	0.7411	-5.5422
H	-5.1192	1.6744	-5.1858
H	-5.5697	0.7385	-6.6444
H	-6.6439	0.7578	-5.2188
C	-4.0855	4.4218	-1.1125
H	-3.6387	5.4274	-1.0140

H	-4.0901	3.9730	-0.1047
C	-5.4559	4.4654	-1.7199
H	-6.1371	5.0739	-1.1013
H	-5.4328	4.8975	-2.7335
H	-5.8701	3.4449	-1.8031
C	-1.8029	1.4684	-5.3947
H	-2.8284	1.5219	-4.9709
H	-1.8839	1.4331	-6.4950
C	-0.9884	2.6374	-4.9333
H	-0.8940	2.6384	-3.8317
H	0.0357	2.6011	-5.3473
H	-1.4618	3.5878	-5.2327
C	-2.2219	3.1602	4.6425
H	-1.1610	2.8629	4.6444
H	-2.7543	2.4553	5.3059
C	-2.4131	4.5869	5.0654
H	-2.0534	4.7384	6.0972
H	-1.8578	5.2697	4.3976
H	-3.4747	4.8799	5.0249
C	0.2573	6.7396	1.1605
H	0.7083	7.4927	0.4930
H	1.0534	6.0279	1.4515
C	-0.3944	7.3704	2.3570
H	0.3468	7.9320	2.9500
H	-1.1987	8.0649	2.0654
H	-0.8440	6.5973	3.0060
C	3.4175	4.0246	-2.3437
H	3.6805	4.9613	-2.8655
H	4.0321	3.2040	-2.7714
C	3.6296	4.1334	-0.8662
H	3.0284	4.9549	-0.4368
H	3.3201	3.2019	-0.3564
H	4.6939	4.3073	-0.6349
C	3.5556	2.0217	-5.5307
H	4.6323	2.2577	-5.5003
H	3.0236	2.7335	-4.8721
C	3.0062	2.0547	-6.9276
H	3.1282	3.0576	-7.3684
H	3.5143	1.3269	-7.5803
H	1.9303	1.8052	-6.9218
C	5.9895	-0.4313	-0.2522
H	6.2252	-0.4018	0.8279
H	6.9034	-0.1645	-0.8094

C	5.4521	-1.7670	-0.6607
H	4.5132	-1.9722	-0.1095
H	5.2106	-1.7928	-1.7388
H	6.1747	-2.5713	-0.4369

Table A.8: DFT-Computed Quadrupolar Tensors and Euler Angle Values for the Hyperfine and the Quadrupolar Tensors of $Au_{25}(SEt)_{18}^{0}$.

	Hyperfine Euler Angles[b]			Quadrupolar Tensors			Quadrupolar Euler Angles[b]		
Atom label[a]	α (°)	β (°)	γ (°)	Qx (MHz)	Qy (MHz)	Qz (MHz)	α (°)	β (°)	γ (°)
Au1(central)	-8.6	85.4	5.7	-17.3	24.7	-7.4	-0.74	1.06	-0.32
Au4(ico)	-2.0	22.8	-24.2	43.9	-76.5	32.7	5.8	6.5	81.2
Au3(ico)	-24.3	57.6	21.9	-59.3	13.3	46.0	-12.1	70.0	7.5
Au7(ico)	-4.7	70.2	42.7	31.0	-46.9	15.8	-34.3	23.7	-80.4
Au2(ico)	4.8	40.3	-48.7	30.7	19.3	-50.1	-34.7	19.1	-82.6
Au5(ico)	-39.9	63.5	-36.6	12.3	-61.1	48.8	-37.3	42.1	-38.3
Au6(ico)	35.1	37.0	55.0	47.1	16.6	-63.7	-25.2	55.6	7.7
Au8(staple)	-1.6	16.1	89.3	12.1	100.1	-112.2	-12.0	54.0	22.5
Au11(staple)	-7.1	86.0	-5.8	-67.1	24.5	42.6	-18.8	66.0	-55.0
Au9(staple)	22.5	43.9	49.7	15.0	-61.9	46.9	-21.7	47.6	-49.2
Au10(staple)	3.4	31.3	-0.4	-83.1	78.6	4.5	33.9	10.9	-63.1
Au12(staple)	27.7	58.2	15.9	100.9	1.9	-102.8	36.2	38.6	-47.4
Au13(staple)	-13.7	52.2	1.9	76.9	-86.3	9.4	-5.1	48.1	-5.3

[a] Except for the central atom, Au1, for symmetry reasons all other labels pertain to couples of equivalent Au atoms. [b] The values of α, β, and γ correspond to components x, y, and z, respectively.

Table A.9: Optimized geometry of $Au_{25}(SCH_3)_{18}^{1-}$ using $Au_{25}(SCH_2CH_2Ph)_{18}^{0}$ crystal structure as the as the starting structure.

115			
Au	0.0000	0.0000	0.0000
Au	1.5905	-2.2019	0.5970
Au	2.7025	0.2765	-0.5971
Au	0.5812	1.6057	-2.1936
Au	1.1015	-1.3092	-2.1917
Au	3.8907	-2.2964	-1.5236
Au	-1.6830	-0.3009	-2.1923
Au	-1.1646	-2.8999	-3.6426
Au	3.0919	0.4405	-3.6434
Au	-1.1116	-2.4788	-0.5957
Au	3.9326	2.2236	1.5236
Au	1.9285	-2.4569	3.6425
Au	-0.0442	-4.5169	1.5246
Au	-1.5905	2.2019	-0.5970
Au	-2.7025	-0.2765	0.5971
Au	-0.5812	-1.6057	2.1936
Au	-1.1015	1.3092	2.1917
Au	-3.8907	2.2964	1.5236
Au	1.6830	0.3009	2.1923
Au	1.1646	2.8999	3.6426
Au	-3.0919	-0.4405	3.6434
Au	1.1116	2.4788	0.5957
Au	-3.9326	-2.2236	-1.5236
Au	-1.9285	2.4569	-3.6425
Au	0.0442	4.5169	-1.5246
S	3.5644	-3.4931	0.4127
S	1.8957	2.3728	-3.9994
S	1.0700	-4.5802	3.5272
S	-1.2399	-4.8343	-0.4137
S	-3.4328	-3.2187	-3.5276
S	1.1072	-2.8322	-3.9967
S	4.5039	-1.3627	-3.5257
S	4.8033	1.3499	-0.4169
S	-3.0045	0.4550	-3.9976
S	-3.5644	3.4931	-0.4127
S	-1.8957	-2.3728	3.9994
S	-1.0700	4.5802	-3.5272

S	1.2399	4.8343	0.4137
S	3.4328	3.2187	3.5276
S	-1.1072	2.8322	3.9967
S	-4.5039	1.3627	3.5257
S	-4.8033	-1.3499	0.4169
S	3.0045	-0.4550	3.9976
C	-1.3129	1.8607	5.5032
H	-2.3648	1.5322	5.5542
H	-0.6672	0.9704	5.4917
H	-1.0635	2.4869	6.3730
C	3.5551	4.9777	3.1464
H	3.1683	5.5496	4.0028
H	4.6138	5.2236	2.9765
H	2.9740	5.2151	2.2371
C	4.6147	2.7052	-1.5974
H	5.3908	3.4615	-1.4089
H	4.7245	2.2843	-2.6145
H	3.6146	3.1594	-1.5170
C	-4.6147	-2.7052	1.5974
H	-4.7245	-2.2843	2.6145
H	-5.3908	-3.4615	1.4089
H	-3.6146	-3.1594	1.5170
C	-3.5551	-4.9777	-3.1464
H	-4.6138	-5.2236	-2.9765
H	-3.1683	-5.5496	-4.0028
H	-2.9740	-5.2151	-2.2371
C	1.3129	-1.8607	-5.5032
H	2.3648	-1.5322	-5.5542
H	1.0635	-2.4869	-6.3730
H	0.6672	-0.9704	-5.4917
C	0.9533	2.0659	-5.5071
H	0.5095	1.0596	-5.4997
H	0.1398	2.8095	-5.5560
H	1.6205	2.1690	-6.3762
C	6.0871	-0.5875	-3.1430
H	6.8297	-1.3806	-2.9708
H	6.3899	0.0325	-3.9998
H	6.0002	0.0357	-2.2348
C	4.6479	-2.6630	1.5972
H	4.5492	-1.5689	1.5197
H	4.3344	-2.9690	2.6131
H	5.6891	-2.9640	1.4096
C	-4.6479	2.6630	-1.5972

H	-4.3344	2.9690	-2.6131
H	-4.5492	1.5689	-1.5197
H	-5.6891	2.9640	-1.4096
C	-6.0871	0.5875	3.1430
H	-6.3899	-0.0325	3.9998
H	-6.8297	1.3806	2.9708
H	-6.0002	-0.0357	2.2348
C	-0.9533	-2.0659	5.5071
H	-1.6205	-2.1690	6.3762
H	-0.1398	-2.8095	5.5560
H	-0.5095	-1.0596	5.4997
C	-2.2673	-0.2073	-5.5055
H	-2.5084	-1.2826	-5.5570
H	-2.6868	0.3222	-6.3742
H	-1.1736	-0.0926	-5.4957
C	-2.5310	5.5669	-3.1451
H	-2.2136	6.6065	-2.9757
H	-3.2205	5.5182	-4.0008
H	-3.0266	5.1831	-2.2352
C	-0.0243	5.3545	1.5956
H	0.3954	5.2364	2.6123
H	-0.2858	6.4063	1.4080
H	-0.9212	4.7204	1.5158
C	2.2673	0.2073	5.5055
H	2.6868	-0.3222	6.3742
H	2.5084	1.2826	5.5570
H	1.1736	0.0926	5.4957
C	2.5310	-5.5669	3.1451
H	3.2205	-5.5182	4.0008
H	2.2136	-6.6065	2.9757
H	3.0266	-5.1831	2.2352
C	0.0243	-5.3545	-1.5956
H	0.2858	-6.4063	-1.4080
H	-0.3954	-5.2364	-2.6123
H	0.9212	-4.7204	-1.5158

Table A.10: Optimized geometry of $Au_{25}(SCH_3)_{18}^0$ using $Au_{25}(SCH_2CH_2Ph)_{18}^0$ crystal structure as the as the starting structure.

115			
Au	0.0000	0.0000	0.0000
Au	1.5929	-2.2042	0.6146
Au	2.7109	0.1880	-0.5722
Au	0.5267	1.5681	-2.2295
Au	1.1218	-1.3238	-2.1994
Au	3.9101	-2.3397	-1.5376
Au	-1.6644	-0.3188	-2.2262
Au	-1.1584	-2.9272	-3.6765
Au	3.0926	0.3842	-3.6388
Au	-1.0656	-2.4811	-0.6528
Au	3.8772	2.2379	1.5737
Au	1.9664	-2.4483	3.6602
Au	-0.0084	-4.4864	1.5303
Au	-1.5929	2.2042	-0.6146
Au	-2.7109	-0.1880	0.5722
Au	-0.5267	-1.5681	2.2295
Au	-1.1218	1.3238	2.1994
Au	-3.9101	2.3397	1.5376
Au	1.6644	0.3188	2.2262
Au	1.1584	2.9272	3.6765
Au	-3.0926	-0.3842	3.6388
Au	1.0656	2.4811	0.6528
Au	-3.8772	-2.2379	-1.5737
Au	-1.9664	2.4483	-3.6602
Au	0.0084	4.4864	-1.5303
S	3.5543	-3.5147	0.4031
S	1.9111	2.3239	-3.9687
S	1.1071	-4.5664	3.5320
S	-1.2542	-4.8070	-0.3713
S	-3.4255	-3.2391	-3.5851
S	1.1121	-2.8528	-4.0030
S	4.5304	-1.3995	-3.5314
S	4.6997	1.4079	-0.3952
S	-3.0219	0.4378	-4.0100
S	-3.5543	3.5147	-0.4031
S	-1.9111	-2.3239	3.9687
S	-1.1071	4.5664	-3.5320

S	1.2542	4.8070	0.3713
S	3.4255	3.2391	3.5851
S	-1.1121	2.8528	4.0030
S	-4.5304	1.3995	3.5314
S	-4.6997	-1.4079	0.3952
S	3.0219	-0.4378	4.0100
C	-1.3217	1.8817	5.5091
H	-2.3793	1.5751	5.5714
H	-0.6910	0.9807	5.4922
H	-1.0549	2.5052	6.3752
C	3.5694	4.9935	3.1887
H	3.1829	5.5764	4.0373
H	4.6325	5.2256	3.0297
H	3.0021	5.2310	2.2722
C	4.4556	2.7696	-1.5550
H	5.2184	3.5384	-1.3642
H	4.5669	2.3664	-2.5778
H	3.4477	3.2012	-1.4503
C	-4.4556	-2.7696	1.5550
H	-4.5669	-2.3664	2.5778
H	-5.2184	-3.5384	1.3642
H	-3.4477	-3.2012	1.4503
C	-3.5694	-4.9935	-3.1887
H	-4.6325	-5.2256	-3.0297
H	-3.1829	-5.5764	-4.0373
H	-3.0021	-5.2310	-2.2722
C	1.3217	-1.8817	-5.5091
H	2.3793	-1.5751	-5.5714
H	1.0549	-2.5052	-6.3752
H	0.6910	-0.9807	-5.4922
C	0.9731	2.0671	-5.4876
H	0.4983	1.0751	-5.5010
H	0.1871	2.8390	-5.5353
H	1.6546	2.1641	-6.3457
C	6.0983	-0.5983	-3.1365
H	6.8497	-1.3806	-2.9555
H	6.4004	0.0176	-3.9960
H	5.9961	0.0309	-2.2357
C	4.6638	-2.7212	1.5872
H	4.6062	-1.6248	1.5099
H	4.3403	-3.0177	2.6027
H	5.6924	-3.0620	1.4005
C	-4.6638	2.7212	-1.5872

H	-4.3403	3.0177	-2.6027
H	-4.6062	1.6248	-1.5099
H	-5.6924	3.0620	-1.4005
C	-6.0983	0.5983	3.1365
H	-6.4004	-0.0176	3.9960
H	-6.8497	1.3806	2.9555
H	-5.9961	-0.0309	2.2357
C	-0.9731	-2.0671	5.4876
H	-1.6546	-2.1641	6.3457
H	-0.1871	-2.8390	5.5353
H	-0.4983	-1.0751	5.5010
C	-2.3022	-0.2141	-5.5308
H	-2.5501	-1.2870	-5.5897
H	-2.7340	0.3229	-6.3882
H	-1.2082	-0.1019	-5.5354
C	-2.5564	5.5718	-3.1603
H	-2.2258	6.6089	-3.0034
H	-3.2431	5.5241	-4.0179
H	-3.0582	5.2047	-2.2476
C	0.0562	5.4150	1.5798
H	0.4904	5.2733	2.5871
H	-0.1310	6.4821	1.3911
H	-0.8854	4.8486	1.5234
C	2.3022	0.2141	5.5308
H	2.7340	-0.3229	6.3882
H	2.5501	1.2870	5.5897
H	1.2082	0.1019	5.5354
C	2.5564	-5.5718	3.1603
H	3.2431	-5.5241	4.0179
H	2.2258	-6.6089	3.0034
H	3.0582	-5.2047	2.2476
C	-0.0562	-5.4150	-1.5798
H	0.1310	-6.4821	-1.3911
H	-0.4904	-5.2733	-2.5871
H	0.8854	-4.8486	-1.5234

Table A.10: Optimized geometry of $Au_{25}(SCH_3)_{18}^{1+}$ using $Au_{25}(SCH_2CH_2Ph)_{18}^{0}$ crystal structure as the as the starting structure.

115			
Au	0.0000	0.0000	0.0000
Au	1.5923	-2.2370	0.6216
Au	2.7603	0.0322	-0.4610
Au	0.4039	1.4985	-2.3124
Au	1.1570	-1.3080	-2.2371
Au	3.9271	-2.4039	-1.5608
Au	-1.6821	-0.3604	-2.2495
Au	-1.1000	-2.9892	-3.7366
Au	3.0988	0.3279	-3.6288
Au	-0.9218	-2.5216	-0.7932
Au	3.7871	2.2949	1.6495
Au	2.0468	-2.4478	3.6710
Au	0.0196	-4.4562	1.5680
Au	-1.5923	2.2370	-0.6216
Au	-2.7603	-0.0322	0.4610
Au	-0.4039	-1.4985	2.3124
Au	-1.1570	1.3080	2.2371
Au	-3.9271	2.4039	1.5608
Au	1.6821	0.3604	2.2495
Au	1.1000	2.9892	3.7366
Au	-3.0988	-0.3279	3.6288
Au	0.9218	2.5216	0.7932
Au	-3.7871	-2.2949	-1.6495
Au	-2.0468	2.4478	-3.6710
Au	-0.0196	4.4562	-1.5680
S	3.5111	-3.6100	0.3466
S	1.8959	2.2503	-3.9356
S	1.1626	-4.5525	3.5540
S	-1.2832	-4.7727	-0.2909
S	-3.3645	-3.3078	-3.6619
S	1.1666	-2.8449	-4.0475
S	4.5810	-1.4192	-3.5198
S	4.5553	1.4964	-0.3448
S	-3.0829	0.4265	-3.9924
S	-3.5111	3.6100	-0.3466
S	-1.8959	-2.2503	3.9356
S	-1.1626	4.5525	-3.5540

S	1.2832	4.7727	0.2909
S	3.3645	3.3078	3.6619
S	-1.1666	2.8449	4.0475
S	-4.5810	1.4192	3.5198
S	-4.5553	-1.4964	0.3448
S	3.0829	-0.4265	3.9924
C	-1.3396	1.8787	5.5615
H	-2.3770	1.5069	5.6119
H	-0.6485	1.0232	5.5709
H	-1.1319	2.5320	6.4214
C	3.5403	5.0569	3.2557
H	3.1434	5.6508	4.0915
H	4.6108	5.2713	3.1248
H	3.0026	5.2982	2.3240
C	4.1984	2.8365	-1.4963
H	4.9049	3.6559	-1.2993
H	4.3449	2.4514	-2.5204
H	3.1631	3.1958	-1.3849
C	-4.1984	-2.8365	1.4963
H	-4.3449	-2.4514	2.5204
H	-4.9049	-3.6559	1.2993
H	-3.1631	-3.1958	1.3849
C	-3.5403	-5.0569	-3.2557
H	-4.6108	-5.2713	-3.1248
H	-3.1434	-5.6508	-4.0915
H	-3.0026	-5.2982	-2.3240
C	1.3396	-1.8787	-5.5615
H	2.3770	-1.5069	-5.6119
H	1.1319	-2.5320	-6.4214
H	0.6485	-1.0232	-5.5709
C	0.9909	2.0450	-5.4822
H	0.5210	1.0530	-5.5453
H	0.2086	2.8205	-5.5216
H	1.6951	2.1773	-6.3169
C	6.1216	-0.5862	-3.0843
H	6.8838	-1.3551	-2.8927
H	6.4306	0.0353	-3.9368
H	5.9896	0.0393	-2.1862
C	4.6708	-2.9209	1.5475
H	4.7038	-1.8235	1.4846
H	4.3211	-3.2043	2.5581
H	5.6688	-3.3431	1.3604
C	-4.6708	2.9209	-1.5475

H	-4.3211	3.2043	-2.5581
H	-4.7038	1.8235	-1.4846
H	-5.6688	3.3431	-1.3604
C	-6.1216	0.5862	3.0843
H	-6.4306	-0.0353	3.9368
H	-6.8838	1.3551	2.8927
H	-5.9896	-0.0393	2.1862
C	-0.9909	-2.0450	5.4822
H	-1.6951	-2.1773	6.3169
H	-0.2086	-2.8205	5.5216
H	-0.5210	-1.0530	5.5453
C	-2.3975	-0.2152	-5.5338
H	-2.6574	-1.2844	-5.5990
H	-2.8471	0.3316	-6.3754
H	-1.3035	-0.1080	-5.5608
C	-2.5761	5.6033	-3.1752
H	-2.2136	6.6348	-3.0576
H	-3.2824	5.5523	-4.0161
H	-3.0652	5.2771	-2.2410
C	0.1795	5.5578	1.4893
H	0.5838	5.3669	2.5005
H	0.1556	6.6384	1.2866
H	-0.8351	5.1394	1.4300
C	2.3975	0.2152	5.5338
H	2.8471	-0.3316	6.3754
H	2.6574	1.2844	5.5990
H	1.3035	0.1080	5.5608
C	2.5761	-5.6033	3.1752
H	3.2824	-5.5523	4.0161
H	2.2136	-6.6348	3.0576
H	3.0652	-5.2771	2.2410
C	-0.1795	-5.5578	-1.4893
H	-0.1556	-6.6384	-1.2866
H	-0.5838	-5.3669	-2.5005
H	0.8351	-5.1394	-1.4300

References

[1] Link, S.; Beeby, A.; FitzGerald, S.; El-Sayed, M. A.; Schaaff, T. G.; Whetten, R. L. Visible to Infrared Luminescence from a 28-Atom Gold Cluster. *J. Phys. Chem. B.* **2002**, *106*, 3410–3415.

[2] Bulusu, S.; Li, X.; Wang, L.-S.; Zeng, X. C. Evidence of hollow golden cages. *Proc. Natl. Acad. Sci. U. S. A.* **2006**, *103*, 8326–8330.

[3] Furche, F.; Ahlrichs, R.; Weis, P.; Jacob, C.; Gilb, S.; Bierweiler, T.; Kappes, M. M. The structures of small gold cluster anions as determined by a combination of ion mobility measurements and density functional calculations. *J. Chem. Phys.* **2002**, *117*, 6982.

[4] Häkkinen, H.; Yoon, B.; Landman, U.; Li, X.; Zhai, H. J.; Wang, L. S. On the electronic and atomic structures of small AuN - (N = 4-14) clusters: A photoelectron spectroscopy and density-functional study. *J. Phys. Chem. A.* **2003**, *107*, 6168–6175.

[5] Haruta, M. *Size- and support-dependency in the catalysis of gold*, 1997.

[6] Huang, W.; Wang, L. S. Probing the 2D to 3D structural transition in gold cluster anions using argon tagging. *Phys. Rev. Lett.* **2009**, *102*, 3–6.

[7] Johansson, M. P.; Lechtken, A.; Schooss, D.; Kappes, M. M.; Furche, F. 2D-3D transition of gold cluster anions resolved. *Phys. Rev. A - At. Mol. Opt. Phys.* **2008**, *77*, 1–7.

[8] Lechtken, A.; Neiss, C.; Kappes, M. M.; Schooss, D. Structure determination of gold clusters by trapped ion electron diffraction: Au(14)(-)-Au(19)(-). *Phys. Chem. Chem. Phys.* **2009**, *11*, 4344–4350.

[9] Li, J. Au20: A Tetrahedral Cluster. *Science (80-.).* **2003**, *299*, 864–867.

[10] Schooss, D.; Weis, P.; Hampe, O.; Kappes, M. M. Determining the size-dependent structure of ligand-free gold-cluster ions. *Philos. Trans. A. Math. Phys. Eng. Sci.* **2010**, *368*, 1211–1243.

[11] Wang, L.-M.; Wang, L.-S. Probing the electronic properties and structural evolution of anionic gold clusters in the gas phase. *Nanoscale*. **2012**, *4*, 4038.

[12] Xing, X.; Yoon, B.; Landman, U.; Parks, J. H. Structural evolution of Au nanoclusters: From planar to cage to tubular motifs. *Phys. Rev. B - Condens. Matter Mater. Phys.* **2006**, *74*, 1–6.

[13] Schaaff, T. G.; Knight, G.; Shafigullin, M. N.; Borkman, R. F.; Whetten, R. L. Isolation and Selected Properties of a 10.4 kDa Gold:Glutathione Cluster Compound. *J. Phys. Chem. B.* **1998**, *102*, 10643–10646.

[14] Euliss, L. E.; Grancharov, S. G.; O'Brien, S.; Deming, T. J.; Stucky, G. D.; Murray, C. B.; Held, G. a. Cooperative Assembly of Magnetic Nanoparticles and Block Copolypeptides in Aqueous Media. *Nano Lett.* **2003**, *3*, 1489–1493.

[15] Gittins, D. I.; Caruso, F. Biological and physical applications of water-based metal nanoparticles synthesised in organic solution. *ChemPhysChem*. **2002**, *3*, 110–113.

[16] Jadzinsky, P. D.; Calero, G.; Ackerson, C. J.; Bushnell, D. a; Kornberg, R. D. Structure of a thiol monolayer-protected gold nanoparticle at 1.1 A resolution. *Science*. **2007**, *318*, 430–3.

[17] Häkkinen, H.; Walter, M.; Grönbeck, H. Divide and protect: capping gold nanoclusters with molecular gold-thiolate rings. *J. Phys. Chem. B*. **2006**, *110*, 9927–31.

[18] Negishi, Y.; Takasugi, Y.; Sato, S.; Yao, H.; Kimura, K.; Tsukuda, T. Magic-numbered Au(n) clusters protected by glutathione monolayers (n = 18, 21, 25, 28, 32, 39): isolation and spectroscopic characterization. *J. Am. Chem. Soc.* **2004**, *126*, 6518–9.

[19] Schaaff, T. G.; Whetten, R. L. Giant Gold−Glutathione Cluster Compounds: Intense Optical Activity in Metal-Based Transitions. *J. Phys. Chem. B*. **2000**, *104*, 2630–2641.

[20] Donkers, R. L.; Lee, D.; Murray, R. W. Synthesis and Isolation of the Molecule-like Cluster Au 38 (PhCH 2 CH 2 S) 24. *Langmuir*. **2004**, *20*, 1945–1952.

[21] Iwasa, T.; Nobusada, K. Gold-thiolate core-in-cage cluster Au25(SCH3)18 shows localized spins in charged states. *Chem. Phys. Lett.* **2007**, *441*, 268–272.

[22] Iwasa, T.; Nobusada, K. Theoretical Investigation of Optimized Structures of Thiolated Gold Cluster [Au25(SCH3)18]+. *J. Phys. Chem. C*. **2007**, *111*, 45–49.

[23] Nobusada, K. Electronic Structure and Photochemical Properties of a Monolayer-Protected Gold Cluster. *J. Phys. Chem. B.* **2004**, *108*, 11904–11908.

[24] Negishi, Y.; Nobusada, K.; Tsukuda, T. Glutathione-Protected Gold Clusters Revisited: Bridging the Gap between Gold(I)−Thiolate Complexes and Thiolate-Protected Gold Nanocrystals. *J. Am. Chem. Soc.* **2005**, *127*, 5261–5270.

[25] Tracy, J. B.; Kalyuzhny, G.; Crowe, M. C.; Balasubramanian, R.; Choi, J.-P.; Murray, R. W. Poly(ethylene glycol) Ligands for High-Resolution Nanoparticle Mass Spectrometry. *J. Am. Chem. Soc.* **2007**, *129*, 6706–6707.

[26] Fields-Zinna, C. A.; Sampson, J. S.; Crowe, M. C.; Tracy, J. B.; Parker, J. F.; DeNey, A. M.; Muddiman, D. C.; Murray, R. W. Tandem Mass Spectrometry of Thiolate-Protected Au Nanoparticles Na x Au 25 (SC 2 H 4 Ph) 18− y (S(C 2 H 4 O) 5 CH 3) y. *J. Am. Chem. Soc.* **2009**, *131*, 13844–13851.

[27] Tracy, J. B.; Crowe, M. C.; Parker, J. F.; Hampe, O.; Fields-Zinna, C. A.; Dass, A.; Murray, R. W. Electrospray Ionization Mass Spectrometry of Uniform and Mixed Monolayer Nanoparticles: Au 25 [S(CH 2) 2 Ph] 18 and Au 25 [S(CH 2) 2 Ph] 18 - x (SR) x. *J. Am. Chem. Soc.* **2007**, *129*, 16209–16215.

[28] Heaven, M. W.; Dass, A.; White, P. S.; Holt, K. M.; Murray, R. W. Crystal structure of the gold nanoparticle [N(C8H17)4][Au25(SCH2CH2Ph)18]. *J. Am. Chem. Soc.* **2008**, *130*, 3754–5.

[29] Zhu, M.; Aikens, C. M.; Hollander, F. J.; Schatz, G. C.; Jin, R. Correlating the crystal structure of a thiol-protected Au25 cluster and optical properties. *J. Am. Chem. Soc.* **2008**, *130*, 5883–5.

[30] Akola, J.; Walter, M.; Whetten, R. L.; Häkkinen, H.; Grönbeck, H. On the structure of thiolate-protected Au25. *J. Am. Chem. Soc.* **2008**, *130*, 3756–7.

[31] Templeton, A. C.; Wuelfing, W. P.; Murray, R. W. Monolayer-Protected Cluster Molecules. *Acc. Chem. Res.* **2000**, *33*, 27–36.

[32] Zhu, M.; Eckenhoff, W. T.; Pintauer, T.; Jin, R. Conversion of Anionic [Au25(SCH2CH2Ph)18]− Cluster to Charge Neutral Cluster via Air Oxidation. *J. Phys. Chem. C*. **2008**, *112*, 14221–14224.

[33] *Absorption and Scattering of Light by Small Particles*. ; Bohren, C. F.; Huffman, D. R., Eds.; Wiley-VCH Verlag GmbH: Weinheim, Germany, 1998.

[34] Schaaff, T. G.; Shafigullin, M. N.; Khoury, J. T.; Vezmar, I.; Whetten, R. L.; Cullen, W. G.; First, P. N.; Gutiérrez-Wing, C.; Ascensio, J.; Jose-Yacamán, M. J. Isolation of Smaller Nanocrystal Au Molecules: Robust Quantum Effects in Optical Spectra. *J. Phys. Chem. B.* **1997**, *101*, 7885–7891.

[35] Wyrwas, R. B.; Alvarez, M. M.; Khoury, J. T.; Price, R. C.; Schaaff, T. G.; Whetten, R. L. The colours of nanometric gold : OOptical response functions of selected gold-cluster thiolates. *Eur. Phys. J. D*. **2007**, *43*, 91–95.

[36] Kelly, K. L.; Coronado, E.; Zhao, L. L.; Schatz, G. C. The Optical Properties of Metal Nanoparticles: The Influence of Size, Shape, and Dielectric Environment. *J. Phys. Chem. B*. **2003**, *107*, 668–677.

[37] Ingram, R. S.; Hostetler, M. J.; Murray, R. W.; Schaaff, T. G.; Khoury, J. T.; Whetten, R. L.; Bigioni, T. P.; Guthrie, D. K.; First, P. N. 28 kDa Alkanethiolate-Protected Au Clusters Give Analogous Solution Electrochemistry and STM Coulomb Staircases. *J. Am. Chem. Soc.* **1997**, *119*, 9279–9280.

[38] Chen, S.; Ingram, R. S.; Hostetler, M. J.; Pietron, J. J.; Murray, R. W.; Schaaff, T. G.; Khoury, J. T.; Alvarez, M. M.; Whetten, R. L. Gold Nanoelectrodes of Varied Size: Transition to Molecule-Like Charging. *Science (80-.).* **1998**, *280*, 2098–2101.

[39] Lee, D.; Donkers, R. L.; DeSimone, J. M.; Murray, R. W. Voltammetry and Electron-Transfer Dynamics in a Molecular Melt of a 1.2 nm Metal Quantum Dot. *J. Am. Chem. Soc.* **2003**, *125*, 1182–1183.

[40] Wu, Z.; Jin, R. On the Ligand's Role in the Fluorescence of Gold Nanoclusters. *Nano Lett.* **2010**, *25*, 2568–2573.

[41] Valden, M. Onset of Catalytic Activity of Gold Clusters on Titania with the Appearance of Nonmetallic Properties. *Science (80-.).* **1998**, *281*, 1647–1650.

[42] Pasquato, L.; Pengo, P.; Scrimin, P. Functional gold nanoparticles for recognition and catalysis. *J. Mater. Chem.* **2004**, *14*, 3481–3487.

[43] Daniel, M. C.; Astruc, D. Gold nanoparticles: Assembly, supramolecular chemistry, quantum-size-related properties, and applications toward biology, catalysis, and nanotechnology. *Chem. Rev.* **2004**, *104*, 293–346.

[44] Qian, X.; Peng, X.-H.; Ansari, D. O.; Yin-Goen, Q.; Chen, G. Z.; Shin, D. M.; Yang, L.; Young, A. N.; Wang, M. D.; Nie, S. In vivo tumor targeting and spectroscopic detection with surface-enhanced Raman nanoparticle tags. *Nat. Biotechnol.* **2007**, *26*, 83–90.

[45] Rosi, N. L.; Giljohann, D. A.; Thaxton, C. S.; Lytton-Jean, A. K. R.; Han, M. S.; Mirkin, C. A. Oligonucleotide-Modified Gold Nanoparticles for Intracellular Gene Regulation. *Science (80-.).* **2006**, *312*, 1027–1030.

[46] Mukhopadhyay, R.; Mitra, S.; Johnson, M.; Rajeev Kumar, V. R.; Pradeep, T. Evolution of the alkyl-chain dynamics in monolayer-protected gold clusters. *Phys. Rev. B.* **2007**, *75*, 075414.

[47] Fabris, L.; Antonello, S.; Armelao, L.; Donkers, R. L.; Polo, F.; Toniolo, C.; Maran, F. Gold Nanoclusters Protected by Conformationally Constrained Peptides. *J. Am. Chem. Soc.* **2006**, *128*, 326–336.

[48] Kalsin, A. M.; Kowalczyk, B.; Wesson, P.; Paszewski, M.; Grzybowski, B. A. Studying the Thermodynamics of Surface Reactions on Nanoparticles by Electrostatic Titrations. *J. Am. Chem. Soc.* **2007**, *129*, 6664–6665.

[49] Botan, V.; Backus, E. H. G.; Pfister, R.; Moretto, A.; Crisma, M.; Toniolo, C.; Nguyen, P. H.; Stock, G.; Hamm, P. Energy transport in peptide helices. *Proc. Natl. Acad. Sci.* **2007**, *104*, 12749–12754.

[50] Becucci, L.; Guryanov, I.; Maran, F.; Guidelli, R. Effect of a strong interfacial electric field on the orientation of the dipole moment of thiolated aib-oligopeptides tethered to mercury on either the N- or C-terminus. *J. Am. Chem. Soc.* **2010**, *132*, 6194–204.

[51] Holm, A. H.; Ceccato, M.; Donkers, R. L.; Fabris, L.; Pace, G.; Maran, F. Effect of peptide ligand dipole moments on the redox potentials of Au38 and Au140 nanoparticles. *Langmuir*. **2006**, *22*, 10584–9.

[52] *Jaguar version 7.6.* ; Schrodinger, LLC: New York, NY, 2009.

[53] Frisch, M. J.; Trucks, G. W.; Schlegel, H. B.; Scuseria, G. E.; Robb, M. A.; Cheeseman, J. R.; Scalmani, G.; Barone, V.; Mennucci, B.; Petersson, G. A.; Nakatsuji, H.; Caricato, M.; Li, X.; Hratchian, H. P.; Izmaylov, A. F.; Bloino, J.; Zheng, J.; Sonnenberg, J. L.; Hada, M.; Ehara, M.; Toyota, K.; Fukuda, R.; Hasegawa, J.; Ishida, M.; Nakajima, T.; Honda, Y.; Kitao, O.; Nakai, H.; Vreven, T.; Montgomery Jr., J. A.; Peralta, J. E.; Ogliaro, F.; Bearpark, M.; Heyd, J. J.; Brothers, E.; Kudin, K. N.; Staroverov, V. N.; Kobayashi, R.; Normand, J.; Raghavachari, K.; Rendell, A.; Burant, J. C.; Iyengar, S. S.; Tomasi, J.; Cossi, M.; Rega, N.; Millam, J. M.; Klene, M.; Knox, J. E.; Cross, J. B.; Bakken, V.; Adamo, C.; Jaramillo, J.; Gomperts, R.; Stratmann, R. E.; Yazyev, O.; Austin, A. J.; Cammi, R.; Pomelli, C.; Ochterski, J. W.; Martin, R. L.; Morokuma, K.; Zakrzewski, V. G.; Voth, G. A.; Salvador, P.; Dannenberg, J. J.; Dapprich, S.; Daniels, A. D.; Farkas, O.; Foresman, J. B.; Ortiz, J. V.; Cioslowski, J.; Fox, D. J. *Gaussian09,Revision A.01*, Wallingford CT, 2009.

[54] Ponder, J. W. *Tinker*, *version 6.3*, 2014.

[55] Rappe, a. K.; Casewit, C. J.; Colwell, K. S.; Goddard, W. a.; Skiff, W. M. UFF, a full periodic table force field for molecular mechanics and molecular dynamics simulations. *J. Am. Chem. Soc.* **1992**, *114*, 10024–10035.

[56] Cornell, W. D.; Cieplak, P.; Bayly, C. I.; Gould, I. R.; Merz, K. M.; Ferguson, D. M.; Spellmeyer, D. C.; Fox, T.; Caldwell, J. W.; Kollman, P. a. A Second Generation Force Field for the Simulation of Proteins, Nucleic Acids, and Organic Molecules. *J. Am. Chem. Soc.* **1995**, *117*, 5179–5197.

[57] London, F. Quantum theory of interatomic currents in aromatic compounds. *J. Phys. Radium*. **1937**, *8*, 397–409.

[58] Ditchfield, R. Self-consistent perturbation theory of diamagnetism. *Mol. Phys.* **1974**, *27*, 789–807.

[59] Wolinski, K.; Hinton, J. F.; Pulay, P. Efficient implementation of the gauge-independent atomic orbital method for NMR chemical shift calculations. *J. Am. Chem. Soc.* **1990**, *112*, 8251–8260.

[60] McWeeny, R. Perturbation Theory for the Fock-Dirac Density Matrix. *Phys. Rev.* **1962**, *126*, 1028–1034.

[61] Cheeseman, J. R.; Trucks, G. W.; Keith, T. A.; Frisch, M. J. A comparison of models for calculating nuclear magnetic resonance shielding tensors. *J. Chem. Phys.* **1996**, *104*, 5497.

[62] Pavone, V.; Lombardi, A.; Saviano, M.; Blasio, B. Di; Nastri, F.; Fattorusso, R.; Zaccaro, L.; Maglio, O.; Yamada, T.; Omote, Y.; Kuwata, S. Mixed conformation in C?,?-disubstituted tripeptides: X-ray crystal structures of Z-Aib-Dph-Gly-Ome and Bz-Dph-Dph-Gly-Ome. *Biopolymers*. **1994**, *34*, 1595–1604.

[63] Wieczorek, R.; Dannenberg, J. J. Comparison of Fully Optimized α- and 3 10 -Helices with Extended β-Strands. An ONIOM Density Functional Theory Study. *J. Am. Chem. Soc.* **2004**, *126*, 14198–14205.

[64] Toniolo, C.; Crisma, M.; Bonora, G. M.; Benedetti, E.; Dl Blasio, B.; Pavone, V.; Pedone, C.; Santini, A. Preferred conformation of the terminally blocked (Aib)10 homo-oligopeptide: A long, regular 310-helix. *Biopolymers*. **1991**, *31*, 129–138.

[65] Improta, R.; Barone, V.; Kudin, K. N.; Scuseria, G. E. Structure and Conformational Behavior of Biopolymers by Density Functional Calculations Employing Periodic Boundary Conditions. I. The Case of Polyglycine, Polyalanine, and Poly-α-aminoisobutyric Acid in Vacuo. *J. Am. Chem. Soc*. **2001**, *123*, 3311–3322.

[66] Viswanathan, R.; Asensio, A.; Dannenberg, J. J. Cooperative Hydrogen-Bonding in Models of Antiparallel Î^2-Sheets. *J. Phys. Chem. A*. **2004**, *108*, 9205–9212.

[67] Parker, J. F.; Choi, J.; Wang, W.; Murray, R. W. Electron Self-exchange Dynamics of the Nanoparticle Couple [Au 25 (SC2Ph) 18] 0/1− By Nuclear Magnetic Resonance Line-Broadening. *J. Phys. Chem. C*. **2008**, *112*, 13976–13981.

[68] Antonello, S.; Holm, A. H.; Instuli, E.; Maran, F. Molecular Electron-Transfer Properties of Au38 Clusters. *J. Am. Chem. Soc.* **2007**, *129*, 9836–9837.

[69] Choi, J.; Murray, R. W. Electron self-exchange between Au140(+/0) nanoparticles is faster than that between Au38(+/0) in solid-state, mixed-valent films. *J. Am. Chem. Soc.* **2006**, *128*, 10496–502.

[70] Guo, R.; Song, Y.; Wang, G.; Murray, R. W. Does core size matter in the kinetics of ligand exchanges of monolayer-protected Au clusters? *J. Am. Chem. Soc*. **2005**, *127*, 2752–2757.

[71] Bertini, I.; Luchinat, C.; Parigi, G. *Solution NMR of Paramagnetic Molecules: Applications to Metallobiomolecules and Models*. ; volume 2.; Elsevier B.V., 2001.

[72] Bertini, I.; Luchinat, C.; Parigi, G. Magnetic susceptibility in paramagnetic NMR. *Prog. Nucl. Magn. Reson. Spectrosc.* **2002**, *40*, 249–273.

[73] Kaupp, M.; Buhl, M.; Malkin, V. G. *Calculations of NMR and EPR Parameters*. ; Wiley-VCH, 2004.

[74] Rastrelli, F.; Bagno, A. Predicting the NMR spectra of paramagnetic molecules by DFT: application to organic free radicals and transition-metal complexes. *Chemistry*. **2009**, *15*, 7990–8004.

[75] Frisch, M. J.; Trucks, G. W.; Schlegel, H. B.; Scuseria, G. E.; Robb, M. A.; Cheeseman, J. R.; Scalmani, G.; Barone, V.; Mennucci, B.; Petersson, G. A.; Nakatsuji, H.; Caricato, M.; Li, X.; Hratchian, H. P.; Izmaylov, A. F.; Bloino, J.; Zheng, J.; Sonnenberg, J. L.; Hada, M.; Ehara, M.; Toyota, K.; Fukuda, R.; Hasegawa, J.; Ishida, M.; Nakajima, T.; Honda, Y.; Kitao, O.; Nakai, H.; Vreven, T.; Montgomery Jr., J. A.; Peralta, J. E.; Ogliaro, F.; Bearpark, M.; Heyd, J. J.; Brothers, E.; Kudin, K. N.; Staroverov, V. N.; Kobayashi, R.; Normand, J.; Raghavachari, K.; Rendell, A.; Burant, J. C.; Iyengar, S. S.; Tomasi, J.; Cossi, M.; Rega, N.; Millam, J. M.; Klene, M.; Knox, J. E.; Cross, J. B.; Bakken, V.; Adamo, C.; Jaramillo, J.; Gomperts, R.; Stratmann, R. E.; Yazyev, O.; Austin, A. J.; Cammi, R.; Pomelli, C.; Ochterski, J. W.; Martin, R. L.; Morokuma, K.; Zakrzewski, V. G.; Voth, G. A.; Salvador, P.; Dannenberg, J. J.; Dapprich, S.; Daniels, A. D.; Farkas, O.; Foresman, J. B.; Ortiz, J. V.; Cioslowski, J.; Fox, D. J. *Gaussian09, Revision A.02*, Wallingford CT, 2009.

[76] Barth, U. Von; Hedin, L. A local exchange-correlation potential for the spin polarized case. i. *J. Phys. C Solid State Phys.* **1972**, *5*, 1629–1642.

[77] Autschbach, J.; Patchkovskii, S.; Pritchard, B. Calculation of Hyperfine Tensors and Paramagnetic NMR Shifts Using the Relativistic Zeroth-Order Regular Approximation and Density Functional Theory. *J. Chem. Theory Comput.* **2011**, *7*, 2175–2188.

[78] Venzo, A.; Antonello, S.; Gascón, J. A.; Guryanov, I.; Leapman, R. D.; Perera, N. V; Sousa, A.; Zamuner, M.; Zanella, A.; Maran, F. Effect of the charge state (z = -1, 0, +1) on the nuclear magnetic resonance of monodisperse Au25[S(CH2)2Ph]18(z) clusters. *Anal. Chem.* **2011**, *83*, 6355–62.

[79] Neese, F. The ORCA program system. *Wiley Interdiscip. Rev. Comput. Mol. Sci.* **2012**, *2*, 73–78.

[80] Ahlrichs, R.; Bär, M.; Häser, M.; Horn, H.; Kölmel, C. Electronic structure calculations on workstation computers: The program system turbomole. *Chem. Phys. Lett.* **1989**, *162*, 165–169.

[81] Wüllen, C. van Molecular density functional calculations in the regular relativistic approximation: Method, application to coinage metal diatomics, hydrides, fluorides and

chlorides, and comparison with first-order relativistic calculations. *J. Chem. Phys.* **1998**, *109*, 392.

[82] Pantazis, D. a.; Chen, X.-Y.; Landis, C. R.; Neese, F. All-Electron Scalar Relativistic Basis Sets for Third-Row Transition Metal Atoms. *J. Chem. Theory Comput.* **2008**, *4*, 908–919.

[83] Dainese, T.; Antonello, S.; Gascón, J. A.; Pan, F.; Perera, N. V; Ruzzi, M.; Venzo, A.; Zoleo, A.; Rissanen, K.; Maran, F. Au25(SEt)18, a Nearly Naked Thiolate-Protected Au25 Cluster: Structural Analysis by Single Crystal X-ray Crystallography and Electron Nuclear Double Resonance. *ACS Nano*. **2014**, *8*, 3904–12.

[84] Stoll, S.; Schweiger, A. EasySpin, a comprehensive software package for spectral simulation and analysis in EPR. *J. Magn. Reson.* **2006**, *178*, 42–55.

[85] Neese, F. Metal and ligand hyperfine couplings in transition metal complexes: The effect of spin–orbit coupling as studied by coupled perturbed Kohn–Sham theory. *J. Chem. Phys.* **2003**, *118*, 3939.

[86] Knight, W. D.; Clemenger, K.; Heer, W. A. de; Saunders, W. A.; Chou, M. Y.; Cohen, M. L. Electronic Shell Structure and Abundances of Sodium Clusters. *Phys. Rev. Lett.* **1984**, *52*, 2141–2143.

[87] Khanna, S. N.; Jena, P. Assembling crystals from clusters. *Phys. Rev. Lett.* **1992**, *69*, 1664–1667.

[88] Hartig, J.; Stößer, A.; Hauser, P.; Schnöckel, H. A Metalloid [Ga23{N(SiMe3)2}11] Cluster: The Jellium Model Put to Test. *Angew. Chemie Int. Ed.* **2007**, *46*, 1658–1662.

[89] Lange, T.; Gohlich, H.; Bergmann, T.; Martin, T. P. Calculated electronic properties of medium sized sodium clusters: the inhomogeneous jellium model. *Zeitschrift Phys. D Atoms, Mol. Clust.* **1991**, *19*, 113–115.

[90] Murray, R. W. Nanoelectrochemistry: Metal Nanoparticles, Nanoelectrodes, and Nanopores. *Chem. Rev.* **2008**, *108*, 2688–2720.

[91] Aikens, C. M. Electronic Structure of Ligand-Passivated Gold and Silver Nanoclusters. *J. Phys. Chem. Lett.* **2011**, *2*, 99–104.

[92] Devadas, M. S.; Bairu, S.; Qian, H.; Sinn, E.; Jin, R.; Ramakrishna, G. Temperature-Dependent Optical Absorption Properties of Monolayer-Protected Au25 and Au38 Clusters. *J. Phys. Chem. Lett.* **2011**, *2*, 2752–2758.

[93] Chen; Ingram; Hostetler; Pietron; Murray; Schaaff; Khoury; Alvarez; Whetten Gold nanoelectrodes of varied size: transition to molecule-like charging. *Science*. **1998**, *280*, 2098–101.

[94] Aikens, C. M. Origin of Discrete Optical Absorption Spectra of M25 (SH) 18- Nanoparticles (M= Au, Ag). *J. Phys. Chem. C.* **2008**, *112*, 19797–19800.

[95] Aikens, C. M. Geometric and Electronic Structure of Au 25 (SPhX) 18 − (X = H, F, Cl, Br, CH 3 , and OCH 3). *J. Phys. Chem. Lett.* **2010**, *1*, 2594–2599.

[96] Bauernschmitt, R.; Häser, M.; Treutler, O.; Ahlrichs, R. Calculation of excitation energies within time-dependent density functional theory using auxiliary basis set expansions. *Chem. Phys. Lett.* **1997**, *264*, 573–578.

[97] Lee, D.; Donkers, R. L.; Wang, G.; Harper, A. S.; Murray, R. W. Electrochemistry and optical absorbance and luminescence of molecule-like Au38 nanoparticles. *J. Am. Chem. Soc.* **2004**, *126*, 6193–9.

[98] Antonello, S.; Perera, N. V; Ruzzi, M.; Gascón, J. a; Maran, F. Interplay of charge state, lability, and magnetism in the molecule-like Au25(SR)18 cluster. *J. Am. Chem. Soc.* **2013**, *135*, 15585–94.

[99] Aikens, C. M. Effects of core distances, solvent, ligand, and level of theory on the TDDFT optical absorption spectrum of the thiolate-protected Au(25) nanoparticle. *J. Phys. Chem. A.* **2009**, *113*, 10811–7.

[100] Antonello, S.; Hesari, M.; Polo, F.; Maran, F. Electron transfer catalysis with monolayer protected Au25 clusters. *Nanoscale*. **2012**, *4*, 5333.

[101] Liu, Z.; Zhu, M.; Meng, X.; Xu, G.; Jin, R. Electron Transfer between [Au 25 (SC 2 H 4 Ph) 18] − TOA + and Oxoammonium Cations. *J. Phys. Chem. Lett.* **2011**, *2*, 2104–2109.

[102] Akbari-Sharbaf, A.; Hesari, M.; Workentin, M. S.; Fanchini, G. Electron paramagnetic resonance in positively charged Au25 molecular nanoclusters. *J. Chem. Phys.* **2013**, *138*, 024305.